QUANTITATIVE THEORIES OF NANOCRYSTAL GROWTH PROCESSES

Michael D. Clark

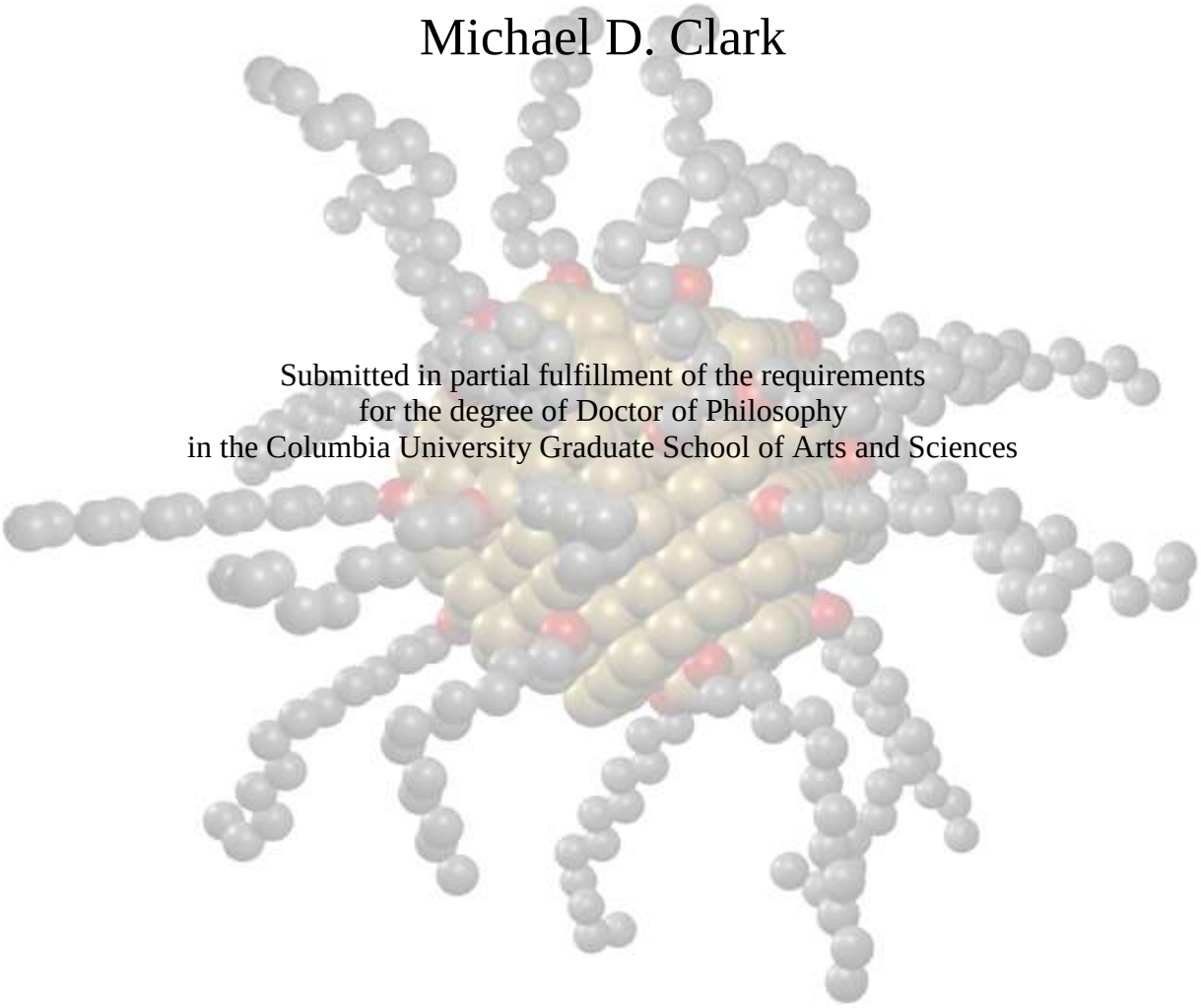

Submitted in partial fulfillment of the requirements
for the degree of Doctor of Philosophy
in the Columbia University Graduate School of Arts and Sciences

COLUMBIA UNIVERSITY
2013

ABSTRACT
Quantitative Theories of Nanocrystal Growth Processes
Michael D. Clark

Nanocrystals are an important field of study in the 21st century. Crystallites that are nanometers in size have very different properties from their bulk analogs because quantum mechanical effects become dominant at such small length scales. When a crystallite becomes small enough, the quantum confinement of electrons in the material manifests as a size-dependence of the nanocrystal's properties. Electrical and optical properties such as absorbance, surface plasmon resonance, and photoluminescence are sensitive to the size of the nanocrystal and proffer an array of technological applications for nanocrystals in such fields as biological imaging, laser technology, solar power enhancement, LED modification, chemical sensors, and quantum computation.

The synthesis of size-controlled nanocrystals is critical to using nanocrystal in applications for their size-dependent properties. The development of nanocrystal synthesis techniques has been its own entire field of study for two decades or more, and several successes have established novel, utilitarian protocols for the mass-production of nanocrystals with controlled size and very low polydispersity. However, the experimental successes are generally poorly understood and no theoretical framework exists to explain the dynamics of these processes and how to better control or optimize them. It is the goal of this thesis to develop novel theories of nanocrystal synthesis processes to describe these phenomena in theoretical detail and extract meaningful correlations and driving forces that provide the necessary insight to improve the technology and enhance our understanding of nanocrystal growth.

Chapter 4, 5 and 6 comprise all the novel research conducted for this thesis, with Chapters 1, 2 and 3 serving as necessary background to understanding the current state of the art. In Chapter 4, we develop a quantitative describe of the process of size focusing, in which a population of polydisperse nanocrystals, which are useless for applications, can be made more monodisperse by the injection of new crystallizable material. We derive mass balance equations that relate the rate of new-material generation to changes in the growth patterns of the nanocrystals. Specifically, we determine that only when the rate of crystal-material production is sustained at a high level can size focusing occur and a monodisperse sample of nanocrystals be produced. Quantitative criteria are provided for how high the rate of production must be, and the quantitative effects on the nanocrystal size distribution function for various magnitudes of the production rate. The effect of the production rate on every facet of the size distribution function is evaluated analytically and confirmed numerically. Furthermore, through comparison of the theory to experimental data, it is determined that a typical nanocrystal synthesis accidentally correlates two variables that are critical to the phenomenon of size focusing. The unknowingly correlated variables have frustrated experimental investigations of the same insights we provided with theory. We recommend a new synthesis protocol that decouples the critical variables, and thus permit the quantitative control of nanocrystal size and polydispersity through theoretical relations, which can also be generalized for the *a priori* design and optimization of nanocrystal synthesis techniques.

In Chapter 5, a theoretical investigation of the growth of surfactant-coated nanocrystals is undertaken. The surfactants create a layer around the nanocrystal that has different transport properties than the bulk solution, and therefore has a strong effect on diffusion-limited growth of

nanocrystals. This effect of a surfactant layer is investigated through the lens of the LSW theory of Ostwald ripening as well as through the lens of our own theory of size focusing from Chapter 4. The quantitative effect of a surfactant layer on the various growth processes of spherical nanocrystals is determined, with the result that size focusing can potentially be enhanced by the choice of an appropriate surfactant for a particular nanocrystal material.

In addition to the kinetic studies of Chapter 4 and 5, a thermodynamic investigation of surfactant-coated nanocrystals is conducted in Chapter 6, with the goal of understanding the process known as "digestive ripening". In digestive ripening, a population of polydisperse gold nanocrystals is exposed to a strongly binding surfactant, at which point the nanocrystals spontaneously shrink and become highly monodisperse. Different surfactants and different crystal materials can exhibit digestive ripening. Those same materials also have the capacity to be digested further from nanocrystals into molecular clusters that eliminate all crystalline material in favor of surfactant-crystal coordination. The outstanding question is, why does the spontaneous digestive ripening process appear to make large nanocrystals shrink to small nanocrystals, but it does not force small nanocrystals to shrink further to molecular clusters? We construct a full Gibbs free energy model, which we minimize under multiple constraints to obtain quantitative relations for what thermodynamic properties (such as the surfactant binding energy and the crystal-solvent surface energy) govern the existence and size-dependence of a thermodynamically stable nanocrystal. Through our model, we determine that a finite-size nanocrystal is only stable under two possible conditions: either the surfactant-crystal binding is stronger than the crystal-crystal binding and the system contains too few surfactants to form molecular clusters and thus "surfactant-lean" nanocrystals are created, or the surfactant-

surfactant intermolecular interactions are sufficiently strong that the nanocrystal core is treated as a swollen micelle in a microemulsion and is stabilized by the surfactant tails' interactions. Quantitative equations are provided that establish what trends and values are expected for experimental results. The results are inconclusive: there is no evidence supporting either conclusion because the available experimental data is insufficient. More accurately, many thermodynamically critical parameters (like the crystal surface energy) are unknown and are practically immeasurable in experimental systems. Speaking generally, the evidence for the surfactant-lean condition is moderately better than the evidence for the microemulsion condition, but in both cases the evidence is insufficient to make a solid conclusion. We therefore use our quantitative results of the thermodynamic investigation to make recommendations to experimentalists as to what trends and what nanocrystal growth processes we expect to observe in either thermodynamic case. While our results are inconclusive in and of themselves, they will be used to highlight the exact thermodynamic driving forces of the experimental systems.

We conclude by giving an overview of two new fields of study for theoretical descriptions of nanocrystal growth, specifically the growth of anisotropic nanocrystals and a practical theory for nanocrystal nucleation. Preliminary relations are constructed, with comments on what directions we expect the research to take and how the results would be useful in enhancing our understanding of nanocrystal growth behavior.

TABLE OF CONTENTS:

LIST OF FIGURES

ACKNOWLEDGMENTS

"All models are wrong. Some models are useful."
Attributed to George E. Box from "Science and Statistics." 1976

"The essence of research is solving for the question."
Attributed to Allen Boozer, by Dr. David Keyes of Columbia APAM

There is no description for the experience of obtaining a doctoral degree from an Ivy League university like Columbia while raising two children at home. Needless to say, it would not have been possible without the continuous support of friends, family, and collaborators who perpetually steered me right when I was wrong and who supported me when I fell.

I first wish to thank my adviser, Dr. Sanat Kumar, for his unending patience with the fact that I frequently insist on doing things a different way. "Doing things my own way" perhaps is more appropriate, and it led to more than one strained discussion over how to view a particular problem. At all points, though, Sanat was insightful and instructive, wishing only for me to succeed and giving me all the support he was able to. He also informed me of several opportunities that I would have otherwise missed, like applying for an award through the American Chemical Society for which I won 2nd place, or applying to teach a course at Columbia and boosting my teaching credentials with an Ivy League course even before I graduated. I look forward to collaborating with Sanat in the future and I wish him well in future years.

Special thanks go to our collaborators. For the size focusing study, the input of Dr. Jonathan Owen, Dr. Emory Chan, and the entire Owen research group was indispensable in learning how to approach the problem of nanocrystal growth from an experimental perspective. Dr. Emory Chan also provided copious amounts of data to which we were able to compare our conclusion.

Certain members of the Owen research group, particularly Zak Norman and Alex Beecher, have been wonderfully entertaining of my ideas and even conducted one or two experiments for my benefit, though the results were not publishable. The use of Single Chain Mean Field theory in the thermodynamic analysis of digestive ripening, which was a potentially traumatizing experience, was made tolerable and even enjoyable by Dr. Igal Szleifer and Dr. Rikkert Nap of Northwestern University. I was invited to their lab and given more attention and advice than I expected, and the results were critical to the formulation of our results. Also, Dr. Saroj Nayak and his student Albert Deardon were helpful in providing DFT results to inspire which directions our digestive ripening analysis should take. The results of Albert's studies did not make it into this thesis, but when they are more fully fleshed out, I intend to include them in final publication.

To my fellow graduate students of Columbia Chemical Engineering, your patience, support, discussions, and occasional parties helped me get through the most difficult problem-solving days of my stay. Most special thanks go to Allison Schwier, Neha Sareen, and Joe Woo for all those days that they watched my daughters Julia and Emma while I went to a meeting or watched a presentation. I know they loved watching my girls, but it was still a favor that I feel I will be perpetually trying to repay.

Thank you to my family, my parents, my mother-in-law, my aunt-in-law, my sisters, my sister-in-law, and my brothers-in-law for your emotional and occasionally fiscal support through the last five years, and thank you also for all the last-minute babysitting favors, the free dinners and lunches, and the continual rearranging of schedules to work around the fact that we live in NYC where traffic disasters and weather disasters are equally frequent and equally ferocious. I was

pleased to have you visit our NYC apartment as often as you did, as inconvenient as it was, and I will never forget how much help I got from all of you in whatever form it came.

Finally, and most importantly, thank you to my wife, Laura Clark. Without your inspiration, I never would have applied to Columbia for graduate school. Without your courage, I never would have accepted the admission while you were pregnant with Julia. And without your sacrifice, I never could have finished this degree. I know only my name gets the "Dr." in front of it, but this achievement belongs to us both.

CHAPTER 1

WHY NANOCRYSTALS MUST BE MONODISPERSE

1.1 INTRODUCTION

In 1984 Dr. Luis Brus published a theoretical description of "semiconductor crystallites" with the remarkable conclusion that the electronic properties of nano-scale crystallites differ from those of bulk crystal; moreover, and most importantly, the theory established that crystallites' electronic properties depend on their size.[3] Brus' results that size and properties are correlated at the nanoscale were so powerful as to spawn a whole new field of study: nanocrystals.

Since their discovery, nanocrystals of myriad types and materials have been synthesized, all with unique and useful properties. Making crystallites on the nanoscale instead of the micron scale enhances the surface plasmon resonance of gold and silver[4], vastly increases the material strength of copper and palladium[5], adjust the magnetic relaxation time in iron oxide and cobalt[6], and gives rise to size-dependent photophysical properties in direct band-gap

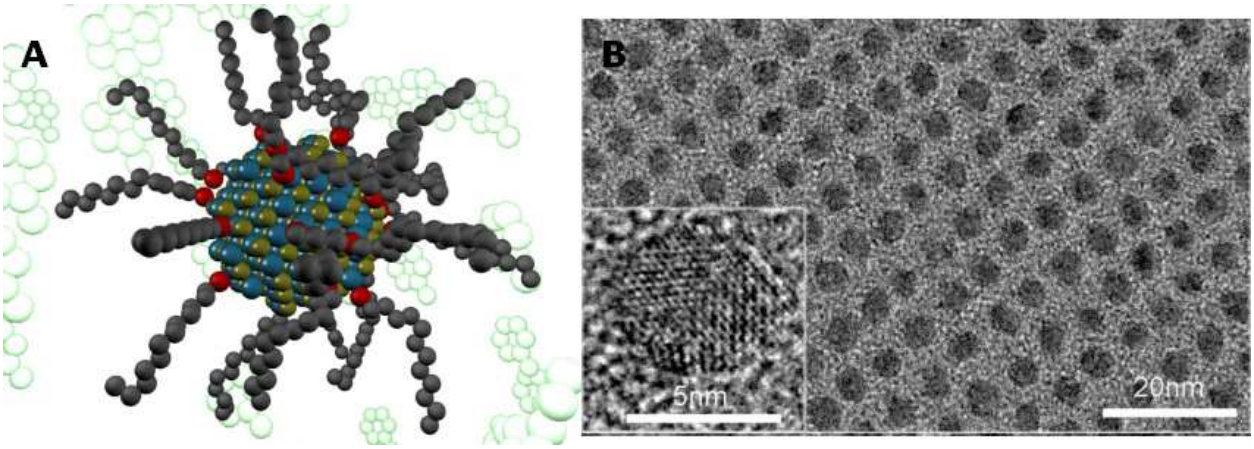

Figure 1.1: (a) Artistic representation of a nanocrystal coated with surfactant molecules. (b) TEM micrograph of CdSe nanocrystals. Inset represents HRTEM of a single CdSe nanocrystal, illustrating the crystal interior.[2]

semiconductors[2, 3, 7]. Semiconductor nanocrystals, also called "quantum dots"[8], have been the most often studied class of nanocrystals since their discovery 30 years ago. In fact, a digital search of the literature reveals that some 125,000 published works relate to nanocrystals, with approximately 60,000 that involve semiconductors and quantum dots.[9]

1.2 THE QUANTUM DOT

The reason that semiconductor nanomaterials are so interesting is the behavior of the electrons in their conduction band. The conduction band of a semiconductor has a small but appreciable population of electrons because the energy gap between the valance band and the conduction band is present but reasonably small (~1-2 eV). In metals, there is no energy gap between the bands and valance electrons perpetually occupy the conduction band (thus the "sea of electrons" model). The band gap energy in insulators, on the other hand, is so large that the number of electrons in the conduction band is nearly zero. Semiconductors are in between and there is a small but perpetual population of electrons in the conduction band which are freely mobile within the material.

In a bulk-sized material, where the semiconducting object is much larger than a conduction electron's de Broglie wavelength, the probability distribution of electrons in the material is practically uniform. Consider, however, a very thin semiconductor plate: the probability of finding a conduction electron outside the plate is zero. If the width of the plate is smaller than the electrons' de Broglie wavelength, then the electrons in the conduction band of the plate behave like particles in an infinite square well. Thus the wavelength λ and its multiples $n\lambda$ are determined explicitly by the width of the plate, as are the energy levels the conduction-band

electron can occupy. This inspired the named "quantum well" for a semiconductor plate that is nanometers wide, because it constrains excited electrons in one dimension while leaving them freely mobile in the other two dimensions. A semiconductor wire that is nanometers in diameter, also called a "quantum wire", will constrain the conduction electrons in two dimensions, allowing only one dimension of mobility. Finally, electrons can be constrained in all three dimensions in a spherical semiconductor nanocrystal, restricting the electrons to be distributed within the conduction band about a point, hence the name "quantum dot".[10]

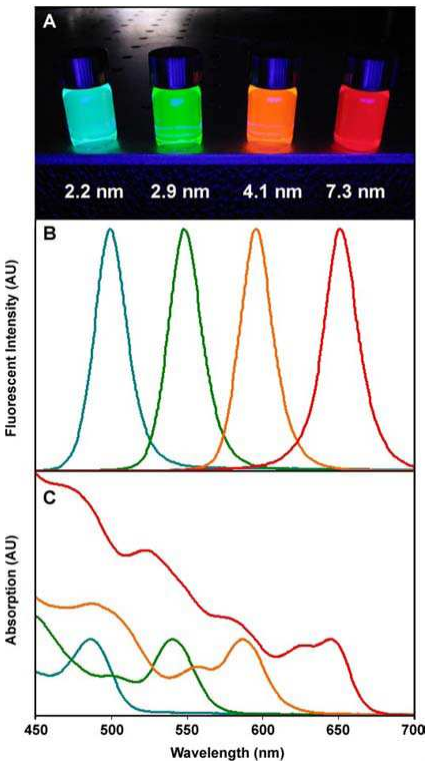

Figure 1.2: Optical properties of CdSe nanocrystals in CH_2Cl_2. (a) Fluorescence image of four vials of monodisperse nanocrystals with several diameters under UV-lamp illumination at 365 nm. (B) Fluorescence spectra of the same four samples, excited at 400 nm. (C) Absorption spectra of the same four samples.[1]

The correlation between nanocrystal size and the electron energy levels in the conduction band has many effects that are useful for technological applications. The first and most obvious is a quantum dot's emission spectrum. Because electrons can only exist at wavelengths $n\lambda$ and all its transitions have energy hc/λ, relaxing electrons will always emit photons of the same particular energy from a nanocrystal of a particular size. Therefore, a semiconductor nanocrystal may absorb a wide frequency range of incident light, but it will only emit a *particular color of light*.[1] Figure 1.2 displays this phenomenon the most readily: an ultraviolet light is shining in the background, and in the foreground are vials of CdSe nanocrystals of different sizes in solution. The 2-nm nanocrystals absorb the UV rays and emit only cyan photons, while the 7-nm nanocrystals absorb the same UV rays but emit red photons. As the

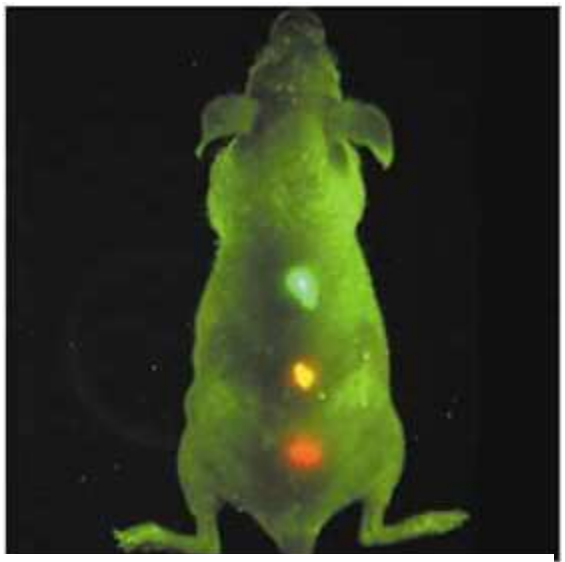

Figure 1.3: A mouse has been given three types of cancer. Three solutions of differently-sized, monodisperse quantum dots have been functionalized to bind to the different cancerous cells, were injected simultaneously into the mouse, and were exposed to UV light. The fluorescence represents quantum dot conjugation to cancer cells. [16]

figure indicates, the wavelength of emitted light is continuously tunable by changing the size of the nanocrystals. By changing the semiconductor material, the exact relationship between size and emission spectra will change, but all semiconductor materials have the property that size and photophysical behavior are strongly correlated at the nanoscale.

The ability to control electronic and optical properties of a species merely by altering the number of atoms it contains became an immensely powerful tool in the search for new, technologically viable nanomaterials. The applications of these optical behaviors are ideal for LEDs[10, 11] and solar power enhancement[12, 13]. By functionalizing a quantum dot surface, nanocrystals can become non-photobleaching biological imaging agents[1, 14-16] or chemical sensors that emit particular frequencies of light upon chemical reaction[17, 18]. Figure 1.3 shows how different quantom dots can be functionalized and used to detect different types of cancer in a rat. Their more exotic properties include specific interactions between quantum dots, called quantum dot coupling, which make nanocrystals suitable for information storage and/or quantum computing.[19] Current work in that field focuses on building such "qubits" with much success, and the eventual goal is a quantum dot processor with a vastly superior computing speed and capacity than current transistor based processors.[20-23]

A host of new studies began exploring semiconductor nanocrystals, fueled by the discovery that it is possible by controlling a nanocrystal's size to control its properties. Those same studies were limited, however, by the fact that *it is necessary* to control a nanocrystal's size in order to control its properties. With this statement, the magnitude of the problem becomes clear. Trillions of nanocrystals, dispersed in solution and made of a few hundred to a few thousand atoms each, must all be roughly the same size to be useful. Synthesizing a solution of nanocrystals was relatively easy, but producing aliquots of nanocrystals that were all nearly the same size was immensely difficult. The biggest barrier to synthesizing uniformly-sized nanocrystals is Ostwald ripening. The process of Ostwald ripening, named after Wilhelm Ostwald who discovered the phenomenon in the late 19th century, makes any system of precipitating clusters (like nanocrystals) more polydisperse with time because small particles shrink while large particles grow.[24, 25] Figure 1.4(a) provides a representative picture of Ostwald-ripened nanocrystals under TEM.[26] Ostwald ripening is a natural kinetic process that allows immiscible materials to completely phase separate, even if it begins with the nucleation of many small zones. It occurs in nanocrystals, in oil-water mixtures, in metallic alloys, and the quantitative results even successfully describe spinodal decomposition.[27-30] Almost universally, producing nanocrystals that are monodisperse enough for applications requires a procedure that defeats Ostwald ripening.

Scalable synthesis of monodisperse nanocrystals has received substantial attention in the last three decades, but it has yielded few new options. Techniques like building microfluidic reactors and using metal vaporization have provided new routes to controlling the size of nanocrystals, but these techniques do not in general benefit from economies of scale in the way a truly

homogeneous-solution based protocol would.[31, 32] To that end, an economically appealing procedure would be most similar to classical chemical reactions whose kinetics and behaviors can be captured and optimized using standard chemical engineering. In the last 20 years only two techniques have been developed that meet these criteria: "size focusing" and "digestive ripening".

1.3 SIZE FOCUSING:

The name "size focusing" was coined by Xiaogang Peng et al. in 1998 in a publication that was in essence a proof-of-concept. After a solution of CdSe nanocrystals was observed the Ostwald ripening for some time, a second injection of reactants was added to the solution, delivering more crystallizable material to the solution. The growth of nanocrystals accelerated and, more importantly, the width of the size distribution saw a significant decrease. The injection of new material led explicitly to a narrower nanocrystal size distribution.[28]

This process of narrowing was termed "size focusing," while Ostwald ripening was called "defocusing". Differently sized injections each caused size focusing at different extents, suggesting a rough correlation therein. However, though multiple injections were studied in other publications, a comprehensive study was never truly made.

With the improvement of size-measurement techniques, nanocrystal studies began to include time-wise size measurements as a matter of course. It was quickly observed that nanocrystals grew most often in a particular pattern: nucleation occurs and the number of nanocrystals increases with time; a brief but measurable period of size focusing follows; and size focusing

gradually transitions to Ostwald ripening. The size focusing-to-Ostwald ripening motif was witnessed in many different systems with different materials, conditions, and protocols.[33-38] While it was surmised that the initial size focusing was likely related to the study by Peng et al. regarding a second injection, and although several research groups explored the phenomenon theoretically and numerically[38-41], the ultimate mechanism of the transition was never established.

A further trend was noticed among some nanocrystal experimenters, one that did not improve the outlook on nanocrystal manufacturability. For certain solution-based syntheses, across multiple materials, the final size of the nanocrystals did not change when the initial amounts of the precursors were adjusted.[42, 43][44] In some cases orders-of-magnitude increases in the initial precursor concentrations did not yield a significant difference in the measured size and polydispersity of the product nanocrystals. This pattern explicitly contradicted the results of Peng et al. which demonstrated a correlation between the degree of focusing and the size of the second injection. These mysteries of size focusing have persisted for over a decade.

1.4 DIGESTIVE RIPENING:

A second synthesis protocol which yields highly monodisperse nanocrystals is the process of digestive ripening. Digestive ripening is kinetically the exact opposite of Ostwald ripening: a solution of large, polydisperse nanocrystals is "digested" down to small, highly monodisperse nanocrystals upon addition of surfactant.[26, 45, 46] Smaller particles are witnessed to grown even as large nanocrystals shrink, again representing the antithesis of Ostwald ripening, with all nanocrystals in the solution eventually arriving at the same monodisperse size. The product

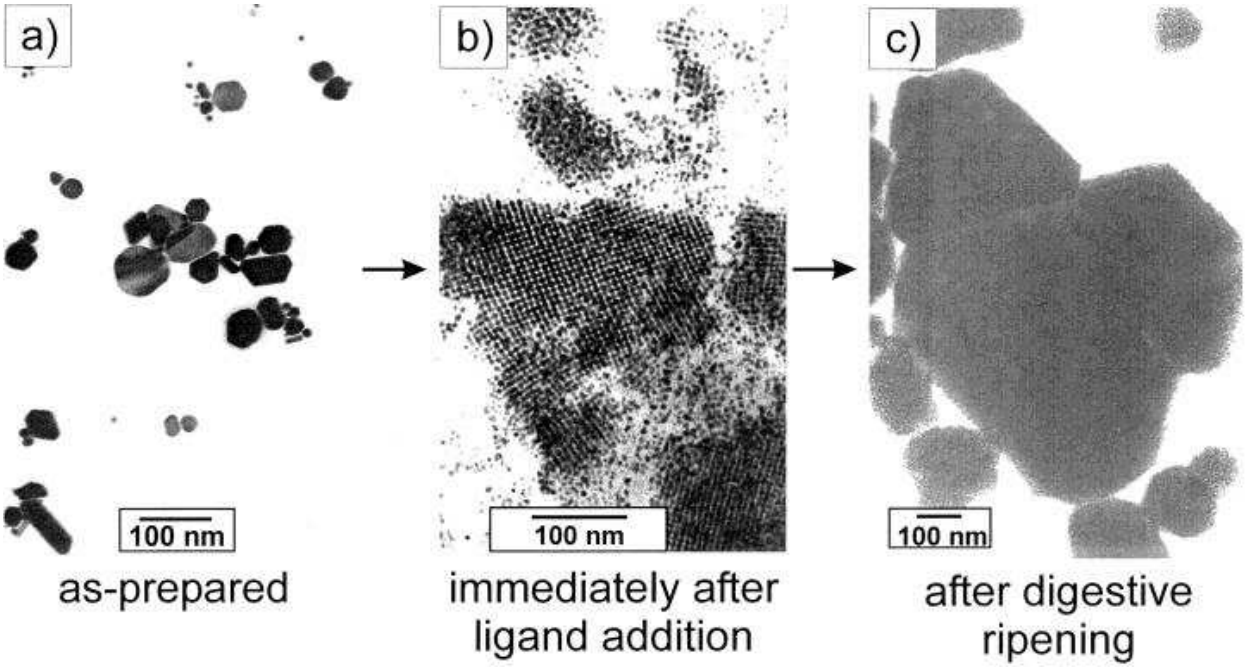

Figure 1.4: (a) Pictorial demonstration of digestive ripening, where polydisperse gold nanocrystals (a) are digested by a strongly binding ligand (b) and then refluxed, which causes digestive ripening and yields monodisperse nanocrystals. [46]

nanocrystals are highly stable, preserving their size for months at room temperature. Most importantly, the change from Ostwald ripening to digestive ripening can be effected merely by adding a strongly-binding surfactant.[46] The utility of this method for synthesizing mass-produced nanocrystals on an industrial scale is obvious: simply mixing a nanocrystal solution with a surfactant will produce high-quality nanocrystals that are immediately ready to use in applications or even to store for sale to other manufacturers.

Digestive ripening has been exhibited for nanocrystals of gold, silver, palladium, cobalt, iron oxide, certain transition metal alloy nanocrystals, and even recently of indium sulfide nanocrystals.[47-52] Several surfactants can effect digestive ripening: alkyl thiols and alkyl amines are common digestive ripening agents, especially for noble metal syntheses. The real mystery of digestive ripening is that often, surfactant is added in far excess quantities. Gold nanocrystals undergo digestive ripening and form finite-size nanocrystals (4 nm or greater) even

when the surfactant-to-gold ratio is 30:1.[26, 45, 46] There is more than enough surfactant to coordinate to every individual gold atom in solution, but for some reason the small nanocrystals are not further digested. The driving force for digestive ripening is not well understood. It is so powerful that gold nanocrystals are reduced from 80 nm to 4 nm within a minute, and it is so universal that multiple different surfactants will induce it. However, the digestion completely ceases when the nanocrystals reach the 1-10 nm scale. The reasons for this behavior remain an open question with many variables and few answers.

1.5 THE NEED FOR THEORY:

Size focusing and digestive ripening have shown immense promise for scalable synthesis of monodisperse nanocrystals, but neither process is well understood. Experimental studies can interrogate these systems only in a limited fashion for several reasons: measurement error is significant, the syntheses can expensive and dangerous, and there is no limit to the number of viable reagents and materials. Some numerical studies and simulations have been undertaken as well, but in general these have offered little insight into the experimental systems.

The most important barrier to exploring size focusing and digestive ripening using experiments is the vast parameter space. Every nanocrystal experiment involves two reagents, often a surfactant, a solvent, a temperature, a reaction time, and a host of procedural choices. Even a comprehensive analysis of all the current nanocrystal studies is difficult because of all the variations between studies. If one were to interrogate a particular synthesis, a good starting place is varying concentrations. Even exploring four values for each precursor and the surfactant, however, becomes cumbersome and difficult to do inexpensively and reliably. Recent

developments in automated technologies have now enabled such parametric studies of single-injection syntheses in a plausible timeframe if they only depend on a few variables. However, size focusing and digestive ripening each involve a *second injection* of new material into an existing nanocrystal solution, instantly doubling the number of parameters (which squares the number of experiments) and introducing new procedural variables that could be critical (induction time, injection rate, mixing rate, etc.). Even if all the experiments were limited to two choices of each parameter, even this poor exploration would cause the number of analyses to explode. Hundreds or even thousands of experiments would be required and the relevant physics may still be overlooked.

The final blow to the utility of such an unwieldy parametric study is the limitations in measuring the system. There are few ways to measure nanocrystal sizes and size distributions, almost all of which are either indirect (UV-Vis spectroscopy, SAXS) or *ex-situ* (TEM, mass spectrometry), all with a measurement error on the order of 5-10%.[53] Simply determining the number of nanoparticles in a container has a measurement error of up to 30%[53], and some physical properties like solubility or surface tension are almost impossible to measure. In short, all the limitations in time, funding, and accuracy make it intractable to understand thoroughly how user-controlled variables affect the outcome of experiments.

It is for this reason that we undertook this thesis, to study the synthesis of monodisperse nanocrystals from a theoretical perspective and to gain insight into the critical variables that control size focusing and digestive ripening. The question remained, however, what techniques to use.

In general, full simulations are inadequate to assessing nanocrystal growth. One nanocrystal, made of thousands atoms growing over a period of minutes, cannot be analyzed by molecular dynamics or Monte Carlo simulations, which are best suited to the sub-nanosecond timescale. To represent a milliseconds-long process in MD or MC would require such drastic coarse-graining that the critical physics of the process could too easily be lost. Phase-field simulations were briefly entertained, where a stochastic differential equation that models the evolution of a phase-separating system described by a density field $\rho(\mathbf{r})$. However, the problem of finite-size effects and the choice of the thermodynamic model only expanded the necessary parameter space, and individual simulations took dramatically longer than an experiment. The model was simply unable to provide enough insight in a timely fashion. Numerical investigations of any sort, stochastic or otherwise, all face the same barrier: the results depend on the initial inputs, and no computer-based simulation can effectively capture all the various dependencies on all the relevant variables. The resultant conclusion is this: exploring the parameter space must be avoided, by producing results that include the parameters themselves. Therefore, our investigation of nanocrystal synthesis techniques would be based in the formulation of new theories using analytical "pencil-and-paper" mathematics.

Analytical mathematics has been used before to investigate precipitation and nanocrystal growth, but it is mostly on a rudimentary level. The most prevalent use of analytical methods to produce a quantitative theory is actually the theory of Ostwald ripening, written in 1961 by both Lifshitz and Slyozov and separately by Wagner.[54-56] Application of LSW theory has revealed that certain nanocrystal systems do indeed undergoing Ostwald ripening exactly as the theory

predicts (i.e. CdS, CdSe).[28, 38, 57] This successful comparison serves as a proof-of-concept that LSW theory ascribes the correct mechanisms to how nanocrystals grow. However, the vast majority of nanocrystal syntheses violate the assumptions of LSW theory, most notably the size focusing and digestive ripening processes which we are investigating. The proof that LSW theory is occasionally successful for nanocrystals implies that its assumptions are a good starting point, and perturbing their analysis has the potential to explain nanocrystal behaviors in other modes.

Deriving the theory of size focusing begins with the same initial governing equations as LSW theory, and extends the concepts to a system in which the volume of solute is not conserved. Since it is the injection of new crystallizable material that effects size focusing, the material balance is perturbed by including a homogeneous molar generation rate which provides new material even as the nanocrystal ensemble evolves. The derivation for the theory of digestive ripening, however, cannot begin with LSW theory because the first governing equation explicitly denies the existence of a stable size. The typical application of the Gibbs-Thomson effect (described in Chapter 3) does not permit any finite-size nanocrystal to be stable in solution. Digestive ripening must therefore be analyzed by a new thermodynamic treatment first, which must include the quantitative reason that Gibbs-Thomson does not apply, to determine how it is primarily different from Ostwald ripening. Then a kinetic analysis may be applied, akin to LSW theory, to determine if and how the evolution of the final digestive ripening size can be tuned using adjustable experimental conditions.

CHAPTER 2

TWENTY YEARS OF NANOCRYSTAL STUDIES

2.1 SEMICONDUCTORS

Modern synthesis of quantum dots began, in its essence, with the publication by Murray et al. in 1993.[7] Murray and coworkers described the first successful scheme for producing gram-scale quantities of monodisperse CdE quantum dots (where E represents the chalcogens, S, Se, and Te). Before this publication the production of nanocrystals had only produced solutions of polydisperse nanocrystals, which were impossible to characterize because their optical properties were not sufficiently uniform. Murray's synthesis of monodisperse nanocrystals permitted the accurate correlation between a nanocrystal's size and composition and its optical properties.

Briefly, the Murray synthesis is described as follows. The synthesis is solution-based, the general idea being that a cadmium precursor and a selenium precursor would undergo a chemical reaction in solution to general single units of CdSe, called "crystal monomers", which are dissolved but supersaturated in solution. When the monomer concentration became high enough, the monomers nucleate homogeneously to form tiny clusters, which then proceed to grow by adsorbing the other dissolved monomers. This general synthesis route had been established a decade previously. Murray et al.'s materials included trioctylphosphine oxide (TOPO) as the solvent, a precursor of dimethyl cadmium (Me_2Cd) dissolved in trioctylphosphine (TOP), and the chalcogen precursor E (where E = S, Se, Te) which is either phosphine chalconide (TOP-E) or bis-trimethylsilyl chalconide ($(TMS)_2E$). Both Cd and E precursors are injected into the TOPO at about 300oC which instantaneously nucleates the nanocrystals in a dangerously explosive

reaction. The reaction produced nanocrystals that were polydisperse but of high-quality crystallinity.

The key step to obtaining monodisperse nanocrystals was size-selective precipitation. The nanocrystals were cleaned with various alcohols to remove byproducts and transferred to a flask of anhydrous butanol. The nanocrystals were soluble in butanol and insoluble in methanol, thus the nanocrystals precipitate upon methanol addition. However, a nanocrystal's solubility in a butanol-methanol mixture is size-dependent: larger nanocrystals precipitate at lower concentrations of methanol. Thus, methanol is added in small aliquots to encourage precipitation of only the largest nanocrystals in solution. The precipitated nanocrystals were removed and methanol was added again, with sequence continuing until the optical absorption no longer changed with methanol addition. With the protocol, the polydisperse nanocrystals from the reaction were filtered into separate solutions of monodisperse nanocrystals at various sizes. Figure 1.2 shows four vials of size-selected CdSe nanocrystals, displaying their size-dependent optical properties and exhibiting their monodisperse nature.[1] Each solution of monodisperse nanocrystal was then characterized by several measurement techniques, representing the first accurate size-dependent characterizations of semiconductor nanocrystals in literature.

After Murray et al. synthesized and characterized the semiconductor nanocrystals, their results gained traction in the scientific community and many other breakthroughs followed. The use of quantum dots in specific applications grew, for example with CdSe nanocrystals employed in light emitting diodes, in biological labels, and in photovoltaic cells.[1, 11-14, 58] An interest grew in the formation of 3D superlattices of quantum dots, where monodisperse nanocrystals

spontaneously arrange into regular and adsorption-friendly structures in solution.[59-61] Studies of high quality core-shell quantum dots surfaced within months the Murray synthesis, in which a core nanocrystal of one material (e.g. CdSe) is coated with a few monolayers of a different crystalline material (e.g. ZnS) to enhance and modify its photophysical properties.[62, 63] Various surfactants were chosen for each nanocrystal material to adjust its nucleation, growth, solubility in solution, shape, and optical properties.[64-68] Most important, the Murray publication enabled the entire scientific community to characterize the product and to perturb the method for characterizing novel nanocrystals, which led to an explosion of nanocrystal examinations and novel nanocrystal applications.

However, size-selective precipitation of the nanocrystals posed a significant barrier to the growth of the technology. The protocol described above required many expensive and time-consuming steps that are each difficult to scale up due to both engineering and economical inefficiencies. All the new applications for quantum dots were being created without a viable route for their mass production.

2.2 SIZE FOCUSING AND THE FOCUSING-DEFOCUSING TREND

In 1998 Peng et al. tested a hypothesis inspired by a previous analysis from Tadao Sugimoto. Sugimoto had analyzed the equation dR/dt, the rate of growth of a given spherical particle in a given solution, which was given by the LSW theory of Ostwald ripening particles (see Figure 4.1 and Chapter 4 for more information). Briefly, the conclusion was that suddenly increasing the concentration of dissolved crystal monomers in a system of growing particles would cause the particles to grow faster, but more monodisperse with time.[69] Sugimoto's analysis amounted

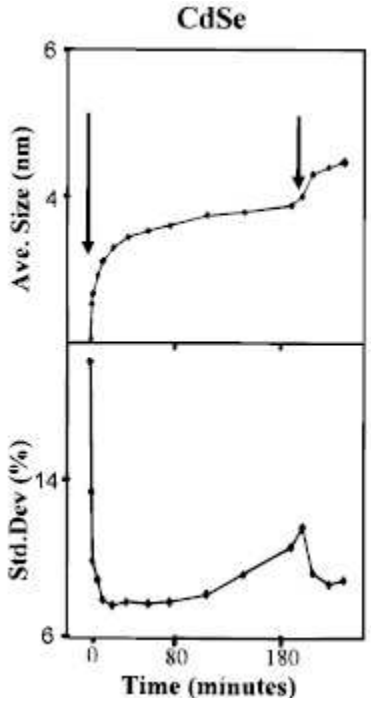

Figure 2.1: Size focusing of nano-crystals by injecting new precursors. Arrows indicated injection times. [50]

only to a scaling law and was proved by the synthesis of highly monodisperse micron-size crystals of silver halides, making the analysis a qualitative success.[70, 71]

Peng et al. applied that conclusion to their nanocrystal system. First, a solution of CdSe nanocrystals was synthesized as per the Murray synthesis, and the mixture was allowed to Ostwald ripen. Then, a fresh supply of crystal precursor was injected to raise the dissolved monomer concentration suddenly. The growth after the second injection followed Sugimoto's conclusions, with a jump in the average diameter and a drop in the polydispersity as recorded by UV-Vis spectroscopy and confirmed by TEM (see Figure 2.1). Peng et al. referred to the decreasing polydispersity as "size focusing". To explore the Sugimoto analysis, several syntheses employed different amounts of precursors for the second injection, which caused different degrees and durations of the size focusing event. Similar results were obtained for InAs nanocrystals. This study was critical to the development of nanocrystal technologies by transforming polydisperse nanocrystals into monodisperse ones merely by adding fresh reagents in a scalable protocol.

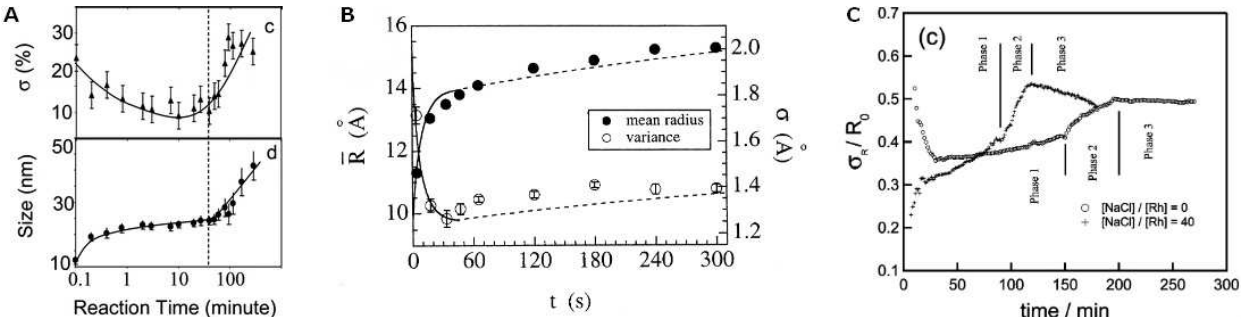

Figure 2.2: The focusing-defocusing trend observed in three systems: (a) MnO nanocrystals [37], (b) CdSe nanocrystals [38], and (c) rhodium nanocrystals [34]. The nanocrystals become first less polydisperse, then more polydisperse with time.

The Peng paper introduced the terms "focusing" and "defocusing" to the nanocrystal community. It is generally appreciated that defocusing represents Ostwald ripening, which is best described by LSW theory[54, 55], and that focusing is caused by the sudden introduction of new monomers, though the only theoretical description of it was Sugimoto's scaling argument. Since the coining of these terms, the transition from a "focusing" nanocrystal solution to a "defocusing" solution has been witnessed in many other nanocrystal systems, as shown in Figure 2.2. Immediately after nucleation, the nanocrystals first undergo size focusing which gradually transitions to Ostwald ripening. The pattern is visible across different synthesis techniques, different materials, and different groups, implying that the focusing-defocusing phenomenon is due to some fundamental physical behavior of a post-nucleation system.[33-38] The reasons for the focusing-defocusing transition remain an open question, but one that this thesis explicitly answers.

2.3 GOLD NANOCRYSTALS

Quickly following Murray's success in the synthesis of semiconductor nanocrystals, a revolution in nanocrystals of gold and other noble metals emerged. In 1994, Brust et al. achieved the successful synthesis of monodisperse, size-stable gold nanocrystals by coating them with alkanethiols.[72] The Brust synthesis started with inverse ionic micelles in toluene. Ionic gold ($HAuCl_4$) and alkanethiol were added: the gold precursor entered the hydrophilic micelle centers when shaken, and the alkanethiol presumably served as a co-surfactant. In the critical step, the gold was reduced with $NaBH_4$ inside the micelles, generating Au^0 monomers which nucleated

and crystallized while the alkanethiol grafted to the nanocrystal's surfaces. The resultant nanocrystals were monodisperse and mostly 2.0-2.5 nm in diameter. The nanocrystals could be precipitated and redispersed in fresh solvent and their sizes were indefinitely stable in solution. Within months, the same group published a follow-up study (commonly known as the Brust-Schiffrin synthesis) in which the same monodisperse gold-thiol nanocrystals were synthesized in a different solvent.[73] The Brust-Schiffrin synthesis also proved that if alkanethiol were entirely removed from the toluene-ionic surfactant solution, then stable gold nanocrystals could still be produced, though they were (a) larger, (b) more polydisperse, and (c) could not be precipitated and redispersed like their thiol-coated counterparts. Thus, Brust and coworkers discovered the stable gold-thiol nanocrystal.

In the last two decades, the Brust and Brust-Schiffrin syntheses inspired hundreds of perturbations and parametric studies on the formation of indefinitely stable gold nanocrystals. A parametric study by Leff et al. in 1995 varied the quantity of dodecanethiol used in the Brust synthesis.[74] (This study also developed the first theoretical treatment of gold-thiol nanocrystals, to be explored further in a later section.) The thiol-to-gold ratios employed by Leff et al. were 1:1, 1:2, 1:3, 1:3½, 1:4, and 1:6. The respective diameters of the product nanocrystals were 1.5 nm, 1.6 nm, 3.0 nm, 6.8 nm, 9.4 nm, and 20.2 nm, displaying a decrease in surface-to-volume ratio as the thiol-to-gold ratio decreased. However, the size does not increase linearly with the gold-to-thiol ratio, but increases less-than-linearly. The polydispersity also displays unexpected behavior. For the first four syntheses, the size dispersion was consistently about ±0.3 nm, which increased to ±0.7 nm for nanocrystals produced with a 1:4 thiol-to-gold ratio. However, in the final synthesis with a 1:6 thiol-to-gold ratio, the polydispersity was a very large

±3.8 nm. The authors describe these largest crystals as exhibiting "degradation of their solubility over time, especially when they are stored in air and under the influences of light." While it is unknown if the effect of storage was ever tested, Leff and coworkers do indicate that something was chemically different about the 1:6 thiol-to-gold synthesis. The work additionally proved that the thiol-to-gold ratio is important when thiol is the limiting reagent, but the results failed to elucidate why the 2-nm nanocrystals form for a 1:1 thiol-to-gold ratio, or why such nanocrystals are so stable.

From 1995 to 2000 a host of studies were published which analyzed the internal characteristics of gold-thiol nanocrystals. These included studies of the phase separation of the alkylthiol monolayer, myriad X-ray studies and mass spectrometry studies of an individual nanocrystal's structure, investigations of their spectroscopic properties, and variations of the surfactant.[4, 75-82] Stable gold nanocrystals were producing using alkyl amines as the surfactant, nanocrystal networks were created using bifunctional dithiol surfactants, and the procedure had even been generalized to other noble metals.[83] And a publication in Science in 1997 employed gold nanocrystals to produce a sensor solution, the spectroscopic and optical properties of which changed measurably, reliably, and selectively when a particular polynucleotide was introduced in the solution.[84]

2.4 DIGESTIVE RIPENING

In 2000 a particularly surprising study on gold nanocrystal synthesis was published by the Klabunde research group, which described the phenomenon of "digestive ripening".[26] The authors began with a slightly modified Brust synthesis. An ionic surfactant DDAB or

$(C_{12}H_{25})_2(CH_3)_2N^+Br^-$ was dissolved to 0.025M in toluene. $AuCl_3$ (0.112 mmol in 10 mL) was added to the solution, which was shaken. After all the gold salt lay inside the micelles, $NaBH_4$ was added (0.338 mmol) to reduce the gold ions. No thiol was present at this time. The product is shown in Figure 1.4(a), a solution of gold nanocrystals that were large and highly polydisperse, from 2 nm to about 80 nm in size. The nanocrystals were also distinctly non-uniform in shape, containing irregular spheres, prisms, and everything in between. The remarkable step was the addition of dodecanethiol *after* the initial nanocrystal formation in a thiol-to-gold ratio of approximately 30:1. Upon thiol addition, an immediate color change was noticed. The solution was mixed with ethanol, causing precipitation of the thiol-passivated nanocrystals. The precipitate was separated, dried, washed, and redispersed in toluene along with an additional dose of fresh dodecanethiol (again at 30:1 thiol-to-gold). The new solution was then refluxed (toluene's b.p. is 110ºC) for three hours, after which a TEM showed that the nanocrystals were much smaller and very monodisperse, at 6.2 ± 0.3 nm (Figure 1.4(b)) The process was named "digestive ripening" to reflect that this process (large, polydisperse crystals yielding small, monodisperse nanocrystals) is the exact opposite of Ostwald ripening.

Further studies were conducted by Klabunde and coworkers to explore the digestive ripening process. The process was repeated, this time with DDAB concentration of 0.020M but otherwise identical. In this case, a TEM image was taken after dodecanethiol addition but before precipitation of the nanocrystals. The TEM revealed 2-6 nm spherical nanocrystals.[45] This proves that the addition of thiol immediately affects the gold, converting large prismatic crystals into small spherical nanocrystals within a minute. After reflux for 1.5 hours, the synthesis

yielded 4.7 ± 0.38 nm gold nanocrystals covered in dodecanethiol ($C_{12}H_{25}SH$). This confirmed that smaller nanocrystals grew and larger nanocrystals shrank during reflux.

Different surfactants were then explored, keeping the remainder of the synthesis unchanged. The first set of experiments in 2002 investigated the length of the alkyl chain length in the alkanethiol. When octanethiol ($C_8H_{17}SH$) was added instead of dodecanethiol, the resulting nanocrystals were 4.5 ± 0.34 nm in size. Using decanethiol ($C_{10}H_{21}SH$) produced 4.7 ± 0.23 nm nanocrystals. Due to the measurement error inherent in using TEM for sizing, these populations of nanocrystals are essentially identical. When hexadecanethiol ($C_{16}H_{33}SH$) was used as the surfactant, then the nanocrystals increased in size to 5.5 ± 0.40 nm. The authors also investigated the different nanocrystals' propensity to precipitate in superlattices of nanocrystals, a phenomenon that is critical for applications.[45]

The second set of experiments from the Klabunde group, published in 2003, investigated the effect of the surfactant's head group.[46] The results of this second study were much more profound. Instead of adding dodecanethiol to the polydisperse gold colloid, the authors used different surfactants such as dodecylamine (RNH_2), octadecylsilane ($RSiH_3$), trioctylphosphine (R_3P), dodecyl alcohol (ROH), dodecyl bromide (RBr), dodecyl iodide (RI), and decane (RH). As expected, decane had no effect on the polydisperse nanocrystals. The alcohol and halide surfactants effected a change in the nanocrystals, but not the signature digestion caused by dodecanethiol. Many large prismatic nanocrystals remained intact, and the nanocrystals could not be redispersed in toluene after they were precipitated. However, the amine, phosphine, and silane all caused digestive ripening. Initial addition of the surfactant in each case immediately

digested the polydisperse colloid into smaller spherical nanocrystals, and further reflux until toluene made the nanocrystals more monodisperse. The trioctylphosphine-capped gold nanocrystals were 7.2 ± 1.1 nm in size, the dodecylamine-capped gold nanocrystals were 8.6 ± 1.3 nm in size, and the octadecylsilane-capped gold nanocrystals were 7.2 ± 1.0 nm. This compares with the dodecanethiol-capped gold nanocrystals that were 4.7 ± 0.38 nm in diameter. Clearly, the choice of head group strongly impacts the degree of digestive ripening on the nanocrystals, including whether digestive ripening occurs at all.

The digestive ripening process is remarkable for three primary reasons. First, the TEM images imply that small particles grow and large particles shrink during digestive ripening, which is the exact opposite behavior from particles that are Ostwald ripening. Second, the transition from Ostwald ripening to digestive ripening appears to be a spontaneous event, initiated merely by the addition of the right surfactant. Third, whatever process that is responsible for the digestion of large nanocrystals to small nanocrystals, seems to be unable to digest the smaller nanocrystals any further. This is particularly a strange result in light of the Brust synthesis, which generated smaller 2-nm nanocrystals of identical chemical makeup to the digestive ripening studies above. And the 30:1 thiol-to-gold ratio was employed to ensure that lack of thiol surfactant would not be the governing factor in the final nanocrystal size. Thus, the reason that digestive ripening does not produce even smaller nanocrystals remains a mystery.

Few developments have been made in determining the mechanism of digestive ripening, but the results are useful in our examination. Both electron density functional theory (DFT) examinations and recent experiments have shown that the species bound to gold nanocrystals is

actually thiolate, i.e. the hydrogen on the thiol is not present on the nanocrystal.[85, 86] Gold-silane bonds are shown also to be missing all the hydrogens from the silicon atom.[87] One experiment by Klabunde's group revealed that gold-amine bonds seem to retain their hydrogens.[85] Meanwhile, multiple electron DFT simulations have determined that gold-thiol nanocrystals are covered in thiol-gold-thiol "staples", in which two thiols literally extract a gold adatom from the crystal surface to form a "staple" structure $Au_{(crys)}$-SR-Au-SR-$Au_{(crys)}$.[86, 88, 89] Such staples are also shown to polymerize on a gold nanocluster surface, suggesting the gold-thiolate bond is incredibly strong.[90]

Digestive ripening has been observed for more materials than just gold. The research group of Prasad (once a member of Klabunde's research group) has witnessed digestive ripening for gold, silver, and palladium when either excess dodecanethiol or excess dodecylamine was present.[47] Cobalt has been shown to undergo reversible digestive ripening at room temperature, transitioning easily between monodisperse 6-nm nanocrystals when the oleic acid-to-cobalt molar ratio is 1:5 and dissolved ionic clusters (to be discussed in the next session) with an acid-to-cobalt ratio of 2.5:1, and easily reverting to monodisperse nanocrystals when oleic acid is removed.[48] Other metals have also formed stable, monodisperse nanocrystals in the presence of excess surfactant, though the similarities to the digestive ripening process are inconclusive.[49, 50, 91]

2.5 MOLECULAR CLUSTERS

In 2004 another group was able to digest gold-thiol nanocrystals even further.[92] They used digestive ripening to produce 6.0 ± 0.5 nm nanocrystals, which were precipitated with ethanol,

washed with hexane, and redispersed in a new solution of dodecanethiol (10% by volume) in octyl ether. The thiol-to-gold ratio was ten times higher in the octyl ether solution (~300:1) than in the digestive ripening step (~30:1). This solution was then refluxed at 297°C for 50 minutes and monitored by UV-Vis spectroscopy, shown in Figure 2.3. Absorption at 525nm indicates the presence of crystalline gold in nanocrystals of any size. Over the course of the reflux, this 525nm signal decreases monotonically until it disappears. TEM confirmed that no nanocrystals remained in solution after one hour. At the same time an absorption signal at 305nm appeared and grew in intensity throughout the reflux, a signal that is associated with Au_3 trimers in hexane. In the inset of Figure 2.3, the absorption also reveals a signal at 250nm, also associated with Au_3 trimers in hexane. The solution was dried and laser desorption/ionization mass spectrometry was performed on the dried remnants. The laser irradiation data suggested Au-S and S-C bonds were broken in the ionization process. Mass spectrometry yielded 3 peaks (*m/z* = 197.2, 394.1, and 591.5) which were unambiguously assigned to gold ions (Au^+), gold dimers (Au_2^+), or gold trimers (Au_3^+). This led to the conclusion that the 6-nm gold nanocrystals had been further digested into "molecular clusters" of $Au_3(C_{12}H_{25}S)_3$. DFT investigations of gold-thiolate molecular clusters have shown that such a species is stable, but only in a "ring" formation, i.e. where every gold atom is bonded to two thiolates and not to the other gold atoms.

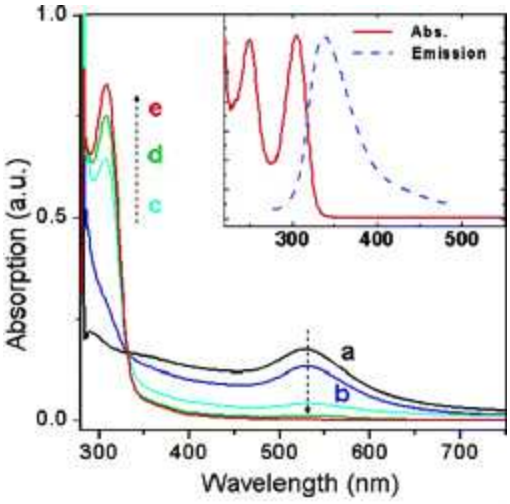

Figure 2.3: UV-Vis absorption spectroscopy measurement of gold-thiolate nanocrystals (absorbance at 525 nm) dissolving and converting to gold-thiolate molecular clusters (absorbance at 305 nm and [inset] 250 nm). [92]

The findings of the gold-thiol molecular cluster synthesis suggest more questions about the digestive ripening process. Polydisperse nanocrystals up to 80 nm in size are digested by thiols down to 2-6 nm nanocrystals within a minute at room temperature, at which point no further digestion is observed despite the excess concentration of dodecanthiol. Those same nanocrystals are heated to 300°C in the presence of excess thiol, and further digestion does occur but takes nearly an hour. The two rates of digestion are so dramatically different that the thermodynamic forces acting on them must be dramatically different in magnitude, and perhaps different in nature.

Multiple metal-surfactant pairs have been shown to produce molecular clusters as well as monodisperse nanocrystals.[48, 49, 93] When iron carbonyl ($Fe(CO)_5$) is thermally decomposed in dichlorobenzene in the presence of oleic acid, iron-oleate molecular clusters are formed. When an iron-oleate complex (a polymerized version of the molecular cluster) is heated in octadecene, the oleates decompose into aldehyde and the leftover oxygen combines with iron ions to form monodisperse, stable Fe_2O_3 nanocrystals covered in oleates. Amine-coated palladium nanocrystals will decompose in the presence of dodecanethiol and form a "tiara" molecular complex, Pd_6RS_6 (shown in Figure 2.4 and known to have an analogous "ring" formation of gold-thiolate molecular clusters). Cobalt will form molecular clusters in the presence of excess oleic acid or in the presence of excess trioctylphosphine oxide, but monodisperse Co nanocrystals are formed when less oleic acid or trioctylphosphine oxide is present than cobalt. The cobalt system is interesting because it is

Figure 2.4: Tiara-structure of Pd(II) thiolate, $[Pd(SC_{12}H_{25})]_6$, as characterized by X-ray single crystal analysis, elemental analysis, MALDI, 1H NMR, and powder XRD. [93]

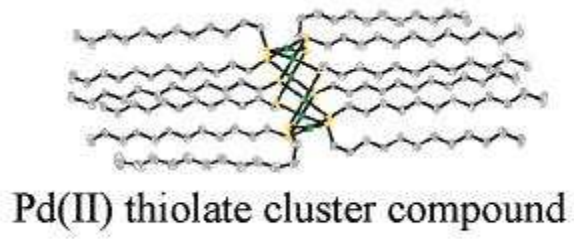

reversible: adding more surfactant to Co nanocrystals digests them into molecular clusters, and reducing and precipitating the surfactant (using $LiAlH_4$) from molecular clusters re-crystallizes them into monodisperse nanocrystals. The global nature of observing molecular clusters made from the same materials as surfactant-coated stable nanocrystals suggests a common physical process governing both of their synthetic behavior. Therefore, any theory pertinent to digestive ripening must address the case of molecular clusters to properly account for all possible physical products of a given synthesis.

The synthesis that is most pertinent to this study was conducted in 2012 by FuKe Wang et al. in the reversible transition between gold-thiol nanocrystals and gold-thiol molecular clusters.[94] Klabunde's digestive ripening work shows that 4.7-nm nanocrystals are stable in the presence of excess alkanethiol even at 100°C. The work by Wang et al. reveals that 10-nm gold nanocrystals can be digested down to molecular clusters *at room temperature* if an *aromatic* thiol is employed, such as naphthalene thiol or phenylthiol. Furthermore, if the resultant molecular clusters are exposed to H_2O_2, monodisperse gold nanocrystals are again formed. Figure 2.5

Figure 2.5: Reversible dissolution of gold nanoparticles (red solution) by the addition of naphthalene thiol into a clear solution of gold-thiolate molecular clusters, $Au(NaphS)_2$, and the regeneration of nanoparticles by addition of H_2O_2. [94]

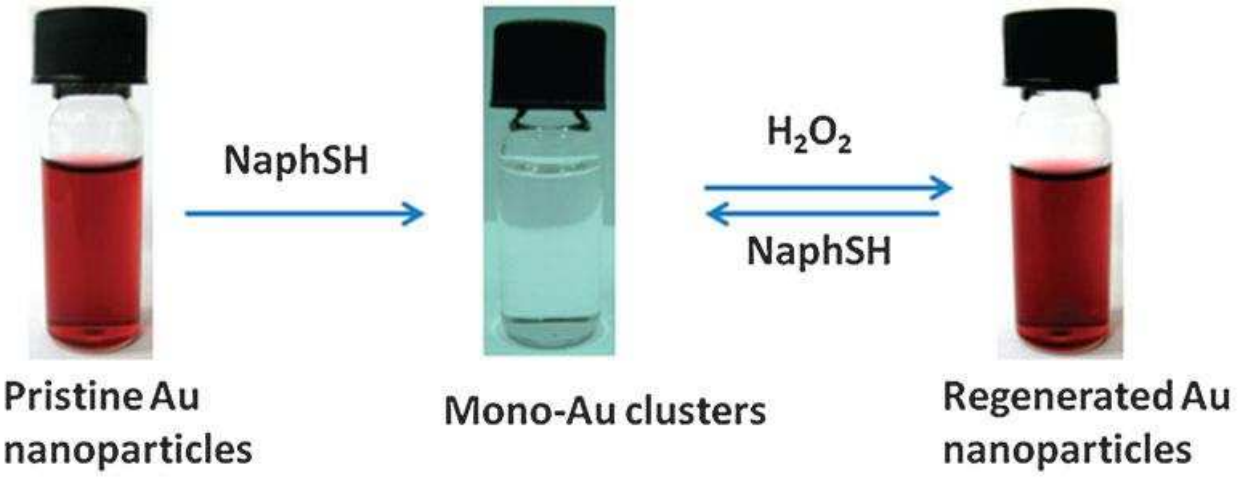

illustrates this reversible process. The authors conjecture that aromatic thiol is more acidic and will dissociate into thiolate and hydrogen ions at a gold surface much more readily than an alkanethiol in equivalent conditions.[94]

2.6 GOLD-THIOLATE COMPLEXES AS PRECURSORS

A recent development in the synthesis of gold-thiol nanocrystals is the use of gold(I)-thiolate precursors.[95-98] This development presents an additional dimension to the systems described above. The gold(I)-thiolate complex is a waxy polymeric species that appears to have a similar local structure to gold-thiolate molecular clusters. Gold(I)-thiolate polymer can be reacted to form gold nanocrystals under certain conditions: (1) if the gold(I)-thiolate is exposed to TEM electron beams,[97] (2) if the gold(I)-thiolate is heat treated up to 160°C in air,[98] and (3) heat treatment in the solid state are some examples.[96] Multiple studies of these systems suggest that, outside of organic solution (which makes these system dubiously comparable to digestive ripening) multiple gold(I)-thiolate monomers are reduced to a thiolate-coated gold nanoparticle mixed with a large number of disulfides. The energy required to undergo this transformation in all three cases is much higher than the energy delivered to gold-thiolate nanocrystals during digestive ripening, though it is perhaps comparable with the energy delivered to gold-thiolate nanocrystals at 300°C when molecular clusters were formed. No studies have examined the behavior of these particle in the presence of disulfides if they were placed in solution.

Figure 1.1: Time-wise evolution of the Stucky synthesis of gold nanocrystals showing continuous nucleation of new particles. [99]

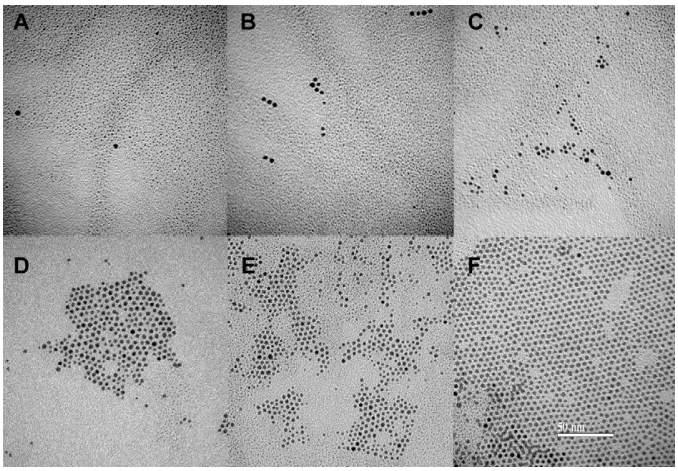

2.7 THE STUCKY SYNTHESIS

The primary disadvantages to the Brust synthesis, including the modified syntheses that lead to digestive ripening, are that it requires two liquid phases and that the reduction by $NaBH_4$ occurs too quickly to control. Much attention was paid to developing synthetic routes for monodisperse nanocrystals that involved one phase and a slower reaction, which would lower the overall cost of producing application-ready nanocrystals in large quantities. The Stucky synthesis accomplished these goals for gold-thiolate nanocrystals by employing a new gold precursor, triphenylphosphine gold chloride ($ClAuPPh_3$), and a slow reducing agent than $NaBH_4$, namely *tert*-butylamine-borane complex, $(CH_3)_3CNH_2{:}BH_3$.[99] These chemicals were added to benzene in the presence of dodecanethiol (2:1 thiol-to-gold ratio) to produce monodisperse gold-thiolate nanocrystals.

Certain aspects of the synthesis encourage comparison to digestive ripening. First, TEM micrographs show that the gold-thiolate nanocrystals do not grow with time. Rather, the number of nanocrystals increases rather dramatically from 5 to 60 minutes (see Figure 2.6). The final size of the gold nanocrystals did depend on temperature: 5.3-nm nanocrystals at room temperature

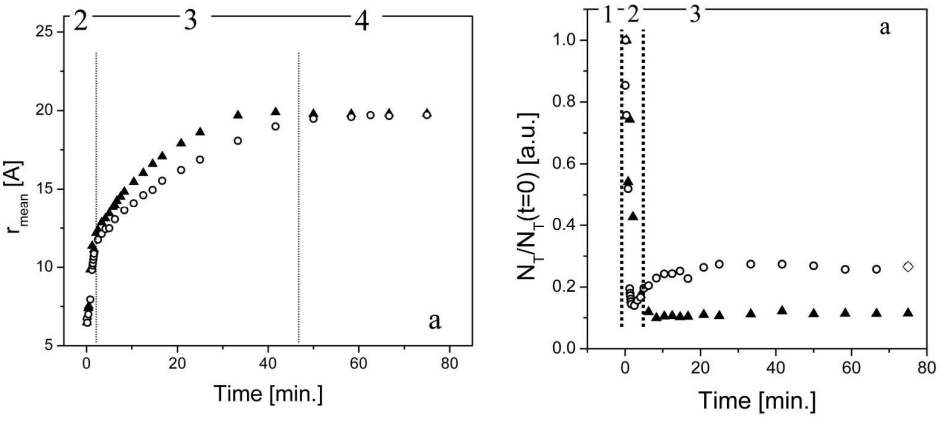

Figure 2.7: Results from a modified Stucky synthesis, which shows nucleation ceases early and instead growth persists through most of the synthesis. [100]

(after 1 hour), 6.2-nm nanocrystals at 55°C (after 5 minutes), 7.1-nm nanocrystals at 85°C, and 8.3-nm nanocrystals at 100°C. More polar solvents yielded smaller nanocrystals than the organic solvents. Finally, different surfactants yielded nanocrystals of different sizes and qualities. Just as in digestive ripening, the dodecylamine-coated nanocrystals were larger and more polydisperse than the thiolate-protected nanocrystals.[99]

Very recently, Koerner et al. using the same overall synthesis was published that examined the effect of gold-to-reducer ratio and of the alkylthiol's length.[100] Stucky's protocol was employed, thus with dodecanethiol and a gold-to-reducer ratio of 1:11, but with one modification: the thiol-to-gold ratio was 1:1 instead of Stucky's 2:1. The differences in the results were striking: the number of nanocrystals remained constant throughout Koerner's synthesis and the nanocrystal size grew appreciably, as shown in Figure 2.7. Both syntheses seem to show that Au^0 is produced over time; Stucky's results implied that the Au^0 simply nucleated more new nanocrystals while the average size stayed constant, while Koerner's results showed gold nanocrystals growing as a result of Au^0 production, while the nanocrystal number remained constant. As was witnessed in digestive ripening, the alkyl chain length on the thiol molecule had little effect on the final size, though the timescale of the reaction was affected. The ratio of reducing agent to gold precursor had a larger impact on the final size, suggesting these nanocrystal syntheses are less dependent on thermodynamics and more kinetics.[100]

2.8 ANISOTROPIC NANOCRYSTALS

In the last decade, a different branch of nanocrystal synthesis emerged as anisotropic nanocrystals were created and studied: nanorods, nanoplates, nanoprisms, nanocubes, nano-

polyhedra, nanotetrapods, nanohexapods, nanoshells, nanocages, and many other irregular structures have been synthesized out of various crystalline materials.[101, 102] Each shape of an anisotropic nanocrystal is characterized by several length scales, which results in fascinating behavior for materials with size-dependent properties. As an elementary example, semiconductor nanorods have been used in solar cells, where the rod diameter controlled the band gap and absorption efficiency and electron transport occurred mostly along the (adjustable) long axis.[12] Less straightforward examples of anisotropic nanocrystal applications include using gold nanorods as glucose sensors and optimizing platinum nano-polyhedral calalysts using its facet-dependent catalytic selectivity.[103, 104] Anisotropic nanostructures are of enormous importance to 21st century nanotechnology and the development of this field could be vastly accelerated by quantitative theoretical investigations of spherical nanocrystals. Such theories have the potential to be generalized for arbitrary shapes and anisotropic growth.

2.9 THEORETICAL INVESTIGATIONS OF NANOCRYTALS

A great deal of attention has been paid to describing nanocrystals in a theoretical sense. Density functional theory (DFT) analyses are extremely common to determine the molecular structure of nanocrystals and their surfactant coatings, as well as to interrogate what processes give them their quantum and optical properties.[86, 105-107] Some DFT studies are energetic in nature to analyze the favorability of a species and the activation barriers of its construction.[57, 108] Additionally, a few numerical solutions to nanocrystal growth have been conducted in the last decade. These simulations take the same governing equations used in the development of LSW theory and generalize the system in some particular fashion beyond LSW theory's assumptions.[39-41] The results are solved for numerically, but critical parameters are often

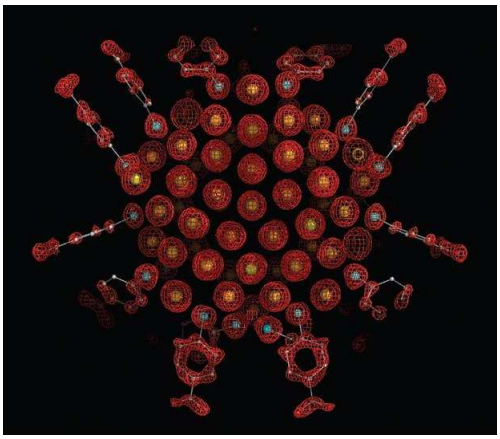

Figure 2.8: Density functional theory (DFT) analysis of gold-*p*-mercaptobenzoic acid, $Au_{102}(p\text{-}MBA)_{44}$, showing the electron density map and optimized molecular structure. [86]

chosen arbitrarily or a parametric study is done with no indication of what parameters choices are best. As such, little mechanistic insight has been gained through these particular techniques, although a variety of experimental data has been matched through the numerical schemes.

These studies represent a kind of "digital experiment" in which a particular mathematical system is interrogated and measured through a particular lens. Numerical solution of any mathematical system, whether algebraic, differential, or otherwise, requires that all input parameters must be chosen *a priori*, often without any reference from experimental systems. Exploration of how these different parameters affect the results are possible, but just as in real experiments the phase-space of all the different parameters is so huge that such an investigation is impractical. Additionally, even in the event of full parametric investigations that leave no experimental system unexplored, correlated variables and a failure to map the resultant data are still barriers to extracting critical insights. In this way, numerical studies and simulations are exactly like experiments, providing only results instead of reasons.

Analytic-theoretical examinations, in which a series of model equations is developed and manipulated to determine critical relations among the system's conditions, provide much more information about these systems. However, there are very few such theoretical studies of nanocrystals. There are five primary theories that describe nanocrystal growth so far witnessed in the literature: LSW theory of Ostwald ripening[54-56], Sugimoto's qualitative treatment of size-

narrowing[69], the Leff treatment of gold-thiolate nanocrystals[74], a theoretical treatment of the focusing-Ostwald ripening transition by Dushkin et al.[38], and the electrostatic theory of digestive ripening by Lee et al.[109]

LSW theory is explained in complete detail in Chapter 3 and will not be addressed here. Briefly, the theory provides a wealth of information but is severely limited to Ostwald ripening systems, describing only the behaviors of nanocrystal that are least preferred.

Sugimoto analyzed the governing equations of LSW theory in 1987 and extrapolated the possibility of forcing the particle distribution to become narrower, which inspired Peng et al.'s size focusing study. However, his conclusions are only qualitative in nature and provide no quantitative framework for controlling size focusing explicitly. The goal was to develop monodisperse micron-size crystals, thus the qualitative analysis was sufficient, but a higher degree of theoretical robustness is necessary if those same principles are to be applied quantatively to nanocrystal syntheses.

Leff et al.'s theoretical treatment of gold-thiolate nanocrystals begins with a general thermodynamic treatment, similar to the Israelachvili treatment of micelles.[74, 110] A total free energy function is declared and minimized subject to two constraints, namely the mass balances on the gold and the thiols, using Lagrange multipliers λ and λ* to develop this equation:

$$X_n = n \exp\left(\frac{\mu_n^0 + \lambda n + \lambda^* n_{thiol}}{kT} \right) \tag{2.1}$$

Leff and coworkers proceed to declare that λ and λ* are the chemical potentials of gold and thiol respectively, and arbitrarily subsume them into the thermodynamic relation above. Such a result already diverges from the Israelachvili theory for micelles: the thermodynamic dependence on X_1, the concentration of gold monomers in solution, has been commuted and is not included in the theory. The model then employs a series of semi-quantitative values to describe the free energy of a surfactant-coated nanocrystal. Although the paper describes how the function is formed, no algorithm or computation is mentioned to find the maximum value of X_n in Eq. (2.1) above. Theoretical results are obtained and compared against experimental results, but it is ambiguous how the theoretical results are computed. No thermodynamic forces are suggested that determine the equilibrium size of the gold-thiolate nanocrystals. In summary, the theory is incomplete and does not properly account for experimental observations made in the intervening 17 years, such as molecular clusters or the dependence on surfactant binding energy on size.

In 2000 Dushkin et al. published a comprehensive analysis of CdSe nanocrystals with specific details regarding their synthesis and characterization.[38] Accompanying the experimental study was a theoretical investigation of the growth kinetics of nanocrystals. The model is meant to account for the transition from size focusing, which was poorly understood, into Ostwald ripening, which was well understood. Unfortunately, the particle growth rate employed in the Dushkin model was in explicit disagreement with the growth rate used in LSW theory and analyzed by Sugimoto. While the LSW growth rate represent a harmonic average between diffusion and surface reaction, which is in better agreement with other mass transfer processes, the Dushkin model uses an arithmetic average between diffusion and surface reaction. LSW theory and the Sugimoto analysis have been successful at describing many nanocrystals' growth

behavior, implying that the harmonic-average rate is more accurate. It is unlikely that the Dushkin model's arithmetic-average rate can capture the same dynamics with such accuracy, and the extrapolations from that rate are put in doubt for the inability to agree with the well-established LSW theory.

The electrostatic model by Lee et al. is somewhat more comprehensive but still fails to thoroughly account for digestive ripening.[109] The postulate of this model is that an accumulation of *z* electric charges on a gold nanocrystal is responsible for digestive ripening and the formation of a stable size. The chemical potential of a nanocrystal (of radius *R*) is developed which comprises the surface tension term plus the free energy of having *z* similar charges lying on its surface. With no charges, the chemical potential monotonically decreases, indicating that bulk gold is preferred. When a number is chosen for *z*, the chemical potential goes to negative infinity as the radius goes to zero. The chemical potential has a maximum at a finite *R* after which it decays to an asymptotic value with increasing radius. The result, according to the authors, is that for particular concentrations there is a stable size. For certain concentrations, there are two radii, r_a and r_b, for which the chemical potentials of the dissolved monomers and the adsorbed monomers is the same (see Figure 2.9). The value r_b is an unstable radius such that particles $r < r_b$ shrink and particles $r > r_b$ grow. The radius r_b indicates Ostwald ripening occurs in that regime. The other, smaller

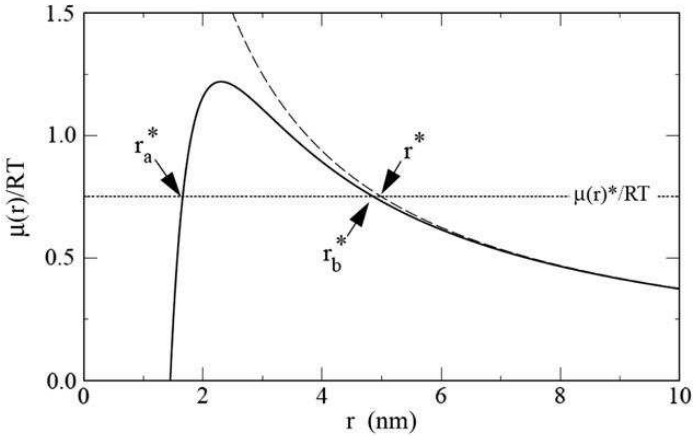

Figure 2.9: Chemical potential of spherical nanoparticles with a presumed electrostatic contribution (solid line) and the classical model without electrostatics (dashed line). The quantity μ(r)* is the chemical potential of dissolved monomers in solution. [109]

radius r_a is stable such that all larger sizes shrink away from r_b, but all smaller sizes grow to increase the particle size and thereby reduce the electrostatic repulsion of the z charges on the surface. The chemical potential curve suggests coexistence between bulk gold and nanocrystals at r_a at equilibrium.

There are a number of issues with the electrostatic model, however. The first is that it excludes the surfactant entirely and offers no explanation for the experimental determination that different surfactants yield different nanocrystal sizes. In fact, the formulation as stated suggests that charge alone causes digestive ripening. No explanation is provided for why bare gold nanocrystals do not exhibit this behavior. Within the framework of the electrostatic model, the smallest gold clusters are claimed to be less favorable than a larger crystal due to electrostatic repulsion. Meanwhile, the model presumes that these clusters will adsorb monomers and grow instead of simply flying apart into component monomers in an inverse-nucleation event. Finally, one detail of the formulation has no physical basis: when z is selected, it is presumed constant with radius. Thus, for $z = 20$ representing twenty charges on the nanocrystal, the model assumes that a micron-sized piece of gold, a 10-nm nanocrystal, and a cluster of 4 gold atoms all bear exactly 20 charges on their surfaces.[109] Physically speaking, z is much more likely to vary with either volume or surface, and the fraction of charged atoms would remain the same. In either of these cases, the mathematics behind the electrostatic model are drastically changed: the charge term no longer diverges to $-\infty$ at zero radius, and no stable chemical potential is present. This model of electrostatics-driven digestive ripening is at best overly specific and at worst erroneous.

With the exception of the ideas published in this thesis, no other analytic-theoretical treatment of nanocrystal growth is found in the literature. As stated above, only the LSW theory of Ostwald ripening provides a completely comprehensive, global, and accurate description of any nanocrystal growth process. Meanwhile, the phenomena of size focusing and digestive ripening are mysterious because they violate LSW theory and they do not behave like other Ostwald ripening systems.

2.10 THE MYSTERIES OF MONODISPERSE SPHERICAL NANOCRYSALS

It is the goal of this thesis to fill in the gaps in our understanding of spherical nanocrystals and how they grow. There are five primary mysteries of spherical nanocrystals that lie outside the realm of Ostwald ripening, and providing a theoretical description that solved these mysteries is essential to graduating such systems into the world of factory-scale production and application.

The five mysteries are as follows:

(1) What processes govern the rate, degree, and extent of size focusing?

(2) What effect do surfactants have on nanocrystals that are Ostwald ripening?

(3) Why do some surfactants halt Ostwald ripening and cause digestive ripening?

(4) What environmental conditions lead to molecular clusters vs. digestive ripening?

(5) What controls the size of digestively ripening nanocrystals?

The theoretical works provided in this thesis will answer these questions. Where assumptions are made, their effect on the quantitative accuracy will be noted, but the key goal of all these

formulations is to examine the physical causes of the target processes. The insights gained will enhance our ability to control and direct nanocrystal growth, even in some cases providing a model framework for the optimization and *a priori* design of nanocrystal syntheses and manufacturing processes.

CHAPTER 3

THE LSW THEORY OF OSTWALD RIPENING

3.1 OSTWALD RIPENING

The process of Ostwald ripening was first described by Wilhelm Ostwald in a book published in German in 1896; the first English representation appeared in 1900.[25] Ostwald ripening occurs mostly in colloids, but also in emulsions, alloys, and other fluid systems where two phases are separating. In this phase separated system, the insoluble solute has partially precipitated into clusters dispersed in the solvent. The clusters are generally dilute, thus the pair-wise interactions between clusters are rare: this differentiates Ostwald ripening from agglomeration or coalescence of clusters into a continuous phase.

Primarily, each cluster interacts only with the surrounding solution. Ostwald observed that small clusters in solution would shrink, becoming dissolved solute, and that larger clusters would grow by redeposition of the recently-dissolved material from the shrinking clusters. The overall trend suggests the system was minimizing its surface-to-volume ratio and it would only stop once phase separation was complete.

3.2 THE GIBBS-THOMSON EFFECT

The thermodynamic basis for why different-sized particles have different growth rates, even in the same solution, is given by the Gibbs-Thomson equation or Kelvin equation. The fundamental concept concerns the interface between the condensed phase and the solution: when this interface is flat, then adding or removing material only changes the volume of the condensed phase.

However, adding new material to a finite cluster with a curved interface causes both the volume *and the surface* of the cluster to change. Therefore, the chemical potential of material in the cluster will depend on its size. If the free energy of a spherical cluster contains a volume term and a surface term

$$G = \frac{4\pi R^3}{3v} g_{cond} + 4\pi R^2 \gamma \tag{3.1}$$

then the standard chemical potential of the solute in such a particle is given as follows:

$$\mu_R^0 = \left(\frac{\partial G}{\partial N}\right)_{T,P} = \left(\frac{\partial G}{\partial R}\right)_{T,P} \frac{v}{4\pi R^2} = g_{cond} + \frac{2\gamma v}{R} \tag{3.2}$$

At equilibrium, the chemical potential of the condensed phase, $\mu_R = \mu°_R$, equals the chemical potential of the dissolved phase at concentration c. For a flat surface, this equilibrium concentration is simply the solubility, $c_\infty = \exp(\beta g_{cond})$. Eq. (3.2) therefore provides how the solubility is different near a curved surface with radius of curvature R:

$$c_R = \exp\left(\frac{g_{cond}}{kT} + \frac{2\gamma v}{RkT}\right) = c_\infty e^{\frac{2\gamma v}{RkT}} \tag{3.3}$$

Eq. (3.3) is the Gibbs-Thomson equation. It reveals that the high surface-to-volume ratio of the smallest clusters makes them exponentially more amenable to dissolving than a larger cluster or a flat surface.

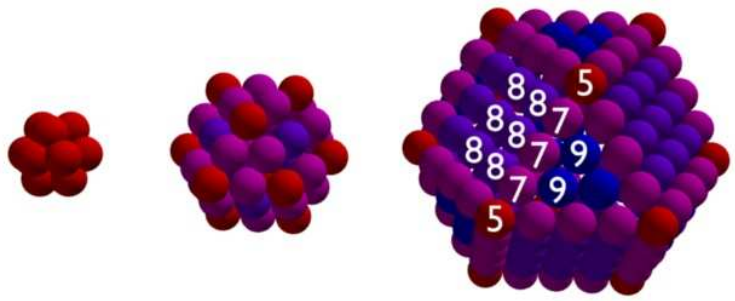

Figure 3.1: Nearest-neighbor (nn) coordination number of the surface atoms in small f.c.c. clusters. Vertex (red) atoms have 5 nn; edge (purple) atoms have 7nn; face (blue) atoms have 8 or 9 nn. The vertex (red) atoms are more weakly attached than the face (blue) atoms. Average coordination increases with cluster size.

There is an equivalent atomistic understanding of the Gibbs-Thomson equation which is more intuitive. For any crystal, a molecule on the surface is coordinated to fewer neighbors than a molecule in the interior phase. Any finite-size crystal (i.e. a closed volume) must have multiple facets that connect to each other at edges, and the edges join together at vertices. The molecules in the bulk, on a face, at an edge, and at a vertex all have different coordination numbers. A bulk molecule has the most neighbors (i.e. 6 in a cubic crystal or 12 in an f.c.c. crystal), a vertex molecule has the fewest (i.e. 3 in cubic or 5 in f.c.c.), and molecules on a face and at an edge have a coordination number in between. This is represented in Figure 3.1, with color-coding to denote the face (blue), edge (purple), and vertex (red) molecules. Statistically, vertex molecules are the weakest-bound molecules and are thus most likely to desorb. As radius decreases and the surface curvature increases, the fraction of edge- or vertex- molecules increases, and the overall likelihood of a surface molecule desorbing from the crystal increases accordingly. The Gibbs-Thomson effect in Eq. (3.3) reflects the Boltzmann-weighted probability a surface molecule will desorb from an R-sized crystal, which increases exponentially as the crystal gets smaller. At equilibrium, when the probabilities of desorption and adsorption are equal, a higher dissolved-molecule concentration is needed around a more-curved crystal, thus the solubility is higher near

an *R*-sized crystal. In a continuous and compressible phase space, the same analogy applies and the result is the Laplace pressure.

3.3 THE GROWTH RATE OF A SINGLE PARTICLE

This section is a kinetic derivation of *dR/dt*, the growth rate of a single spherical particle in a solution of solute molecules (called "crystal monomers") at a concentration c_b. The derivation has been repeated elsewhere, among other places in Mantzaris' treatment of Ostwald ripening.[41] If the particle is suspended in the solution, then it simultaneously experiences adsorption of monomers from solution and desorption of monomers from its surface. The net growth rate depends on the combined average rates of these two processes, as derived here.

The adsorption rate is assumed to be a first-order surface reaction versus the solute concentration at the interface, c_i, with reaction rate constant k_s (the units of k_s are length/time). Meanwhile, the desorption rate is proportional to the Gibbs-Thomson solubility, thus smaller particles will lose their surface atoms more quickly. Desorption has its own rate constant k_d but most literature sources simply replace it with k_s for convenience. (It is pointed out below that the the assumptions of $k_d = k_s$ and of first-order kinetics are not necessary in the theoretical analyses to follow.) The analysis is limited to nearly spherical crystals which can be characterized only by their radius *R*. By combining these results, the rate of change of the total number of

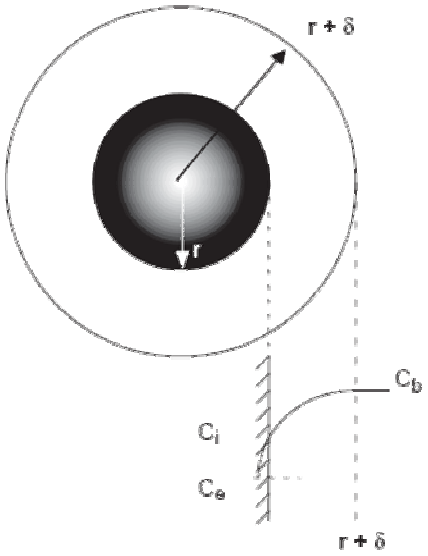

Figure 3.2: Schematic of the diffusion layer around a particle, with concentrations c_b and c_i at the bulk and the surface respectively. [41]

solute molecules in the spherical particle is equal to the net sorption over its surface:

$$\frac{d}{dt}\left(\frac{4\pi R^3}{3v}\right) = 4\pi R^2 k_s \left(c_i - c_\infty e^{\frac{2\gamma v}{RkT}}\right) \tag{3.4}$$

For a quantitative analysis c_i must be determined using transport phenomena. An adsorbing (or desorbing) monomer at the interface must travel between the bulk solution and the interface by diffusion. There is a presumed diffusion layer of thickness δ around the particle. The bulk solution conditions are met at a distance $r = R + \delta$ from the particle center, and the monomers diffuse freely in the range $R < r < R + \delta$. Figure 3.2 illustrates the spherical particle and the diffusion layer around it.[41] The following assumptions are made about this diffusion layer:

(1) There is negligible convection.

(2) Monomers are neither produced nor consumed in the layer.

(3) The diffusion layer is much larger than the particle, $\delta >> R$.

and

(4) The particle surface's motion (due to growth) is much slower than monomer transport.

Motion of the solute in the diffusion layer therefore reduces to a diffusion-only process, and the solute material balance is simply the Laplace equation in spherical coordinates:

$$D\nabla^2 c(r) = 0 \tag{3.5}$$

with solution $c(r) = A + B/r$. There are two boundary conditions: a Dirichlet boundary for the bulk solution, $c(r) = c_b$ at $r = R + \delta$; and a Robin boundary condition at the particle surface, where the diffusive flux $J = D\,\partial c/\partial r$ at $r = R$ equals the reactive flux $J = \nu k_s(c_{r=R} - c_\infty e^{2\gamma w/RkT})$. Although the surface R is changing with time, assumption (4) allows us to neglect the time-dependence of R relative to diffusion. Employing assumption (3) above, the full solution to Eq. (3.5) is therefore

$$c(r) - c_\infty e^{\frac{2\gamma w}{RkT}} = \left(c_b - c_\infty e^{\frac{2\gamma w}{RkT}} \right) - \frac{k_s R}{D}\left(c(r = R) - c_\infty e^{\frac{2\gamma w}{RkT}} \right)\frac{R}{r} \tag{3.6}$$

The concentration at the particle surface $c(r=R)$ is evaluated and included in Eq. (3.4). The result simplifies to the equation for the single-particle growth rate in a solution of concentration c_b:

$$\frac{dR}{dt} = \nu \frac{Dk_s}{k_s R + D}\left(c_b - c_\infty e^{\frac{2\gamma w}{RkT}} \right) \tag{3.7}$$

Finally, note that the single-particle growth rate has two limiting case: "diffusion-limited growth" in which $D << k_s R$ and "reaction-limited growth" in which $k_s R << D$, giving these two simplified forms of the single-particle growth rate:

$$\frac{dR}{dt} = \nu \frac{D}{R}\left(c_b - c_\infty e^{\frac{2\gamma w}{RkT}} \right) \tag{3.8a}$$

$$\frac{dR}{dt} = vk_s\left(c_b - c_\infty e^{\frac{2\gamma}{RkT}}\right) \tag{3.8b}$$

We note several important details before proceeding. First, for small R the exponential term always dominates and the result is that particles near the limit $R = 0$ are always shrinking for any concentration c_b. Second, there always exists a radius R_c at which $c_b = c_\infty \exp(2\gamma/R_c kT)$ and a particle of that radius is neither growing nor shrinking. This radius R_c is defined the "critical radius". Third, the reaction-limited expression is monotonically increasing, while the diffusion-limited expression sees a maximum and decreases as $R \rightarrow \infty$.

Our focus in this thesis will be almost exclusively on the diffusion-limited growth expression. The reaction-limited system has been treated by the equivalent step-by-step analysis, but only the results are given here, to differentiate the experimental behavior in the two regimes.

3.4 LIFSHITZ-SLYOZOV-WAGNER (LSW) THEORY

A quantitative kinetic theory of Ostwald ripening was developed in April 1961, when Lifshitz and Slyozov out of the USSR published their theory of precipitation.[54] In September of that same year, Wagner from the Max Planck Institute submitted a theory of Ostwald ripening which cited the Lifshitz and Slyozov paper and provided the exact same quantitative conclusions.[55] However, Wagner used a very different mathematical treatment to solve the diffusion-limited Ostwald ripening process, and Wagner also extended the treatment to examine the reaction-limited ripening, which Lifshitz and Slyozov neglected. Wagner's treatment is more approachable, while Lifshitz and Slyozov's treatment is more mathematically rigorous. The two

treatments provide identical quantitative size distribution functions and growth laws, and the unified theory of precipitation and Ostwald ripening is now known as "LSW theory".[56]

The core result of LSW theory is the solution of three governing equations. The first is the single-particle growth rate *dR/dt* derived above in Eq. (3.8). The second is a global material balance on the monomers, including all dissolved monomers and all material in the particles, expressed in an instantaneous rate-of-change format:

$$\frac{dc_b}{dt} = -\frac{d}{dt}\int_0^\infty \frac{4\pi R^3}{3v} f(R,t)dR = -\frac{d}{dt}\int_0^\infty \frac{4\pi R^2}{v}\frac{dR}{dt} f(R,t)dR \tag{3.9}$$

Here, *f(R,t)* is the time-dependent size distribution function of all the nanocrystals in the system, i.e. the probability density of having a particle of radius *R* at time *t*. The third and final equation is the continuity equation on *f(R,t)*, which establishes that the probability *f(R,t)* only changes from smaller particles grow to size *R*, from larger particles shrinking to size *R*, and from spontaneous generation of *R*-sized particles. In Ostwald ripening, particles are not spontaneously generated and the growth rate *dR/dt* determines the net motion of particles in *f(R,t)*. The time-wise evolution of the size distribution function in the absence of nucleation is therefore:

$$\frac{\partial f}{\partial t} = -\frac{\partial}{\partial R}\left(f \frac{dR}{dt} \right) \tag{3.10}$$

(A note: the notation used here is an amalgam of the notation used by Liftshitz and Slozov and the notation used by Wagner.) A general solution to these governing equations is intractable as

stated. A series of assumptions is therefore applied such that the problem becomes tractable while still being physically relevant. These assumptions apply in addition to the first four assumptions made in constructing *dR/dt*:

(5) the exponential Gibbs-Thomson term is approximated by its linear Taylor expansion,

(6) the fraction of monomers that are dissolved is negligibly small, therefore $dc/dt \sim 0$,

(7) only diffusion-limited (3.8a) and reaction-limited (3.8b) growth are explored

and

(8) the size distribution function *f(R,t)* can be treated by separation of variables.

This last assumption is proven by Lifshitz and Slyozov to calculate a form for *f(R,t)* that is asymptotically accurate with time. We will only derive the diffusion-limited growth case here, as this is the case most often cited in the literature for describing nanocrystal growth.

Linearizing the Gibbs-Thomson term allows for a change of variables, and the single-particle growth rate may be restated in a more convenient format:

$$\frac{dR}{dt} = \frac{K_D}{R^2}\left(\frac{R}{R_c} - 1\right) \tag{3.11}$$

where R_c is the critical radius defined above (such that $dR/dt \mid_{Rc} = 0$) and K_D is the LSW constant $K_D = 2\gamma w^2 c_\infty D/kT$. R_c changes with c_b and is time-dependent, while K_D is a function only of temperature. Inserting this new compact form of the single-particle growth rate Eq. (3.11) into

the global material balance Eq. (3.9) and applying assumption (6), $dc/dt \sim 0$, yields the very simple but informative result:

$$\int_0^\infty \frac{4\pi R^2}{v}\frac{K_D}{R^2}\left(\frac{R}{R_c}-1\right)f(R,t)dR = \frac{\langle R\rangle}{R_c}-1=0 \qquad (3.12)$$

This means a behavior-determining quantity, R_c, is related to an observable quantity $\langle R\rangle$, the average particle radius. It will be shown later that LSW theory derives an equation for $R_c(t)$ which therefore yields a growth law $\langle R\rangle(t)$ which can be confirmed by direct experimental observations. Furthermore, ripening experiments observe the average radius (thus R_c) to increase with time.

(We previously stated that the assumptions of $k_s = k_d$ and of first-order adsorption kinetics are not necessary. It is the use of R_c which obviates these assumptions, because R_c incorporates all the arbitrary kinetics of sorption into a single parameter. Furthermore, the rate constants k_s and k_d and the bulk concentration c_b never appear in other equations, and R_c will never be explicitly evaluated because $R_c = \langle R\rangle$. The net result is that the behavior of Ostwald ripening has no dependence on the details of the sorption kinetics.)

The remaining derivation of LSW solves for the size distribution function $f(R,t)$ that describes an Ostwald ripening system. Both papers declare that in the limit $t \to \infty$, the function $f(R,t)$ will have a constant shape when normalized around $R = R_c$ and only its height and width will evolve with time. Therefore, $f(R,t)$ is described through a mixture of combination-of-variables, in which

a dimensionless radius $\rho = R/R_c(t)$ is defined, and separation-of-variables, in which $f(R,t)$ is expressed as a product of a function of time and a function of ρ:

$$f(R,t) = g(t)\rho^2 h(\rho)$$

The factor of ρ^2 comes from the boundary condition at $R = 0$. The particles are known to dissolve away into monomers as their size approaches zero, and this represents a decrease in the total number of particles. Let $Z(t)$ be the number concentration of particles in the system, equal to the integral of f over all R, and let us calculate its rate of change using dR/dt and Eq. (3.10):

$$\frac{dZ}{dt} = \frac{d}{dt}\int_0^\infty f(R,t)dR = \lim_{R\to 0} f(R,t)\frac{dR}{dt} = \lim_{R\to 0} f(R,t)\frac{K_D}{R^2} \tag{3.13}$$

Since the quantity dZ/dt is neither infinite (unphysical) nor zero (because the total amount of material is constant but the average size is increasing), clearly $f(R,t)$ goes as R^2 or ρ^2 near $R = 0$. The equation for dZ/dt is additionally useful to determine the rate dR_c/dt. While the details are described in Appendix A, the result is the following:

$$\frac{dR_c^3}{dt} = \frac{K_D}{\gamma_D} \tag{3.14}$$

where

$$\gamma_D = \int_0^\infty \rho^2 h(\rho) d\rho \tag{3.15}$$

The entire system of equations has now been reduced to two unknowns: the function $h(\rho)$ and the value of γ_D, which are explicitly related. Wagner solves them simultaneously as follows: the asymptotic form of $f(R,t)$, the expression for $g(t)$, the time-derivative of ρ, and the value γ_D are all plugged into the continuity equation (3.10). Taking note that $d\rho/dt = \rho/R_c \, dR_c/dt$, the two-variable partial differential equation simplifies to an ordinary differential equation in ρ only, as follows:

$$\left(\frac{\rho^3}{\gamma_D} - 3\rho + 3\right)\frac{dh}{d\rho} + \left(\frac{6\rho^2}{\gamma_D} - 3\right)h(\rho) = 0 \tag{3.16}$$

In solving for $h(\rho)$ and γ_D simultaneously, the expression $(\rho^3/\gamma_D - 3\rho + 3)$ must be considered with respect to the value of γ_D. No value of $\gamma_D < 9/4$ is physically viable, because $h \sim r^6$ in the limit $r \rightarrow$ inf. For any $\gamma_D \geq 9/4$ the ODE for $h(\rho)$ has at least one pole at $1 < \rho_{pole} < 3/2$ where $(\rho^3/\gamma_D - 3\rho + 3) = 0$. For $h(\rho)$ to be a physical relevant size distribution, $h(\rho \geq \rho_{pole}) = 0$ in this case. In LSW theory, the case $\gamma_D > 9/4$ is excluded in both treatments by declaring that $(\rho_{pole}^3/\gamma_D - 3\rho_{pole} + 3)$ and its derivative $(3\rho_{pole}^2/\gamma_D - 3)$ must both be zero. However, this is not quantitatively justified within LSW theory, as this declaration is derived "heuristically" by Wagner and "from inspection" of an equation by Lifshitz and Slyozov. In any case, the remaining possible value of $\gamma_D = 9/4$ is the one employed in LSW theory.

It was not until 1975 that Kahlweit provided the proper reasoning for accepting $\gamma_D = 9/4$ and excluding $\gamma_D > 9/4$.[56] Where LSW theory treats the asymptotic form of $f(R,t)$ for an open (i.e. infinite) system, Kahlweit presumes that the system is (more realistically) closed in a finite volume container. Thus, the final state of the system is a *single large spherical particle* that is in equilibrium with the solution. Kahlweit gives physical meaning to the quantity $(\rho^3/\gamma_D - 3\rho + 3)$ and notes that it is $d(\rho^3)/dt$, i.e. the rate of change of a single particle's dimensionless volume ρ^3 versus time, which includes both dR/dt and dR_c/dt. During Ostwald ripening, as the system evolves to a solitary large particle, Kahlweit infers that every particle in the system must achieve some maximum ρ at some point in their lifetime. At this maximum ρ, naturally the growth in ρ must be zero, i.e. $d(\rho^3)/dt = (\rho^3/\gamma_D - 3\rho + 3) = 0$ for that particle. This is the solution to $\rho = \rho_{pole}$ as defined above. Therefore, no particle grows larger than $\rho = \rho_{pole}$ in an experiment, which is equivalent to the declaration $h(\rho \geq \rho_{pole}) = 0$, corroborating the Wagner analysis. So far, the analysis matches that of Lifshitz and Slyozov, and Wagner reaches the same conclusion although through different logic. Finally, Kahlweit had the insight to examine the *fastest-growing particle* in the system. The fastest-growing particle reaches a maximum $\rho = \rho_{pole}$ at some point during Ostwald ripening, just as all the other particles do, but additionally the growth rate of this particle is maximized with respect to ρ, i.e. $d/d\rho\,[d(\rho^3)/dt] = 0$. Therefore, the solution to the two parameters γ_D and ρ_{pole} are given by the two equations $(\rho_{pole}^3/\gamma_D - 3\rho_{pole} + 3) = 0$ and $(3\rho_{pole}^2/\gamma_D - 3) = 0$. These equations are identical to those in the LSW derivation, and provides the LSW values $\gamma_D = 9/4$ and $\rho_{pole} = 3/2$. Kahlweit attaches physical meaning to the calculations by examining a closed system with a definable end-state.

The justified value $\gamma_D = 9/4$ allows the ODE for $h(\rho)$ to be decomposed as follows:

$$\frac{d\ln h}{d\rho} = \frac{\frac{8}{3}\rho^2 - 3}{(3+\rho)\left(\frac{3}{2}-\rho\right)^2} = -\frac{\frac{7}{3}}{(3+\rho)} - \frac{\frac{11}{3}}{\left(\frac{3}{2}-\rho\right)} + \frac{\frac{3}{2}}{\left(\frac{3}{2}-\rho\right)^2} \tag{3.17}$$

Therefore, with Wagner's declaration $h(0) = 1$ as a boundary condition, the solution to $h(\rho)$ is:

$$h(\rho) = \left(\frac{3}{\rho+3}\right)^{7/3}\left(\frac{\frac{3}{2}}{\frac{3}{2}-\rho}\right)^{11/3}\exp\left(-\frac{\rho}{\frac{3}{2}-\rho}\right) \tag{3.18}$$

Figure 3.3: The R_c-normalized solution to $f(R,t)$, the particle size distribution function, as solved by LSW theory both in the diffusion-limited case and the reaction-limited case. INSET: Time-wise evolution of the distribution. [54-56]

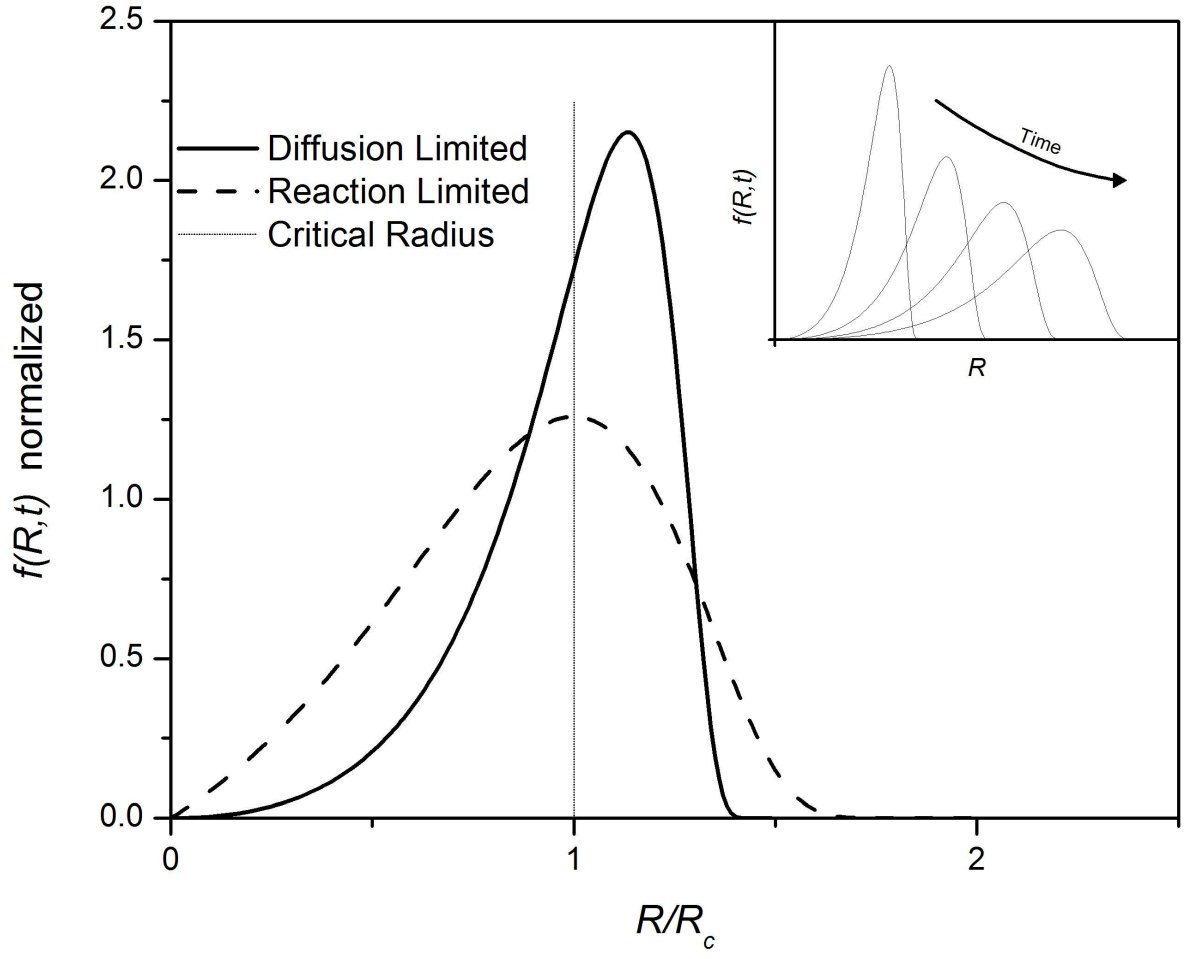

This provides a complete solution to the function *f(R,t)* in the asymptotic limit, requiring only an initial average size $\langle R \rangle_0$ and either the particle volume fraction φ or the initial particle concentration Z_0. The shape of the distribution $\rho^2 h(\rho)$ is shown in Figure 3.3. It is possible in principle, though difficult in practice, to verify this size distribution function and its time-wise evolution against particles observed to Ostwald ripen in experiments.

More importantly for experimental utility, however, was the determination of $\gamma_D = 9/4$. With this value, the growth of R_c and thus of $\langle R \rangle$ is quantitatively established, giving us the following growth law for Ostwald ripening:

$$\frac{d\langle R \rangle^3}{dt} = \frac{4}{9} K_D = \frac{8 \gamma v^2 c_\infty D}{9 kT} \tag{3.19}$$

The average growth rate incorporates the driving force (γ) and the primary resistance to transport ($c_\infty D$). If the diffusivity, solubility, and molar volume of the particle's monomers can be measured, then an Ostwald ripening experiment can provide a measure of the particle surface tension.

Wagner's derivation of the equivalent reaction-limited systems yielded similar results, with another size distribution function (also shown in Figure 3.3)

$$h_R(\rho) = \rho \left(\frac{2}{2-\rho} \right)^5 \exp\left(-\frac{3\rho}{2-\rho} \right) \tag{3.20}$$

and another growth law showing how the *square* of $\langle R \rangle$ grows proportionally with time, instead of the cube of $\langle R \rangle$ in diffusion-limited growth:

$$\frac{d\langle R \rangle^2}{dt} = \frac{64\gamma v^2 c_\infty k_s}{81kT} \tag{3.21}$$

In any given Ostwald ripening system, plots of $\langle R \rangle^2$ and $\langle R \rangle^3$ versus time should indicate if the particle growth is diffusion-limited, reaction-limited, or something in between. Plots of the % standard deviation should be invariant with time. No other form of Ostwald ripening is permitted by the LSW theory asymptotic analysis, and thus any systems of particles that shows growth outside these two cases is not undergoing classical Ostwald ripening.

3.5 RESULTS OF LSW THEORY

This behavior predicted by LSW theory has been witnessed in countless experimental systems, atomistic simulations, and phase-field calculations. The growth law, the size distribution function, and individual particle trajectories have been verified in several cases, and the theory is established as a quantitative theory of Ostwald ripening. Our own phase-field simulation of spinodal decomposition followed LSW theory quantitatively. (Results are not shown explicitly. Special thanks go to Prof. Long-qing Chen for assistance in optimizing the phase-field model, despite the fact that the data collected have yielded no novel results.)

Specific to this thesis, it has been observed that several nanocrystal systems undergo Ostwald ripening.[28, 38, 57] Within the accuracy of experimental measurements, such systems generally obey the quantitative relations of LSW theory. As a result, the single-particle growth rate Eq. (3.3) and the declaration of a constant polydispersity (for this solution to $h(\rho)$, the standard deviation appears to be about 21.4%) appears to accurately model the results of these nanocrystal systems.

3.6 DISCUSSION OF THE ASYMPTOTIC LIMIT

LSW theory analyzes the asymptotic limit in which the function $f(R,t)$ evolves in a completely self-perpetuating nature. The shape of $f(R,t)$ normalized about its average is completely unchanging in the asymptotic limit, because every slope and derivative in $f(R,t)$ preserves that shape when convolved with dR/dt. If at any time t the actual size distribution function $f(R,t)$ is different from the asymptotic LSW solution $g(t)\rho^2 h(\rho)$, then that difference $f(R,t) - g(t)\rho^2 h(\rho)$ will asymptotically shrink with time in an open (infinite) system. Kahlweit's analysis of the fastest-growing particle in a closed container refines this argument: $f(R,t) = g(t)\rho^2 h(\rho)$ is exactly accurate when the largest particle in the system is exactly of size $\rho = \rho_{pole}$. This increases the likelihood that an experimental system will obey LSW theory, since its conclusions are accurate at a finite time, achievable in an experimental timeframe. However, even this analysis depends critically on one assumption: that the Gibbs-Thomson effect can be approximated by its linear Taylor expansion.

It has been criticized that the linear Taylor expansion of the Gibbs-Thomson equation is an invalid approximation in nanocrystal systems.[39] The linearization presumes that the

nanocrystals are sufficiently large for $2\gamma w/RkT << 1$, and an order-of-magnitude analysis suggests $2\gamma w/RkT \sim 1$ or higher in many nanocrystal systems.[41] The overall error, however, is clearly bounded. The definition of R_c is the radius at which $dR/dt = 0$ and that definition remains the same in both the full exponential treatment and the linear approximation. Near that point, $R = R_c$ and $dR/dt = 0$, the linear and exponential versions of the growth law are identical to first order near $R/R_c = 1$. Meanwhile, examination of $h(\rho)$ show that the distribution emphasizes the population of particles near $R/R_c = 1$ and deemphasizes particles far away. As a result, even for moderate values of $2\gamma w/RkT$, LSW theory provides a good approximation to the actual dynamics even when it employs a poor approximation to the growth rate dR/dt.

It is necessary to note in addition that the asymptotic limit embodied in $h(\rho)$ does not exist unless the growth rate dR/dt varies faster than $1/R^2$. LSW theory employs the linear approximation to the exponential Gibbs-Thomson term. If the quadratic Taylor expansion were used for example and a $1/R^3$ term appeared in dR/dt, then the differential equation for $h(\rho)$ would contain the time-dependent quantity R_c. Thus, the separation-of-variables treatment is invalid if a linear approximation is not used. In any system with $2\gamma w/RkT \sim 1$, the nanocrystals would grow such that the distribution function would change shape over time. After a long time of continuous growth, eventually the system reaches the state $2\gamma w/RkT << 1$, and the assumptions of LSW theory are recovered. In the interim, the size distribution function $f(R,t)$ would slowly and asymptotically approach the LSW form $g(t)\rho^2 h(\rho)$ as $2\gamma w/RkT$ asymptotically approaches zero. It is with that procession in mind that LSW theory is used, if cautiously, to examine nanocrystals systems which are undergoing apparent Ostwald ripening.

3.7 SCALING-LAW BEHAVIOR FAR FROM THE ASYMPTOTIC LIMIT

The material balance in Eq. (3.9) clearly shows that if the average radius and critical radius are not initially equal, then they will converge with time. Using a scaling analysis, the time-scale of this convergence can be assessed.[111] Let the monomer concentration c_b at time $t = 0$ be much higher than the Gibbs-Thomson solubility of the average-sized particle, which is to say let $\langle R \rangle >> R_c$ at $t = 0$. The growth rate of all nanocrystals at $t = 0$ is therefore much higher than in the Ostwald ripening case. This faster growth will deplete the dissolved monomer, lowering c_b, which in turn reduces the growth rate, and so forth. As c_b decreases, more of the small nanocrystals begin to shrink, and eventually the total rate of monomers desorbing from shrinking nanocrystals is sufficient to provide (almost) all of the monomers condensing onto the growing nanocrystals. This last limit is the Ostwald ripening case described by LSW theory. The initial drop in c_b, however, will be analyzed here.

In the event that c_b is very high, the single-crystal growth rate Eq. (3.8a) is reduced to $dR/dt \approx vDc/R$ and the material balance Eq. (3.9) reduces to:

$$\frac{dc}{dt} \approx -4\pi cD\langle R \rangle Z \tag{3.22}$$

For the scaling argument, we integrate this equation assuming $\langle R \rangle$ changes slowly enough to be considered constant, yielding a decaying exponential for $c(t) = c_0 \exp(-k_{dep}t)$ where k_{dep} defines the rate of monomer depletion and $k_{dep} = 4\pi Z\langle R \rangle D$. The rate of Ostwald ripening as derived by LSW theory is

$$\langle R \rangle^3 = \langle R \rangle_0^3 + K_D t \tag{3.23}$$

We compare k_{dep} against K_D directly. The diffusion coefficient is equal. Experimental nanocrystal studies suggest Z is of the order of μM, and it is reasonable to assume c_∞ is at most of order μM for insoluble crystal material. If the surface tension is roughly $\gamma \sim 1$ J/m² (Nanda) and the molecular volume is $v \sim 0.01$ nm³ (for lattices with Å-size constants), then the quantity $2\gamma v/kT$ is on the order of 10 nm, which is equivalent to $\langle R \rangle$ for these systems. As a result, our scaling argument yields $K_D \sim v k_{dep}$ and the Ostwald ripening rate is the following order of magnitude:

$$\frac{\langle R \rangle^3}{\langle R \rangle_0^3} = 1 + \frac{v}{\langle R \rangle_0^3} k_{dep} t \tag{3.24}$$

Finally, we note that nanocrystals contain hundreds to thousands of monomers, especially when the average size is of order 10 nm, so the factor $v/\langle R \rangle_0^3 << 1$. Therefore, the timescale for growth by monomer depletion is many times faster than the timescale of Ostwald ripening. This analysis will be used in Chapter 4 when examining experimental data.

CHAPTER 4

DEVELOPING THE THEORY OF SIZE FOCUSING

4.1 THE SIZE FOCUSING OF NANOCRYSTALS

No analysis of nanocrystal synthesis would be complete without touching on the phenomenon of size focusing. Originally proposed by Tadao Sugimoto in 1987, a size focusing experiment would take nanocrystals (or any colloid) that are Ostwald ripening and then upon injection of additional precursors or reagents, the size distribution would become more monodisperse.[69]

The injection of new material effectively introduces more crystallizable solute (a.k.a. crystal monomers) into the solution. The monomer concentration c_b is driven up, which corresponds to driving R_c down in the single-particle growth rate, given in Chapter 3 in Eq. (3.8). In the diffusion-limited growth regime, the growth rate is proportional to D/R, and a particle of size $R = 4R_c$ ($\rho = 4$) is growing *slower* than a particle of size $R = 3R_c$ ($\rho = 3$), thus these two particles will become *closer in size* as time progresses. Generalizing this behavior to a population of nanocrystals, any size distribution that resides at sizes greater than $R = 2R_c$ will grow more monodisperse with time. Sugimoto noticed this behavior and defined all radii $R > 2R_c$ as the "narrowing zone" of particle growth, where any distribution would become narrower with time because dR/dt decreases with R. Conversely, the range of radii $0 < R < 2R_c$ was defined by Sugimoto as the "broadening zone" because dR/dt increases with R and particles that are farther from $R = R_c$ will grow faster away from $R = R_c$. These two zones are labeled in Figure 4.1 which graphs the single-particle growth rate dR/dt. Recall from Chapter 3 that the average size $\langle R \rangle$ is

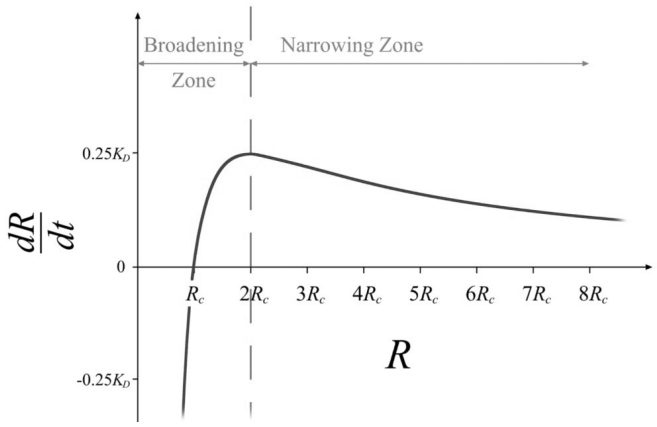

Figure 4.1: Growth rate for a single nanocrystal in a supersaturated monomer solution. The "broadening zone" and "narrowing zone" correspond to the regions $R < 2R_c$ and $R > 2R_c$, as per Sugimoto. [69]

equal to the critical radius R_c during Ostwald ripening. This places the entire population of nanocrystals in an Ostwald ripening system squarely in the broadening zone. Nominally, it is the injection of new material that drives R_c to low enough values that the distribution is shifted to the narrowing zone and size focusing is effected.

In the literature there are several notes that imply the size focusing phenomenon is due to an instantaneous, step-change increase in the monomer concentration as a result of the precursor reaction.[39, 41, 69] Under this assumption, the bulk solution would hold a "reserve of monomers" that would deposit onto the nanocrystals over time. In multiple nanocrystal syntheses, a single injection was observed to cause initial size focusing followed by Ostwald ripening. The transition from size focusing to Ostwald ripening is smooth, where the polydispersity of the nanocrystals decreases, reaches a minimum, and increases. The time scales of the focusing and ripening regimes in these studies are comparable, on the same order of magnitude or different by only a factor of 10. The "monomer reserve" mechanism has cited as the primary reason for the initial size focusing.[39, 41] However, the scaling law derivation conducted in Section 3.7 suggests that this behavior is not reasonably described by assuming an instantaneous "monomer reserve". The observed size focusing events occur much too slowly to

be caused by the depletion of monomers that had instantly appeared. Another mechanism is responsible for these behaviors.

Recently, a number of studies have probed the kinetics of precursor conversion to monomers in nanocrystal synthesis.[43, 53, 112-116] In these studies, precursors slowly convert to monomers as nanocrystals grow. This leads to a pseudo-steady state monomer concentration that is controlled by the kinetics of precursor conversion, rather than controlled by the solubility as in Ostwald ripening, and that can influence the narrowing of the size distribution. To quantitatively understand the relationship between monomer production rates and nanocrystal growth, we propose a theoretical model and show that "size focusing" might be extended throughout a synthesis if monomer production can be sustained at sufficient rates during growth,[43, 69, 102, 117] and even more efficiently if the nucleation and monomer production can be decoupled.

4.2 DERIVATION OF THE THEORY OF SIZE FOCUSING

We begin by using the same governing equations as employed by LSW theory (see Chapter 3) for the rate of diffusion-limited growth of a single nanocrystal of radius R:

$$\frac{dR}{dt} = \frac{vD}{R}\left((c_b - c_\infty) - \frac{2\gamma v c_\infty}{RkT} \right) = \frac{K_D}{R^2}\left(\frac{R}{R_c} - 1 \right) \tag{4.1}$$

The behavior embodied in Eq. (4.1) is plotted schematically in Figure 4.1 (adapted from Sugimoto's work). Here, $c_b(t)$ is the solution's monomer concentration at time t, c_∞ the monomer solubility, D the monomer diffusivity, v the crystal molar volume, and γ the crystal surface

tension. The second equality follows from the definitions that $K_D = \frac{2\gamma v^2 c_\infty D}{kT}$ and $R_c = \frac{2\gamma v}{kT}\frac{c_\infty}{c_b - c_\infty}$, as defined for LSW theory. A central quantity is the "critical" radius, R_c, defined as the radius at which $dR/dt|_{R=Rc} = 0$ just as in LSW theory. Crystals with $R > R_c$ will grow in a solution of monomer concentration c, while crystals that are smaller than R_c will shrink. The distribution evolves slowly, becoming increasingly polydisperse with time, and the standard deviation of sizes asymptotically approaches $\sigma = 0.215\langle R\rangle$ at long times and large sizes. Note that the maximum growth rate occurs at $R = 2R_c$. This divides the growth rate dR/dt into the "narrowing zone", $R > 2R_c$, and the "broadening zone", $R < 2R_c$, as per Sugimoto.

We augment the LSW derivation by including a production rate of new monomer in the bulk, in an instantaneous "monomer balance" in solution:

$$\frac{dc}{dt} = \dot{c} - \int_0^\infty \frac{d}{dt}\left(\frac{4\pi R^3}{3v}\right) f(R,t)\,dR = \dot{c} - Z\frac{d}{dt}\left(\frac{4\pi\langle R^3\rangle}{3v}\right) \tag{4.2}$$

$\dot{c}$ is the rate of new monomer production (in units of molar per second), $f(R,t)$ is the nanocrystal size distribution function at time t, and $Z = \int_0^\infty f(R,t)\,dR$ is the number concentration of nanocrystals (units of molar). We hypothesize that the growth process quickly becomes pseudo-steady, i.e. $dc/dt \approx 0$, both because the solubility of monomers in solution is likely to be incredibly low for crystalline materials and because dR/dt in Eq. (4.1) increases with c_b, implying an at-least exponential decay of c_b with time.[54] Integration of Eq. (4.1) over the whole distribution and a substitution of the result into Eq. (4.2) then yields

$$\frac{d}{dt}\frac{4\pi\left\langle R^3\right\rangle}{3} = 4\pi K_D\left(\frac{\langle R\rangle}{R_c} - 1\right) = \frac{v\dot{c}}{Z} \tag{4.3}$$

We highlight several salient features of Eq. (4.3). First, for $\dot{c} = 0$, this yields the LSW result $\langle R\rangle = R_c$ as stated in Eq. (3.12). Second, Eq. (4.3) expresses a simple mass balance, where all produced monomer goes directly to nanocrystal grwoth, which reflects our central pseudo-steady assumption where the dissolved monomer concentration does not change significantly. Third, and most importantly, large values of $\dot{c}$ result in $\langle R\rangle >> R_c$, and Ostwald ripening does not occur: in this "production-controlled" limit, Eq. (4.1) reduces to $dR/dt \propto K_D/R$. Therefore, (a) smaller crystals grow faster than larger ones, and the size distribution becomes more monodisperse as the average size increases, and (b) almost no nanocrystals are shrinking and the nanocrystal concentration Z is constant. Put another way, the entire disribution is taken out of the broadening zone and brought to the narrowing zone. The question is, what experimental conditions define whether "production-controlled" growth or Ostwald ripening will occur? To establish this transition, we introduce a dimensionless quantity ξ that we call the "size focusing coefficient," which is the ratio of the monomer production rate per particle to the Ostwald ripening rate:

$$\xi = \frac{v\dot{c}}{4\pi Z}\frac{1}{K_D} = \left(\frac{\langle R\rangle}{R_c} - 1\right) \tag{4.4}$$

We now consider the size distribution, *f(R,t)*, and how it narrows as $\langle R\rangle$ increases. *f(R,t)* obeys the continuity equation $\partial f/\partial t = \partial/\partial R\left[f\, dR/dt\right]$ in its temporal evolution. The LSW treatment provides

an analytical solution for *f* by assuming it has a time-independent shape *h(R)* where *f(R,t)* = *g(t)h(R),* and thus the solution is obtained by separation of variables.[54, 55] Since size focusing causes the distribution to become narrower with time, the constant-shape assumption is invalid here and it is not readily possible to derive a general solution to *f(R,t)* for $\dot{c} > 0$. Instead, we investigate only the evolution of σ, the standard deviation of nanocrystal sizes, through the use of an assumed distribution function, e.g. a time-dependent Gaussian.

Employing a Gaussian with average $\langle R \rangle$ and variance σ into the continuity equation yields a nonlinear differential equation whose exact solution is intractable. To gain insights into the behavior of the size distribution function, we employ a regular perturbation analysis in the region near $R = \langle R \rangle$. Therefore, we replace R with $\langle R \rangle(1 + \varepsilon)$ and examine only $\varepsilon << 1$, such that terms of higher order than ε are negligible. We thus obtain the following two equations corresponding to the ε^0 and ε^1 terms (see Appendix B for details):

$$-\frac{1}{\sigma}\frac{d\sigma}{dt} = \frac{K_D}{\langle R \rangle^3}(\xi - 1) \tag{4.5a}$$

$$\frac{d\langle R \rangle}{dt} = \frac{K_D}{\langle R \rangle^2}\left(\xi - \frac{2\sigma^2}{\langle R \rangle^2}(\xi + 1)\right) \tag{4.5b}$$

We see immediately from Eq. (4.5a) that σ decreases with time only for $\xi > 1$, in accordance with previous assertions. Therefore, for any $\xi > 1$ (i.e. $\langle R \rangle > 2R_c$ or at high monomer concentrations), some narrowing occurs, and $\sigma^2/\langle R \rangle^2$ eventually becomes negligible at long times.

In this case, Eq. (4.5b) reduces to Eq. (4.3). Combining Eqs. (4.5a) and (4.5b) at long times for $\xi > 1$ yields the following differential equation:

$$\frac{1}{\sigma}\frac{d\sigma}{dt} = \left(\frac{1}{\xi} - 1\right)\frac{1}{\langle R\rangle}\frac{d\langle R\rangle}{dt} \qquad (\forall \xi > 1) \tag{4.6}$$

For ξ constant or nearly so, we may integrate this equation from an arbitrary time t_0 where the average size and standard deviation are $\langle R\rangle_0$ and σ_0:

$$\frac{\sigma(t)}{\sigma_0} = \left(\frac{\langle R\rangle}{\langle R\rangle_0}\right)^{\frac{1}{\xi}-1} \tag{4.7}$$

This is our essential result: an equation that details the exact degree of size focusing expected given a monomer production rate embodied in ξ, the size focusing coefficient. This conclusion is in quantitative agreement with the scaling argument of Sugimoto that size focusing only occurs when $\langle R\rangle > 2R_c$ and the single-crystal growth rate decreases with size.[28, 69]

Note that LSW theory includes two treatments of Ostwald ripening, in which either diffusion or the surface adsorption reaction is the rate limiting step. The above derivation was performed for diffusion limited growth, and we note that we also performed the analogous derivation for surface-reaction controlled growth. In this case, the factor *D/R* in Eq. (4.1) is replaced with a reaction constant k_s. For $\dot{c}$ very high in this regime, however, *dR/dt* no longer has a decreasing

tail for large *R* and no narrowing can occur. Performing the equivalent Gaussian analysis for *f* under surface-reaction control, we find $\sigma \propto \langle R \rangle^{1/\xi}$ and no value of ξ causes σ to decrease with time. Therefore, size focusing is only possible at high $\dot{c}$ for diffusion-limited growth.

4.3 COMPARISON WITH NUMERICAL STUDIES

To substantiate the model's accuracy, Eqs. (4.3) and (4.7) have been compared against numerical simulations of nanocrystal growth based on Mantzaris' population balances.[41] We replicated the population balance method[41] to study an ensemble of nanocrystals growing while monomer was continually added to the solution throughout the simulation.

The single-particle growth rate (Eq. 4.1) is paired with a population-balance treatment of the distribution's evolution equation. The distribution is then numerically integrated over time; finite differences are used for spatial derivatives, time integration is approximated by the Runge-Kutta method, and all environmental variables are continually updated. For zero monomer generation, the results of the Mantzaris method approach LSW theory at long times regardless of the initial distribution.[41] For non-zero monomer generation, it was necessary to modify Mantzaris' material balance (Eq. 39 in the reference) to include the generated monomers in the balance:

$$S(\tau) = \frac{S_0}{\chi}\left[1 - Km_0(\tau)\int_0^{x_{\max}} x^{3/\lambda} u(x,\tau)dx\right] + \int_0^{\tau} \dot{C}(\tau)d\tau \qquad (4.8)$$

where $\dot{C}$ is dimensionless production rate, $\dot{C} = \dot{c}T_1/C_\infty$. In terms of Mantzaris variables and the new variable $\dot{C}$, the Damköhler number ξ can be expressed as follows:

$$\xi = \frac{RT}{2\gamma V_m^2 C_\infty D}\frac{V_m \dot{c}}{4\pi m_0(\tau)} = \frac{\dot{C}}{S_0}\frac{\langle y^3 \rangle_0 \chi}{3(1-\chi)} \tag{4.9}$$

The quantities $\langle y^3 \rangle$, S_0, and χ are necessary input parameters to the Mantzaris simulation, thus ξ is predefined for any choice of $\dot{C}(\tau)$. The results of a typical study using this method have been compared directly with our model in Figure 4.6. Points represent the data from the numerical integration, while the lines are the analytical equations of our model.

This study for ξ = 3.33 provides excellent agreement (< 0.3% overall RMSD) between numerical results and the analytical model. These results do not depend on the initial distribution's shape: simulations with Gaussian, bimodal, and skewed initial distributions all obeyed the model equally well under production-controlled conditions. Numerical integrations for other production-controlled system, with $\xi > 1$, achieve similar agreement. The numerical data diverge from our model for $\xi < 1$, as expected. (Numerical simulations indicate that for $0 < \xi < 1$, the distribution never reaches any pseudo-steady state similar to LSW theory or any quantifiable focusing state described by our model. This condition is unapproachable by either theory.) The polydispersity of all simulations with $\xi > 1$ decreased continuously until σ was small enough to approach the resolution Δx of the finite difference calculations. This comparison provides good evidence that the analytical derivation is mathematically robust, and that any system that obeys the dynamics of LSW theory is also capable of undergoing size focusing at high ξ. However, despite the model's mathematical accuracy, its relevance to experimental behaviors must be explored separately in the next section.

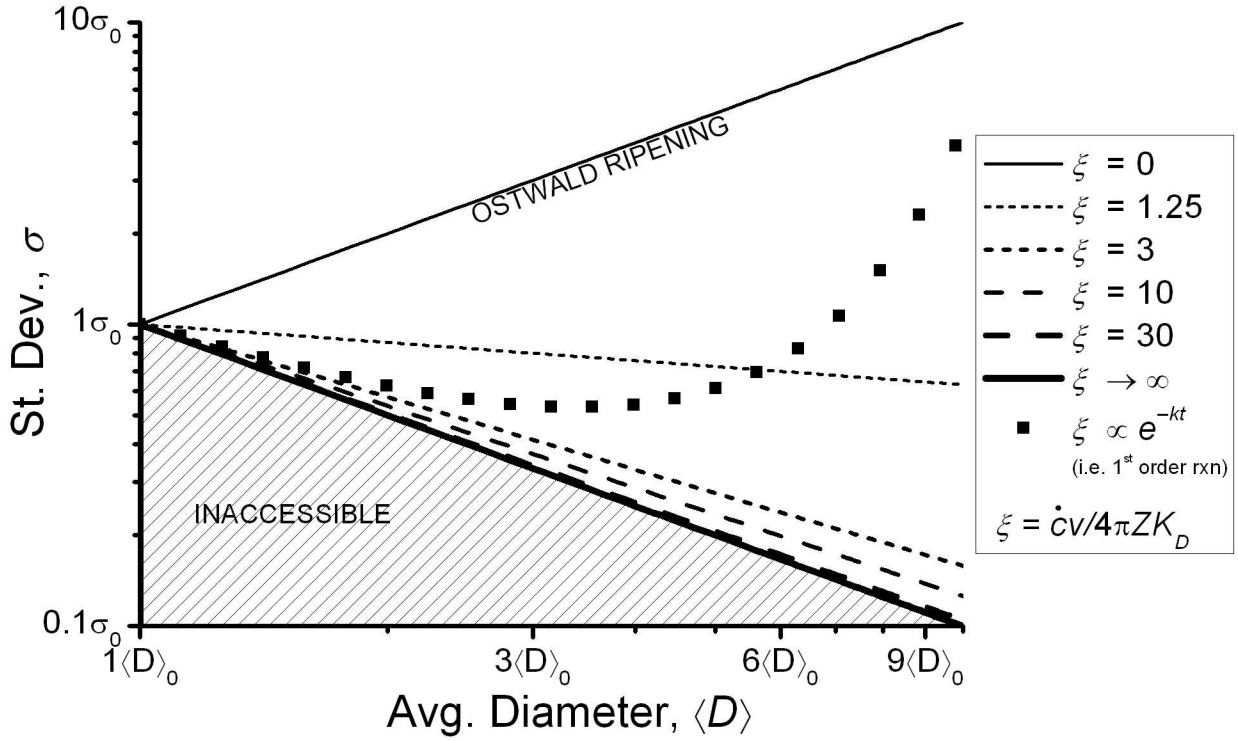

Figure 4.2: Parametric plot of the steady-state narrowing and broadening of nanocrystals. A nanocrystal mixture, initially with average diameter $\langle D\rangle_0$ and standard deviation σ_0, grows over time to $\langle D\rangle$ and σ with a monomer production rate $\dot{c}$ and size focusing coefficient ξ. $\xi = 0$ results in Ostwald ripening, while $\xi > 1$ causes size focusing. The lines show the degree of focusing for different magnitudes of ξ, approaching $\sigma \propto {}^{1}/_{\langle D\rangle}$ as $\xi \to \infty$. The points represent the size focusing/Ostwald ripening transition when monomer production is due to a 1st-order precursor reaction, thus $\xi(t) = \xi_0 \exp(-kt)$.

4.4 COMPARISON WITH EXPERIMENTS:

There is little systematic data that addresses the role of monomer production kinetics on the polydispersity of nanocrystal sizes. Furthermore, it is challenging to accurately measure nanocrystal concentrations, particularly at small sizes where the error in size measurement leads to large errors (perhaps 30% or more) in the measured nanocrystal volume.[53] This makes it difficult to obtain experimental proof of size distribution focusing for nanocrystals and hinders experimental validation of our theory. It also underscores the importance of establishing how production rates control size distributions.

For general insights, we can make predictions based on Eq. (4.7). Figure 4.2 plots the diameter-polydispersity relationship at various $\xi \propto \dot{c}$ and a fixed nanocrystal concentration (Z). These plots illustrate the power of controlling the monomer production. In the limit $\dot{c} \approx 0$, Ostwald ripening occurs and the % polydispersity remains constant near 21%, according to LSW theory.[54, 55] In the production-controlled limit, $\dot{c} \to \infty$, narrowing occurs to its maximum degree with $\sigma \propto 1/\langle R \rangle$ as the crystals grow. We conducted numerical simulations with various ξ values and found that $\xi = 10^2$–10^3 is essentially equivalent to the $\xi \to \infty$ limit. In this limit, if one begins with nanocrystals at 2.0±0.4nm (20% polydisperse), then the size distribution will evolve over time to 4.0±0.2nm (5% polydisperse), then 6.0±0.13nm (2%), and then 9.0±0.09nm (1%). While such highly monodisperse crystals have been produced in this manner with micrometer dimensions,[71, 118] our predictions show that monodisperse distributions can be created for nanocrystals smaller than 10 nm, as long as the focusing coefficient is large enough.

We now make a detailed comparison to some of the available experimental data, where narrowing has been observed and the kinetics of precursor conversion to monomer have been studied. In the size-focusing experiments published by Peng *et al.*[28] an injection of precursor to the solution during growth led to an immediate drop in polydispersity followed by a slow re-broadening of the distribution. To quantitatively model this data with our theory, we must have measures of the precursor reaction rate, the nanocrystal concentration Z, and the LSW constant K_D. As data for these quantities are unavailable, these are used as fitting parameters. Based on our previous observations,[53] the injection of $CdMe_2$ and TOPSe precursors leads to a monomer production that follows two competitive pathways: a rapid $CdMe_2$ thermolysis and a much slower acid-catalyzed TOPSe cleavage.[119] To fit the changes in size observed upon injection,

we used a single bimolecular rate law with first order kinetics, which effectively captures the reaction kinetics at early times. Our fit yielded k = 0.0490 $M^{-1}s^{-1}$, $K_D = 6.0\times10^{-4}$ nm^3/s, and nanocrystal concentrations after the first (Z_1 = 1.09×10^{-4} M) and second ($Z_2 = 3.83\times10^{-5}$ M) injections (see Figure 4.3).[120]

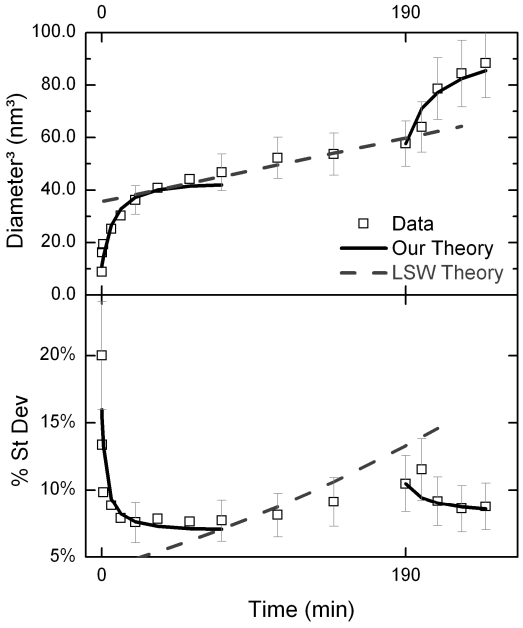

Figure 4.3: Comparing theory and data from Peng et al. [28] Top: Diameter data (squares). Bottom: % standard deviation data (diamonds). Solid lines represent our model in equations (4.3) and (4.7), dashed lines represent Ostwald ripening by LSW theory.

For further validation, we employed Peng's assumption that Ostwald ripening occurs between injections, roughly t = 75-190 min, as evidenced by the broadening distribution. If this is the case, the diameter should obey the LSW growth law, $\langle R\rangle^3 - \langle R\rangle_0^3 = {}^4/_9 K_D t$, and the polydispersity should follow Wagner's equation VI.9:[55]

$$\%\sigma = (\%\sigma)_0 \exp\left(\frac{K_D t}{\langle R\rangle^3}\right) \tag{4.10}$$

These two expressions are plotted as dashed lines in Figure 4.3, using the value of K_D extracted from our fit. The results are in good agreement with the observed changes in diameter and polydispersity,[121] reinforcing the value of K_D extracted from this data.

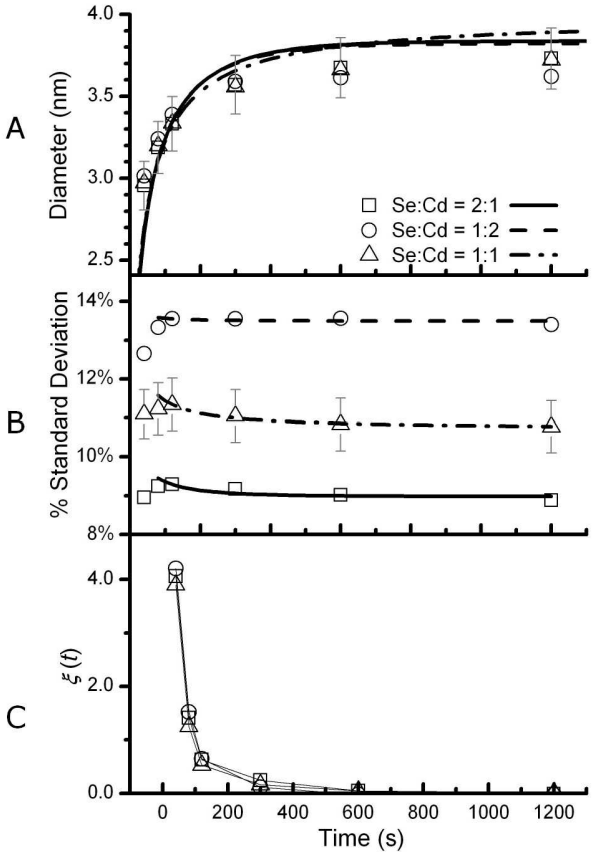

Figure 4.4: Comparing theory and data from Chan et al. [43] Experimental data (points) and our model (lines) for three reactions, with initial precursor concentrations [Se]0/[Cd]0 = 74.2/37.1 mM, 38.4/77.0 mM, and 74.2/74.2 mM.
(a) Diameters measured by UV-Vis vs. Eq. (4.3)
(b) % standard deviation from UV-Vis vs. Eq. (4.7)
(c) Size focusing coefficient ξ calculated from [CdSe] data and Z data with interpolating lines.

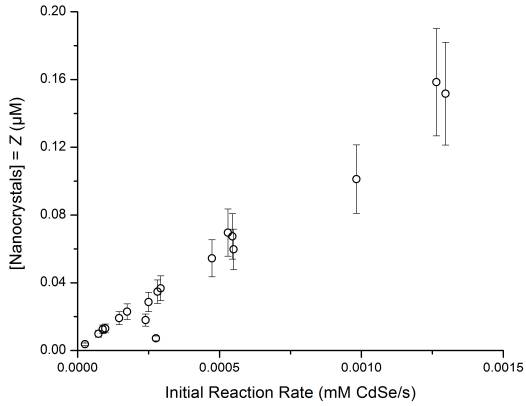

Figure 4.5: Plot of the nanocrystal concentration Z from all reactions by Chan et al. [43] versus the initial CdSe molar generation rate, $\dot{c}_0 = k_O[\mathrm{Cd}]_0[\mathrm{Se}]_0$. The trend is clearly linear with a zero y-intercept, as predictedby Sugimoto. [123]

We next turn to a second study of CdSe nanocrystal syntheses by Chan *et al* where eighteen independent CdSe syntheses were conducted with various precursor concentrations by a robot designed for the automation of chemical syntheses.[43] In this study, the concentration of CdSe crystal units was measured directly via UV-Vis absorption. With this data, we may develop an accurate expression for $\dot{c}$ from [CdSe] instead of assuming a chemical mechanism.[122] We find that a bimolecular rate expression (k_P·[CdOLA]·[TOPSe]) provides a more than adequate representation of the kinetic data, with RMSD = 6.7%. Figure 4.4 plots the experimental data and our model for three representative reactions. $K_D = 9.6\pm2.3\times10^{-3}$ nm³/s was fit as a single constant that spans all syntheses that underwent narrowing. Additionally, the variation of the fit parameter Z against the initial reaction rate (Figure 4.5) is consistent with Sugimoto's

theory of nucleation,[123] in which Z varies linearly with the initial monomer supply rate, $\dot{c}_0$, during nucleation. This lends self-consistency to the assumed kinetics and fit values. We note, however, that because Z varied so closely with $\dot{c}_0$ across the various reactions, the parameter ξ did not change significantly between syntheses, as shown in Figure 4.4(c). The observed decrease in ξ across all three syntheses arises from the decreasing reaction rate, which is analogous to the first-order reaction kinetics ($\xi \propto e^{-k_P t}$) plotted in Figure 4.2. This pattern is discussed in more detail below.

4.5 DISCUSSION OF PRODUCTION-CONTROLLED GROWTH

An interesting aspect of our theory is that the extent of focusing (ξ) depends on both the monomer production rate ($\dot{c}$) as well as the number of nanocrystals (Z). Although a lack of systematic data makes it difficult to unequivocally verify our prediction, the studies by Chan and Peng are qualitatively consistent with the relationship between $\dot{c}$, Z and the focusing coefficient. In the study by Chan et al. $\dot{c}_0$ and Z are proportional to one another across the range tested, as shown in Figure 4.5 comparing the initial rate of CdSe production with the final (most accurate) measurement of Z. It is for this reason that no significant differences in the focusing coefficient are observed (Figure 4.4(c)). On the otherhand, in the study by Peng et al. the second injection of precursors does lead to increased focusing because Z is already fixed at this point in the reaction (i.e. no new nanocrystals are formed) and ξ increases with the increase in $\dot{c}$.

A number of studies have shown a relationship between the monomer production rate and the number of nuclei. Theoretical predictions published by Sugimoto show that Z can be proportional to the rate of monomer production during homogeneous nucleation ($\dot{c}_0$)[123] A

number of experimental studies have provided evidence supporting this correlation, both in the synthesis of micron sized silver halide crystals and in the synthesis of semiconductor nanocrystals.[53, 70, 71, 123] As a consequence of this relationship, when a single injection of precursors causes homogeneous nucleation and growth, increasing $\dot{c}$ will not effect changes in the initial ξ value ($\xi_0 \propto \dot{c}_0/Z \approx$ constant). Furthermore, because $\dot{c}(t)$ depends on the precursor concentrations, the function $\dot{c}/\dot{c}_0$ is identical for any initial precursor concentrations. Therefore, even large changes to the precursor concentrations will have little impact on the extent of narrowing, unleas they influence K_D. On the other hand, by controlling the nucleation and growth processes independently, one can influence the narrowing of the size distribution during a nanocrystal synthesis.

Seeded growth is one such strategy where nuclei are supplied from an external source, the number concentration of which can be varied over a large range, independent of $\dot{c}$. These conditions are effectively obtained in the study by Peng et al., where the second precursor injection does not effect nucleation; thus Z is established prior to the second injection and the new ξ may be adjusted through the volume of the injection. Likewise, under conditions where nanocrystal precursors are mixed at room temperature and slowly heated, nucleation occurs at a lower temperature than growth, potentially leading to higher pseudo-steady state supersaturation.[124]

4.6 THE BROADENING ZONE DURING PRODUCTION-CONTROLLED GROWTH

Two important qualitative assumptions are made in developing the theory of size focusing. The first is that the quantity of dissolving nanocrystals becomes negligible quickly and may be

disregarded. The second is that the number concentration of nanocrystals, *Z*, is approximately constant and its time-dependent behavior may be neglected in all calculations. A quantitative analysis of the shrinking nanocrystals will confirm these two assumptions.

To investigate the shrinking nanocrystals, it is convenient to consider the total distribution *f* as a sum of two distributions: the broadening-zone distribution, f_b, and the narrowing distribution, f_n. As shown in Figure 4.1, these two zones are defined around the boundary $R = 2R_c$. R_c increases as *c* decreases with time, therefore the domains of f_b and f_n are always changing with time. By combining Eq. (4.3) and Eq. (4.4) for production-controlled growth, the temporal evolution of R_c is determined:

$$\frac{dR_c^{\,3}}{dt} = \frac{1}{(\xi+1)^3}\frac{d\langle R\rangle^3}{dt} = \frac{3\xi K_D}{(\xi+1)^3} \tag{4.11}$$

The behavior of the nanocrystals at the boundary $R = 2R_c$ is easily determined. For any $\xi > 0$, dR/dt at $R = 2R_c$ is larger than dR_c/dt given by Eq. (4.11). Therefore, nanocrystals will always grow from the broadening zone into the narrowing zone, transferring material from f_b into f_n. Additionally, small nanocrystals continue to shrink away until they dissolve into monomers. In this way, f_b has two material sinks at its extremes, $R = 0$ and $R = 2R_c$. Qualitatively it is observed therefore that the population of f_b falls away quickly to a negligible value, justifying the approximations made above, but without any quantitative validation.

Here, the exact evolution of f_b is explored, from which a model for dZ/dt and for the fraction of broadening nanocrystals may be built. The domain of f_b is limited and f_b and f_n do not overlap at

any R, thus the evolution equation can be used exclusively to examine f_b independently of f_n when it is defined on the interval $0 \le R < 2R_c$:

$$\frac{\partial f_b}{\partial t} = -\frac{\partial}{\partial R} f_b \frac{dR}{dt} \qquad R \in [0,2R_c) \tag{4.12}$$

The evolution of f_b results from the growth rate, dR/dt, which banishes material from its center $R = R_c$. Furthermore, the magnitude of dR/dt increases further away from $R = R_c$. No nanocrystals are generated in f_b (nucleation is still presumed negligible) and we have established that nanocrystals leave f_b at both extremes. This effectively to leads to $R = R_c$ acting as the "source" of nanocrystals that evolve toward the two "sinks" at $R = 0$ and $R = 2R_c$. This is only possible for f_b a continuous, positive function if its shape is static about $R = 2R_c$ and self-perpetuating, the exact behavior of the LSW distribution for an Ostwald ripening system.

Because f_b must be a static-shape function, it is amenable to separation-of-variables and to an all-analytic derivation which mirrors the LSW derivation. Let $\rho = R/R_c$ and let $f_b(R,t)$ be defined:

$$f_b(R,t) = g_b(t)\rho^2 h_b(\rho) \tag{4.13}$$

With this framework, the evolution equation given for LSW theory by Eq. (3.10) is combined with Eq. (4.13) to yield the following multi-variable differential equation:

$$\rho^2 h_b(\rho)\frac{R_c^{\ 3}}{K_D}\frac{1}{g_b(t)}\frac{dg_b}{dt} = -\left[\frac{dh_b}{d\rho}(\rho-1)+h-\left(\rho^3\frac{dh_b}{d\rho}+2\rho^2 h_b(\rho)\right)\frac{1}{3K_D}\frac{dR_c^{\ 3}}{dt}\right] \qquad (4.14)$$

The solution requires the declaration of two new parameters. The first is $\phi_b(t)$, the volume-fraction of nanocrystals contained in the broadening zone:

$$\phi_b(t) = \int_0^{2R_c}\frac{4\pi R^3}{3} f_b(R,t)dR = \frac{4\pi R_c(t)g_b(t)}{3}\int_0^2 \rho^5 h_b(\rho)d\rho \qquad (4.15)$$

This quantity is time-dependent and its temporal behavior is one of the critical results of this analysis. The second new quantity is $Z_b = \int_0^{2R_c} f_b(R,t)dR$, the number concentration of nanocrystals that reside in the broadening zone. Z_b/Z represents the fraction by number of broadening nanocrystals and ϕ_b/ϕ represents the fraction by volume of broadening crystals. The detailed mathematical derivation continues in Appendix C, but the salient points are reproduced and discussed here.

In the derivation of $h_b(\rho)$, the following dimensionless quantity $\Gamma(\xi)$ repeatedly appears, which varies only with the size-focusing coefficient ξ. This quantity has four definitions:

$$\begin{aligned}\Gamma(\xi) &= -\frac{h_b(2)}{\int_0^2\rho^2 h_b(\rho)d\rho}\frac{8}{3K_D}\frac{dR_c^3}{dt}+\frac{h_b(2)+h_b(0)}{\int_0^2\rho^2 h_b(\rho)d\rho} = -\frac{R_c^3}{K_D}\frac{1}{Z_b}\frac{dZ_b}{dt}\\ &= \frac{1}{K_D}\frac{dR_c^3}{dt}-\frac{R_c^3}{K_D}\frac{1}{\phi_b}\frac{d\phi_b}{dt} = -\frac{1}{3K_D}\frac{dR_c^3}{dt}-\frac{R_c^3}{K_D}\frac{1}{g_b}\frac{dg_b}{dt}\end{aligned} \qquad (4.16)$$

The most convenient definition is the second one, relating $\Gamma(\xi)$ explicitly to the rate of change of Z_b vs. the Ostwald ripening rate. This function $\Gamma(\xi)$ is invariant with either time or ρ, thus it may be used in Eq. (4.14) to simplify the result and obtain an ordinary differential equation for h_b.

$$\left[-\frac{3\xi}{(\xi+1)^3}\rho^2-\Gamma(\xi)\rho^2+1\right]h(\rho)+\left(\rho-1-\rho^3\frac{\xi}{(\xi+1)^3}\right)\frac{dh}{d\rho}=0 \tag{4.17}$$

In the original LSW derivation, it was determined that the denominator of $h(\rho)$ had a poles at some value of ρ which affected the form of $h(\rho)$. Such is also the case here. The prefactor of the right-hand term in Eq. (4.17), $\rho - 1 - \rho^3 \cdot \xi/(\xi + 1)^3$, has three zeros corresponding to three values of ρ for any $\xi > ½$; one value is negative, another value is $\langle\rho\rangle = \xi + 1$ (corresponding to Eq. 4.4 above), and the third lies in the region $1 < \rho_{pole} < 3/2$. The first two poles are immaterial here, but for the last pole $h_b(\rho)$ diverges at $\rho = \rho_{pole}$ if the value of $\Gamma(\xi)$ is left arbitrary. To ensure $h_b(\rho)$ remains finite and positive everywhere in $0 < \rho < 2$, we apply an *ansatz* that the left-hand term in Eq. (4.17), namely $[3\xi/(\xi + 1)^3 - \Gamma(\xi)]\rho^2 + 1$, is *also* equal to zero at $\rho = \rho_{pole}$. Analysis by L'Hôspital's rule proves that this *ansatz* guarantees $h_b(\rho)$ is positive and finite everywhere.

Our *ansatz* also yields this definition of $\Gamma(\xi)$

$$\Gamma(\xi)=\frac{1}{\rho_{pole}^2}-\frac{3\xi}{(\xi+1)^3} \tag{4.18}$$

as well as a convenient restatement of Eq. (4.17):

$$\frac{\frac{\rho^2}{\rho_{pole}^2}-1}{\rho-1-\rho^3\frac{\rho_{pole}-1}{\rho_{pole}^3}}=\frac{d\ln h_b}{d\rho} \tag{4.19}$$

This equation can be integrated exactly to yield a solution to $h_b(\rho)$ of the following form:

$$h_b(\rho)=C_h\left(1-\left(\frac{\rho}{\rho_{pole}}+\frac{\rho^2}{\rho_{pole}^2}\right)(\rho_z-1)\right)^{-\frac{\rho_{pole}}{2(\rho_{pole}-1)}}\left(\frac{1+\left(1+2\frac{\rho}{\rho_{pole}}\right)\sqrt{\frac{\rho_{pole}-1}{\rho_{pole}+3}}}{1-\left(1+2\frac{\rho}{\rho_{pole}}\right)\sqrt{\frac{\rho_{pole}-1}{\rho_{pole}+3}}}\right)^{\frac{1}{2}\frac{\rho_{pole}}{\sqrt{(\rho_{pole}+3)(\rho_{pole}-1)}}} \tag{4.20}$$

In the limit $\xi\to\infty$, a Taylor expansion on $1/\xi$ yields the following approximate form:

$$\lim_{\xi\to\infty}h_b(\rho)=C_h\exp\left(\frac{\rho}{2}\left(1+\frac{\rho}{\rho_{pole}}\right)+\left(1+2\frac{\rho}{\rho_{pole}}\right)\frac{1}{\rho_{pole}+3}\right) \tag{4.21}$$

While this form is only accurate for $\xi > 20$, it unequivocally illustrates how $h_b(\rho)$ grows monotonically and more-than-exponentially from $\rho = 0$ to $\rho = 2$. The value of C_h is completely arbitrary. To confirm the solution is correct, however, it must be validated against our *ansatz* as given by Eq. (4.18). For a given ξ, ρ_{pole} and $h_b(\rho)$ are calculated, then $\Gamma(\xi)$ is determined from the first definition of Eq. (4.16). This is compared directly against Eq. (4.18) for the given value of ξ in Figure 4.6, showing that the values are identical, proving that this derivation of $h_b(\rho)$ is completely self-consistent.

4.7 OTHER PARAMETERS vs. TIME

The solution to $f_b(R,t)$ has little utility by itself. However, the derivation and solution of the function $h_b(\rho)$ permitted the definition of $\Gamma(\xi)$ and ρ_{pole}, from which other quantities in the system may be evaluated. For example, the third definition of $\Gamma(\xi)$ given in Eq. (4.16) yields the following differential equation for $\phi_b(t)$:

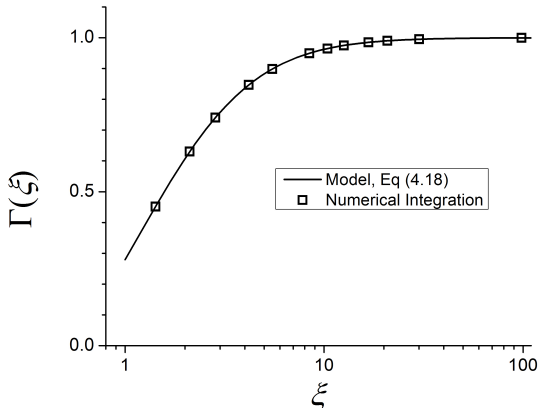

Figure 4.6: Comparison of two calculations of $\Gamma(\xi)$, one from Eq. (4.18) and one from numerical integration of $\rho^2 h_b(\rho)$. The negligible error is attributed to numerical integration.

$$\frac{1}{\phi_b}\frac{d\phi_b}{dt} = \left[2 - \frac{1}{\rho_z^{\,2}}\frac{(\xi+1)^3}{3\xi}\right]\frac{1}{R_c^{\,3}}\frac{dR_c^{\,3}}{dt} \tag{4.22}$$

This equation is now easily solvable as a power law, $\phi_b \propto R_c^{\,n} \equiv \langle R\rangle^n$, with a constant exponent. The fraction of nanocrystals in the broadening zone can be expressed by ϕ_b/ϕ, where ϕ is the total nanocrystal volume fraction (see Appendix A). If Z is nearly constant and the distribution is monodisperse (as already presumed in this analysis), then ϕ goes as $\langle R\rangle^3$. The result is that the fraction of nanocrystals in the broadening zone evaluates to the following power law:

$$\frac{\phi_b}{\phi} = \frac{\phi_{b0}}{\phi_0}\left(\frac{\langle R\rangle^3}{\langle R\rangle_0^{\,3}}\right)^{1-\frac{1}{3}\frac{\rho_{pole}}{\rho_{pole}-1}} \tag{4.23}$$

For any value of $\xi > ½$ and thus $\rho_{pole} < 3/2$, Eq. (4.23) states that the fraction of nanocrystals in the broadening zone decreases with time. For any $\xi > 1$ that fraction decreases faster than $\langle R\rangle^{-2}$, for $\xi > 2$ it decreases faster than $\langle R\rangle^{-8}$, and for $\xi > 10$ it decreases faster than $\langle R\rangle^{-\xi^2}$. In any regime that might be considered "production-controlled growth", ϕ_b decreases to nearly zero before the average radius has doubled. This proves quantitatively that the assumption of negligible shrinking nanocrystals is correct.

The solution to $f_b(R,t)$ via $h_b(\rho)$ also provides us with a quantitative rate of dissolution of nanocrystals, computed as dZ/dt. Note that this quantity is different from dZ_b/dt and requires a different calculation than the one given in Eq. (4.16). Specifically, dZ/dt is calculated through Eq. (3.13) from Chapter 3. The result is combined with Eq. (4.23) to obtain the following:

$$\Delta Z = Z_0 - Z = \frac{h_b(0)}{\int_0^2 \rho^2 h_b d\rho} \frac{1}{\Gamma(\xi)} \left[1 - \left(\frac{\langle R \rangle}{\langle R \rangle_0} \right)^{2 - \frac{1}{\rho_{pole} - 1}} \right] \tag{4.24}$$

The prefactor in front has been simplified algebraically, with the result that its maximum value is e^{-4}, occurring at $\xi \to \infty$. Meanwhile, the exponent $2 - 1/(\rho_{pole} - 1)$ is always negative, thus the term in []-brackets is always positive and less than 1. The total result is that the total change in the nanocrystal concentration, ΔZ, cannot exceed 2% of Z_0 whenever the broadening zone is accurately described by $\rho^2 h_b(\rho)$. This decrease is much smaller than experimental measurement error for Z (30%) and also much smaller than scattered experimental observations of a decrease in Z.[43, 53, 125] Eq. (4.24) implies that any experimentally observed changes in Z are due to

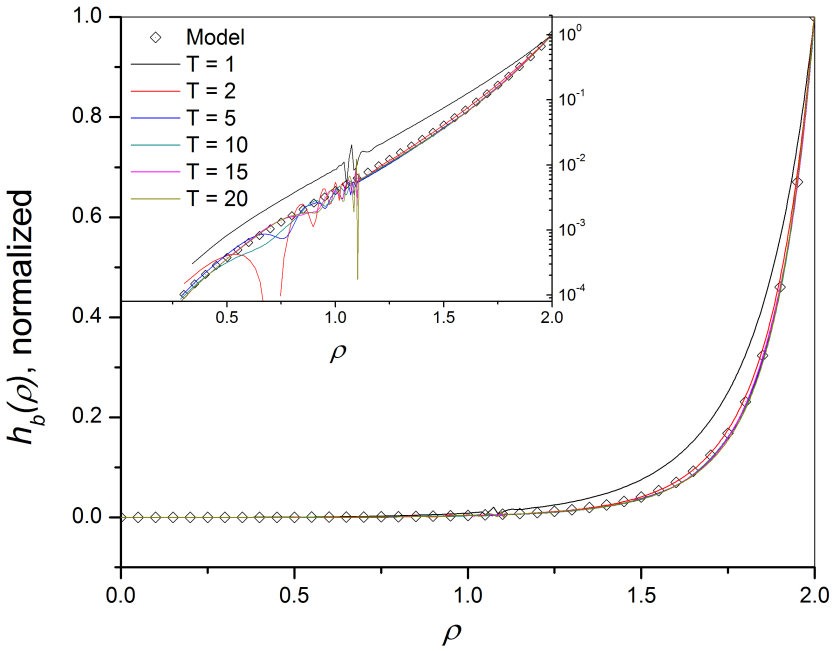

Figure 4.7: Comparison of the broadening zone size distribution function, numerical vs. analytical. Data from a Mantzaris population balances simulation [41] are represented as lines. Different colors represent different simulation times, *T*. Our model Eq. (4.20) is represented as diamonds. *T*=1 is the outlier, with all other data collapsing to our model equation. The inset shows a logarithmic plot, which highlights the numerical instabilities that result from the finite-difference scheme.

post-nucleation behaviors where the actual size distribution function is still far away from $\rho^2 h_b(\rho)$.

4.8 NUMERICAL ANALYSIS OF THE BROADENING ZONE MODEL

Using population balance simulations,[41] we took the same simulations which were previously compared to Eq. (4.7) and investigated the distribution between $\rho = 0$ and $\rho = 2$. Figure 4.7 compares $f_b(R,t)$ from the simulation data at various times (shown as lines) against our model (shown as points) $\rho^2 h_b(\rho)$ as calculated from Eq. (4.20). After dimensionless time $T = 2$, the broadening-zone distribution has attained a constant shape which our model accurately represents.

Additionally, the volume fraction ϕ_b appears to obey the power law given in Eq. (4.24), as shown in Figure 4.8. In this simulation, $\xi = {}^5/_3$ and $\rho_{pole} \approx 1.125$, thus ϕ_b should vary as $R_c^{-2.99}$. A power-law fit to the data yields a slope of –3.07, within 2.7% of the theoretical value. The error is

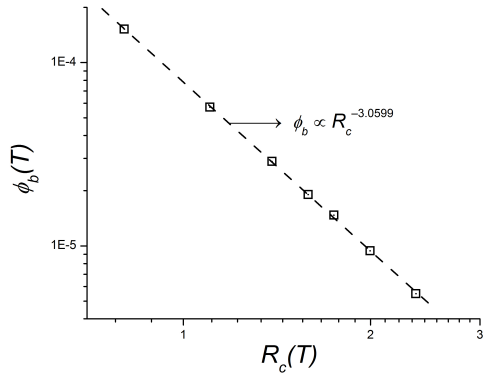

Figure 4.8: Simulation values of ϕ_b, the volume fraction of nanocrystals in the broadening zone, versus R_c, the critical radius. at various times during production-controlled growth. The squares are data.; the line is a power-law fit.

attributed to propagation of errors in the algorithm, which are emphasized in the broadening zone as a result of the algorithm's structure.[41] Additionally, Z decreased by a total 0.012% from $T = 0$ to $T = 1$ and showed no changes through $T = 100$ when the simulation ended.

As stated above, some experimental studies witnessed a measurable decrease in Z concurrent with size focusing, $d\sigma/dt < 0$.[37] To investigate whether such a condition could be reproduced, we conducted 140 Mantzaris-type simulations with multiple input parameters. Only four simulations showed the given behavior of Z decreasing simultaneously with size-focusing. In those four cases, however, the calculations revealed that $\langle R \rangle / R_c < \xi + 1$, which by Eq. (4.2) and Eq. (4.4) implies c_b was *increasing* with time. The LaMer model of nucleation and growth suggests this is not possible after nucleation. It is likely that these 4 simulations were run with inappropriate choices of initial conditions. Such a failure to reproduce experimental trends in simulation is inconclusive, however. Our analysis only proves that such a trend is impossible at long times after nucleation.

4.8 CONCLUSION

We have developed a theory of size distribution focusing of nanocrystals that includes a rate at which monomers are produced in the reaction medium over time. Using our model we show how size distributions of nanocrystals can narrow or broaden depending on the rate of the monomer

production and the number of nanocrystals. Quantitative examination of the entire size distribution confirmed all the assumptions made, and provided specific insight into the dissolution rate of nanocrystals during size focusing. We further suggest that seeded nanocrystal growth reactions are likely to give rise to synthetic methods where size focusing can be best controlled. Under these conditions the number of nanocrystals and the monomer production rate can be independently tuned to optimize size focusing and permit the *a priori* design of procedures that produce nanocrystals of a desired size and polydispersity.

CHAPTER 5

THE GROWTH OF SURFACTANT-COATED NANOCRYSTALS

5.1 NANOCRYSTALS COATED WITH SURFACTANT

Many modern nanocrystal syntheses produce nanocrystals that are coated with surfactant molecules. Cadmium selenide, iron oxide, cobalt, gold, silver, and zinc oxide are just a few examples of nanocrystals often manufactured with surfactants grafted to their surface.[10, 47-49, 126] Although this trend started in the early 1990s to make the nanocrystals easier to synthesize and more stable in solution, many studies in the last decade have used surfactants with specific tail groups to functionalize the nanocrystal for particular applications.[73, 98] In fact, the use of surfactants is so ubiquitous that the development of "surfactant free" syntheses of nanomaterials has jumped significantly since 2008.

Experimental evidence suggests that some surfactant-mediated nanocrystals grow similarly to bare nanocrystals.[36, 38] Also, many works have assessed the effect that a surfactant has on a nanocrystal's optical properties.[64-66] To date, however, no theoretical description of the growth processes for surfactant-coated nanocrystals exists and LSW theory has been used as an approximation. It unknown what differences between bare and surfactant-mediated nanocrystals an experimenter might observe or what errors might be made by assuming their behavior is identical. Particularly in the size-focusing case (Chapter 4), the surfactants might affect growth in a critical way such that our theory of size focusing is no longer accurate. To investigate these differences thoroughly, it is necessary to re-examine Ostwald ripening and size focusing

quantitatively to obtain a comprehensive theoretical picture of how surfactants affect spherical nanocrystal growth.

First, a new single-particle growth rate is derived which incorporates diffusion through the surfactant layer into its framework. Second, the new single-particle growth rate is used to modify the LSW theory of Ostwald ripening. Almost all mathematical steps are nearly identical to Wagner's original derivation and the new results require few additional assumptions.[55] Third, the theory of size focusing is reproduced with the new single-particle growth rate. Although our results will show that Ostwald ripening is negligibly affected by the addition of a surfactant layer, the analysis of size focusing will indicate that surfactants can be very useful in tuning the size focusing process.

5.2 THE GROWTH RATE OF A SINGLE SURFACTANT-COATED PARTICLE

The initial form of the growth rate used here is identical to the initial form of the LSW bare-particle growth rate. Adsorption is assumed to proceed as a first-order reaction between the particle surface and the monomers present in solution at the surface, and the rate of desorption is presumed to be governed by the Gibbs-Thomson equation:

$$\frac{dR}{dt} = vk_s\left(c_i - c_{sat}e^{2\gamma/RkT}\right) \tag{5.1}$$

As stated in Chapter 3, c_i is the concentration of monomers in solution at the particle surface. Note that the Gibbs-Thomson term includes c_{sat} instead of c_∞. c_{sat} is the monomer solubility within the surfactant layer, which is presumably different from the solubility c_∞ in the solvent.

The concentration at the particle surface c_i must be calculated from the mass transfer to and from the particle surface, which includes the adsorption/desorption reactions and the diffusion of monomer to/from the bulk solution. The classical LSW treatment assumes diffusion is uniform between the surface and the bulk, and the pseudo-steady state diffusion equation is solved with boundary conditions given by the bulk concentration c_b and the monomer flux at the particle surface.[54-56] This analysis will be augmented to quantitatively include the presence of surfactants bound to the nanocrystal surface.

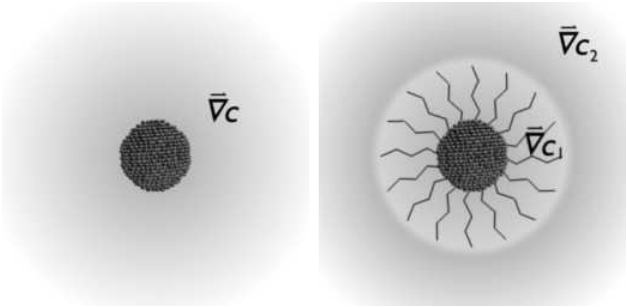

Figure 5.1: Illustration of the diffusion layer around a bare nanocrystal (left) and the double-diffusion layer induced by the addition of a surfactant layer (right). The two concentration gradients act as diffusive resistances to monomer transport.

Let the space filled by grafted surfactants be denoted by a layer of thickness δ around the R-sized spherical particle. At the point $R + \delta$, the surfactant layer interfaces with the bulk solution. We make the approximation that interface between the solution and the surfactant layer is sharp. The concentration profile therefore experiences a zero-order discontinuity at a distance $R + \delta$ from the particle center. The discontinuity exists because the monomers (a) may diffuse faster or slower in the surfactant layer than in the bulk layer and (b) may be more or less soluble in the surfactant layer than the bulk layer. Therefore, each space has its own independent concentration profile which must be solved together. This model's geometry is illustrated in Figure 5.1. Let the spherically-symmetric concentration profiles be denoted by $c_1(r)$ in the bulk and by $c_0(r)$ within the surfactant layer. Each of these profiles is governed by pseudo-steady diffusion of monomers (where the particle surface is assumed to move much slower than monomer diffusion). The diffusion-only mass balance yields the following two differential equations:

$$\nabla^2 c_0 = \frac{1}{r^2}\frac{\partial}{\partial c} r^2 \frac{\partial c_0}{\partial r} = 0 \tag{5.2a}$$

$$\nabla^2 c_1 = \frac{1}{r^2}\frac{\partial}{\partial c} r^2 \frac{\partial c_1}{\partial r} = 0 \tag{5.2b}$$

with solutions:

$$c_0 = a_0 + \frac{b_0}{r} \tag{5.3a}$$

$$c_1 = a_1 + \frac{b_1}{r} \tag{5.3b}$$

To solve for the constants of integration, we use four boundary conditions. The first and second boundary conditions are the same as that for the LSW growth rate: the concentration at $r \rightarrow \infty$ is c_b, and the diffusive flux of material at the nanocrystal surface must equal the adsorption flux of material onto the surface given in Eq. (5.1). The remaining two boundary conditions are given by a quantitative treatment of the interface between the surfactant layer and the solution. Let there be a partition coefficient K_P at the interface which relates the solubility in the solution versus the solubility in the surfactant layer. If a monomer thermodynamically prefers the solution, then $K_P > 1$ and the concentration just inside the interface is lower than that just outside the interface, and vice versa for $K_P < 1$. This relation between the two concentrations at $r = R + \delta$ is the third boundary condition. The fourth boundary condition is a mass balance at the interface, i.e. that the diffusive flux into the interface from the solution's side must equal the diffusive flux away from the surface on the surfactant layer's side. This boundary condition requires the diffusion coefficients within the surfactant layer (D_0) and in bulk solution (D_1). The four boundary conditions are as follows:

$$c_1(r \to \infty) = c_b \tag{5.4a}$$

$$D_0\left[\frac{\partial c_0}{\partial r}\right]_R = k_s\left(c_0(R) - c_\infty e^{2\gamma/RkT}\right) \tag{5.4b}$$

$$c_1(R+\delta) = K_P c_0(R+\delta) \tag{5.4c}$$

$$D_1\left[\frac{\partial c_1}{\partial r}\right]_{R+\delta} = D_0\left[\frac{\partial c_0}{\partial r}\right]_{R+\delta} \tag{5.4d}$$

The constants a_0, b_0, a_1, and b_1 are solved (see Appendix D for algebraic details) and the quantity $c_0(R)$ is computed. This value is inserted in Eq. (5.1) to yield the surfactant-mediate single particle growth rate:

$$\frac{dR}{dt} = v\frac{D_0}{R}\frac{\left(\frac{c_b}{K_P} - c_{sat}e^{2\gamma/RkT}\right)}{\left(\frac{D_0}{k_s R}+1\right)+\left(\frac{D_0}{K_P D_1}-1\right)\frac{R}{R+\delta}} \tag{5.5}$$

Eq. (5.5) is modified in two ways, as per LSW theory. The exponential Gibbs-Thomson term is approximated by its linear Taylor expansion, and the bulk concentration c_b is replaced by a critical radius R_c. Again, R_c is defined such that for which $dR/dt = 0$ evaluated at $R = R_c$. The resultant equation is:

$$\frac{dR}{dt} = \frac{2\gamma v^2 c_{sat}}{kT} \frac{D_0}{R} \frac{\left(\frac{1}{R_c} - \frac{1}{R}\right)}{\left(\frac{D_0}{k_s R} + 1\right) + \left(\frac{D_0}{K_P D_1} - 1\right) \frac{R}{R + \delta}} \tag{5.6}$$

with the critical radius R_c now defined

$$R_c = \frac{2\gamma v}{kT} \frac{K_P c_{sat}}{c_b - K_P c_{sat}} = \frac{2\gamma v}{kT} \frac{c_\infty}{c_b - c_\infty} \tag{5.7}$$

Because c_{sat} is the solubility of monomers in the surfactant layer, the product $K_P c_{sat} = c_\infty$ represents the solubility in the solution. To compare the new growth rate Eq. (5.6) with that used in LSW theory, we examine the reaction-limited and the diffusion-limited cases. The reaction-limited growth rate, with $D_0 >> k_s R$, is as follows:

$$\frac{dR}{dt} = \frac{2\gamma v^2 c_{sat} k_s}{kT} \left(\frac{1}{R_c} - \frac{1}{R}\right)$$

This rate law is indistinguishable from the reaction-limited growth law for a nanocrystal with no surfactant layer. The only difference is that the growth rate depends on c_{sat} instead c_∞, but to within a constant the behavior is identical; therefore, all equations given in LSW theory for a reaction-limited Ostwald ripening system apply equally well to both bare and surfactant-coated particles.

The equivalent diffusion-limited case with $D_0 << k_s R$ provides a novel relation:

$$\frac{dR}{dt} = \frac{2\gamma v^2 c_\infty D_1}{kT} \frac{D_0}{K_P D_1} \frac{\frac{1}{R}\left(\frac{1}{R_c} - \frac{1}{R}\right)}{1 + \left(\frac{D_0}{K_P D_1} - 1\right)\frac{R}{R+\delta}} \tag{5.8}$$

This diffusion-limited growth rate differs notably from LSW theory in that there is now an *R*-dependent denominator. Note that when $D_0 = K_P D_1$ or when $\delta = 0$, i.e. when the surfactant layer is not at all different from bulk solution, Eq. (5.8) reduces to quantitatively to the LSW rate.

To determine the quantitative effect of a surfactant layer on nanocrystal growth, we restrict our analysis to $\delta > 0$ and $D_0/K_P D_1 \neq 1$. Under these conditions, the surfactant layer has a non-negligible effect on the monomer flux and nanocrystal growth. Let us define a monomer flux coefficient η as follows:

$$\eta = \frac{D_0}{K_P D_1} - 1 \tag{5.9}$$

The monomer flux coefficient η represents the relative flux of monomers through the surfactant layer versus that through bulk solution. Values of $\eta > 0$ indicate that monomer flux is enhanced in the surfactant layer (because of higher permeability and/or greater mobility), while $-1 < \eta < 0$ indicates the flux of monomers is inhibited through the surfactants. $\eta = -1$ represents an impermeable surfactant layer, in which case *dR/dt* is uniformly zero for all $\delta > 0$. Employing η

and the LSW constant $K_D = 2\gamma v^2 c_\infty D_1/kT$ (the definition of which has not changed from LSW theory) allows this simplification of the single-particle growth rate in its diffusion-limited form:

$$\frac{dR}{dt} = \frac{K_D}{R^2}\left(\frac{R}{R_c} - 1\right)\frac{1+\eta}{1+\eta\dfrac{R}{R+\delta}} \tag{5.10}$$

This equation is plotted in Figure 5.2 for several values of η and δ. Other features are evident from Eq. (5.10). First, note that *dR/dt* has a maximum value R_{max} for any $\eta\delta > 0$, and *dR/dt* decreases with *R* beyond that point. Therefore, the surfactant coating on a particle does not disrupt the potential for size-focusing. Additionally, as the particle grows, the ratio of surfactant length to particle size, δ/R decreases. In the limit $\delta/R \to 0$, the last term in Eq. (5.10) quickly approaches unity and the LSW growth rate is recovered. Meanwhile, for η values of small magnitude, the last term in Eq. (5.10) depends very weakly on *R*, and *dR/dt* is merely perturbed from the LSW growth rate. The following is thus generally implied: if surfactants grafted to a nanocrystal have tails with very similar transport properties to the solvent, or if the surfactants

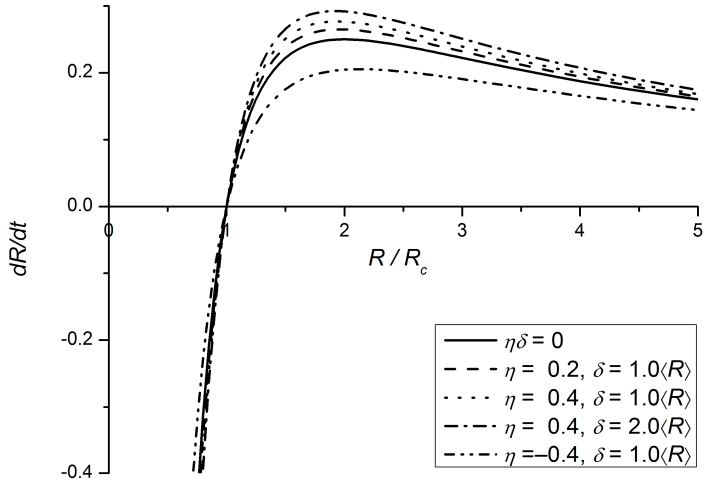

Figure 5.2: Modified single-particle growth rate as given in Eq. (5.10). The solid line represents the original LSW growth rate. Dashed and dotted lines represent the growth rate for different surfactant layer properties, δ = surfactant layer depth and η = surfactant layer transport enhancement. All growth rates decrease for large *R*, thus size focusing is possible.

are very short compared to the nanocrystal radius, then the surfactant-coated nanocrystal will display the same growth patterns as a bare nanocrystal.

To have any impact on the growth kinetics of a nanocrystal, η and δ must both be significant. The behavior of surfactant-coated nanocrystals in the regime of Ostwald ripening and in the regime of production-controlled growth and size-focusing is derived herein. The growth patterns of bare spherical nanocrystals and surfactant-coated spherical nanocrystals will thus be quantitatively compared. Because Eq. (5.10) reduces to the LSW growth rate for $\eta\delta = 0$, whatever results are derived will also reduce to the LSW results when $\eta\delta = 0$.

5.3 OSTWALD RIPENING OF SURFACTANT-COATED NANOCRYSTALS:

The derivation of the Ostwald ripening behavior will mirror that LSW theory almost exactly. Most of the derivation will be found in the Appendix D, but the key details are listed here. We begin with the instantaneous material balance which already includes the growth rate:

$$\frac{dc_b}{dt} = -\frac{4\pi K_D}{v}\int_0^\infty \left(\frac{R}{R_c} - 1\right)\frac{1+\eta}{1+\eta\dfrac{R}{R+\delta}}\, f(R,t)\,dR \tag{5.11}$$

We presume a pseudo-steady state, $dc_b/dt \approx 0$, based on the extremely small solubility of crystalline materials and the fact that c_b asymptotically approaches solubility c_∞ as the average particle size growth to infinite size. As a result, the integral of the function evaluates to approximately zero. The integrand is somewhat weakly dependent on η if any small range of R is

considered, regardless of δ, thus the value of the integral can be accurately replaced with the crude approximation:

$$0 = \left(\frac{\langle R \rangle}{R_c} - 1 \right) \frac{1+\eta}{1+\eta \frac{\langle R \rangle}{\langle R \rangle + \delta}} \tag{5.12}$$

Trial distributions of *f(R,t)* as wide as 40% coefficient of variance confirm this approximation is within 2% of the accurate integral. Therefore, the LSW result $\langle R \rangle = R_c$ is an acceptable approximation to Eq. (5.11).

The size distribution function *f(R,t)* obeys the following continuity equation:

$$\frac{\partial f}{\partial t} = -\frac{\partial}{\partial R}\left(f \frac{dR}{dt} \right) \tag{5.13}$$

The rate of change of the number of nanocrystals is given by the rate of total dissolution of the smallest nanocrystals multiplied by their population:

$$\frac{dZ}{dt} = \frac{d}{dt} \int_0^\infty f(R,t) dR = -K_D (1+\eta) \lim_{R \to 0} \left(\frac{f(R,t)}{R^2} \right) \tag{5.14}$$

Note that the quantity $K_D(1+\eta)$ indicates that transport through the surfactant layer determines *dZ/dt*, not transport through the solvent. However, as per the LSW result, the distribution *f(R,t)*

must always be proportional to R^2 in the small-R limit. We continue to mirror the LSW form of the distribution by establishing a time-dependent dimensionless radius and restating Eq. (5.10)

$$\rho = \frac{R}{R_c(t)} \tag{5.15}$$

$$\frac{dR}{dt} = \frac{K_D}{R_c^2}\frac{\rho - 1}{\rho^2}\frac{1+\eta}{1+\eta\frac{\rho}{\rho+\delta'}} \tag{5.16}$$

Separation-of-variables is again used to define the size distribution function at long times:

$$f(R,t) = g(t)\rho^2 h(\rho) \tag{5.17}$$

where $h(0) = 1$ arbitrarily. Inserting the definition Eq. (5.17) into the evolution equation Eq. (5.13) gives the following result:

$$\rho^2 h(\rho)\frac{1}{g}\frac{dg}{dt} - \left[\rho^3\frac{dh}{d\rho} + 2\rho^2 h(\rho)\right]\frac{1}{R_c}\frac{dR_c}{dt} = -\frac{K_D}{R_c^3}\frac{d}{d\rho}\left[h(\rho)(\rho-1)\frac{1+\eta}{1+\eta\frac{\rho}{\rho+\delta'}}\right] \tag{5.18}$$

The time-dependent quantities $(1/g)\cdot dg/dt$ and $(1/R_c)\cdot dR_c/dt$ must now be established. LSW theory uses the original pseudo-steady approximation, $dc/dt \approx 0$, to declare that the total volume fraction of nanocrystals, defined as φ, remains constant regardless of how $f(R,t)$ evolves. This declaration resolves $(1/g)\cdot dg/dt$:

$$\varphi = \int_0^\infty \frac{4\pi R^3}{3} f(R,t) dR = \frac{4\pi R_c{}^4 g(t)}{3} \int_0^\infty \rho^5 h(\rho) d\rho \tag{5.19}$$

Therefore:

$$\frac{1}{g(t)} \frac{dg}{dt} = -\frac{4}{R_c} \frac{dR_c}{dt} \tag{5.20}$$

By plugging Eq. (5.17) into both sides of Eq. (5.14) and combining the result with Eq. (5.20), an expression for dR_c/dt is obtained:

$$\frac{dR_c^3}{dt} = \frac{K_D(1+\eta)}{\gamma_D} \tag{5.21}$$

where

$$\gamma_D = \int_0^\infty \rho^2 h(\rho) d\rho \tag{5.22}$$

Eq. (5.21) and Eq. (5.22) are equivalent to their LSW definitions to within a constant. These definitions allow Eq. (5.18) to be simplified into an ordinary differential equation in ρ only:

$$\left(\frac{\rho^3}{3\gamma_D} - \frac{\rho - 1}{1 + \eta \frac{\rho}{\rho + \delta'}} \right) \frac{dh}{d\rho} = h(\rho) \left[-\frac{6}{3\gamma_D} \rho^2 + \frac{1}{1 + \eta \frac{\rho}{\rho + \delta'}} - \frac{\rho - 1}{1 + \eta \frac{\rho}{\rho + \delta'}} \frac{\eta \delta'}{(\rho + \delta')^2 \left(1 + \eta \frac{\rho}{\rho + \delta'}\right)} \right] \tag{5.23}$$

Although γ_D is unknown, it depends on the solution to $h(\rho)$, thus the solution to Eq. (5.23) exists and is self-consistent. The details of the solution and approximations made therein are expanded

in Appendix D, and only the results are shown here for clarity. ρ_{pole} and γ_D are thus approximated by the following formulas:

$$\rho_{pole} \approx \frac{3+\dfrac{\eta\delta'^{\frac{3}{2}}}{\left(1+\eta\frac{\frac{3}{2}}{\frac{3}{2}+\delta'}\right)\left(\frac{3}{2}+\delta'\right)^2}}{2+\dfrac{\eta\delta'^{\frac{3}{2}}}{\left(1+\eta\frac{\frac{3}{2}}{\frac{3}{2}+\delta'}\right)\left(\frac{3}{2}+\delta'\right)^2}} \tag{5.24}$$

$$\gamma_D \approx \frac{9}{4}\left(1+\eta\frac{\frac{3}{2}}{\frac{3}{2}+\delta'}\right) \tag{5.25}$$

These approximations are accurate out to order $(\eta\delta/R_c)^2$. Values obtained from Eq. (5.24) are close to the accurate numerical solutions, within a factor of 10^{-3} for $-¼ < \eta < ¼$ and within a factor of 10^{-3} for $-½ < \eta < 1$, regardless of δ. Values from Eq. (5.25) are slightly less accurate for γ_D, with a 1% error from the numerical solutions for any $|\eta| < 1$. The accuracy is marginally increased if the 3/2 terms in Eq. (5.25) are *post facto* replaced by ρ_{pole}. The real utility of these approximations, however, is that employing them in Eq. (5.23) allows a closed-form expression for the differential equation of *h*:

$$\frac{d\ln h}{d\rho} = \frac{-\dfrac{24}{27\left(1+\eta\frac{\rho_{pole}}{\rho_{pole}+\delta'}\right)}\rho^2 + \dfrac{1}{1+\eta\frac{\rho}{\rho+\delta'}} - \dfrac{\rho-1}{1+\eta\frac{\rho}{\rho+\delta'}}\dfrac{\eta\delta'}{(\rho+\delta')^2\left(1+\eta\frac{\rho}{\rho+\delta'}\right)}}{\dfrac{4\rho^3}{27\left(1+\eta\frac{\rho_{pole}}{\rho_{pole}+\delta'}\right)} - \dfrac{\rho-1}{1+\eta\frac{\rho}{\rho+\delta'}}} \tag{5.26}$$

The numerator of this expression can be separated into two pieces to yield the following:

$$\frac{d\ln h}{d\rho} = -\frac{\frac{d}{d\rho}\left[\frac{4\rho^3}{27\left(1+\eta\frac{\rho_{pole}}{\rho_{pole}+\delta'}\right)} - \frac{\rho-1}{1+\eta\frac{\rho}{\rho+\delta'}}\right]}{\frac{4\rho^3}{27\left(1+\eta\frac{\rho_{pole}}{\rho_{pole}+\delta'}\right)} - \frac{\rho-1}{1+\eta\frac{\rho}{\rho+\delta'}}} + \frac{-\frac{12}{27}\rho^2}{\frac{4\rho^3}{27} - (\rho-1)\frac{1+\eta\frac{\rho_{pole}}{\rho_{pole}+\delta'}}{1+\eta\frac{\rho}{\rho+\delta'}}} \tag{5.27}$$

The first term is easily integrable, and the second term is almost identical to the differential equation given by Wagner for the bare-particle diffusion-limited system. The final approximation made in this Ostwald ripening model is to remove the η-dependence in the last term of Eq. (5.27), introducing error on the order of $|\eta(\rho_{pole} - \rho)|$. Accordingly, the solution to $h(\rho)$ will be relevant for small η, i.e. for surfactants very similar to the solvent.

The final form of $h(\rho)$ is solved and given here in the time-independent ρ-size distribution function:

$$\frac{1}{\gamma_D}\rho^2 h(\rho) = \left(\frac{\frac{4\rho^3}{27} - (\rho-1)}{\frac{4\rho^3}{27} - (\rho-1)\frac{1+\eta\frac{\rho_{pole}}{\rho_{pole}+\delta'}}{1+\eta\frac{\rho}{\rho+\delta'}}}\right)\frac{4}{9}\rho^2\left(\frac{3}{\rho+3}\right)^{7/3}\left(\frac{\frac{3}{2}}{\frac{3}{2}-\rho}\right)^{11/3}\exp\left(-\frac{\rho}{\frac{3}{2}-\rho}\right) \times\exp\left(O\left(\eta\frac{\rho_{pole}}{\rho_{pole}+\delta'} - \eta\frac{\rho}{\rho+\delta'}\right)\right) \tag{5.28}$$

With the exception of the first term in parentheses and the error-order term, this distribution is identical to the LSW distribution for an Ostwald ripening system. The first term is always

between $1-\eta$ and 1 over the whole interval $0 < \rho < \rho_{pole}$, and it approaches unity as the particles grow and δ/R_c decreases. Additionally, numerical integration of Eq. (5.23) indicate that Eq. (5.28) provides an accurate approximation to *f(R,t)* for $\eta\delta \sim 10^{-1}$ or less. The result in Eq. (5.28) is pictorially represented in Figure 5.3.

Finally, the definition of γ_D in Eq. (5.25) is used to establish the rate of change of R_c.

$$\frac{dR_c^{\,3}}{dt} = \frac{1+\eta}{1+\eta\frac{\rho_{pole}}{\rho_{pole}+\delta'}}\frac{4}{9}K_D \tag{5.29}$$

The mass balance given by Eq. (5.11) does not explicitly declare $R_c = \langle R \rangle$, but numerical integrations of Eq. (5.11) using Eq. (5.28) for the size distribution function reveal that $\langle R \rangle$ is within 1% of R_c regardless of η and δ. Given that measurement error in nanocrystal experiments is well above 1%, the growth law for R_c^3 also correctly characterizes the average radius:

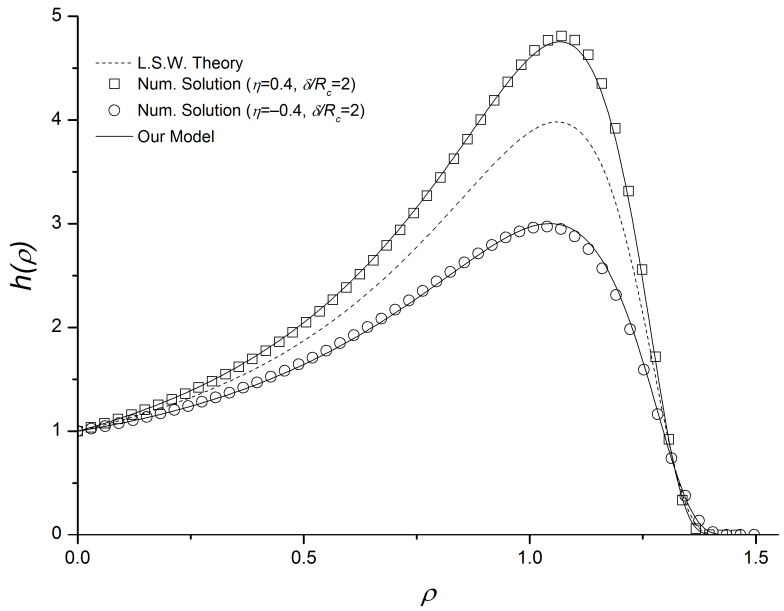

Figure 5.3: The static-shape size distribution function $h(\rho)$. The dotted line is the LSW form for classical Ostwald ripening. The two solid lines represent the distribution for two different kinds of surfactant-coated nanocrystals, as calculated by Eq. (5.28): $\eta = 0.4$ with $\delta/R_c = 2$, and $\eta = -0.4$ with $\delta/R_c = 2$. Also included are points, squares and circles, which are numerical integrations of the differential equation Eq. (5.23), validating the approximations made in obtaining Eq. (5.28).

$$\frac{d\langle R\rangle^3}{dt} = \frac{1+\eta}{1+\eta\frac{3\langle R\rangle}{3\langle R\rangle+2\delta}}\frac{4}{9}K_D \tag{5.30}$$

This growth law is nearly identical to the LSW result in Eq. (3.19) for δ of order $\langle R\rangle$ or smaller, regardless of the value of η. For nanocrystal experiments, where measurement error is high, Eq. (5.30) is indistinguishable from the growth law given by LSW theory.

5.4 MODIFYING THE THEORY OF SIZE FOCUSING

The analysis of Ostwald ripening for surfactant coated-nanocrystals followed the derivation of LSW theory of bare nanocrystals very closely. In an equivalent fashion, the derivation of the theory of size focusing of bare nanocrystals given in Chapter 4, will be employed to determine the growth behavior of surfactant-coated nanocrystals in the production-controlled regime. The material balance (Eq. 5.11 above) is modified by introducing $\dot{c}$, the molar-per-time rate of generation of new monomer in solution.

$$\frac{dc}{dt} = \dot{c} - \frac{4\pi K_D}{v}\int_0^\infty \left(\frac{R}{R_c}-1\right)\frac{1+\eta}{1+\eta\dfrac{R}{R+\delta}}f(R,t)dR \tag{5.31}$$

It has already been established (Section 5.2) that the integral quantity can be approximated to within 1% by replacing all instances of R with the average $\langle R\rangle$. Such a replacement is accurate because *f(R,t)* is still sufficiently narrow even in an Ostwald ripening system. The theory of size focusing declares that *f(R,t)* is narrower than the Ostwald ripening case whenever $\dot{c}$ is large,

validating such an approximation here. That identity allows the re-definition of the size focusing coefficient, ξ:

$$\xi = \frac{\dot{c}v}{4\pi Z}\frac{1}{K_D} = \left(\frac{\langle R\rangle}{R_c} - 1\right)\left(\frac{1+\eta}{1+\eta\frac{\langle R\rangle}{\langle R\rangle+\delta}}\right) \tag{5.32}$$

It is clear that for $\eta = 0$ or $\delta << R$, the definition of ξ for surfactant-coated nanocrystals reverts to that given in Chapter 4. Further replicating the derivation of Chapter 4, the time-wise behavior of *f(R,t)* is examined by presuming *f(R,t)* is a Gaussian function with time dependent mean $\langle R\rangle$ and variance σ. Using this Gaussian distribution in evolution equation Eq. (5.13) yields a formula relating the time-dependent behavior of $\langle R\rangle$ and σ to the growth parameters K_D and ξ. Because the Gaussian approximation is not valid across all $0 < R < \infty$, regular perturbation theory is employed about the average $R = \langle R\rangle$. The details are similar to those in the expanded derivation of the size-focusing theory in Appendix B, but the main result is two relations for the time-dependent behavior of $\langle R\rangle$ and σ:

$$\frac{1}{\sigma}\frac{d\sigma}{dt} = \frac{K_D\xi}{\langle R\rangle^3}\left\{\frac{1}{\xi} - \left[\frac{1+\eta\frac{\langle R\rangle^2+2\langle R\rangle\delta}{\langle R\rangle^2+2\langle R\rangle\delta+\delta^2}}{1+\eta}\right]\right\} \tag{5.33a}$$

$$\frac{d\langle R\rangle}{dt} = \frac{K_D\xi}{\langle R\rangle^2} \tag{5.33b}$$

Eq. (5.33a) comes from the zero-order perturbation and Eq. (5.33b) comes from the first-order perturbation. The second-order perturbation reveals an equation which is identical to Eq. (5.33a) for any distribution with $\sigma^2/\langle R\rangle^2 << 1$. Given that the Ostwald ripening distribution has $\sigma^2/\langle R\rangle^2$ of about 5%, Eq. (5.33a) suffices.

Just as in Chapter 4, Eq. (5.33a) reveals that σ will decrease with time for any $\xi > 1$. Eq. (5.33b) reduces to the same growth law $d\langle R\rangle^3/dt = 3K_D\xi$ that is given in Chapter 4 when the distribution gets sufficiently narrow, $\sigma^2 << \langle R\rangle^2$. Inserting Eq. (5.33b) into Eq. (5.33a) and integrating yields the following power law:

$$\frac{\sigma}{\sigma_0} = \left(\frac{\langle R\rangle}{\langle R\rangle_0}\right)^{\frac{1}{\xi}-\frac{1}{1+\eta}\left(1+\eta\frac{\langle R\rangle^2+2\langle R\rangle\delta}{\langle R\rangle^2+2\langle R\rangle\delta+\delta^2}\right)} \tag{5.34}$$

In the case $\xi \to \infty$, the bare-nanocrystal power law ($\eta = 0$ or $\delta = 0$) yields $\sigma \propto 1/\langle R\rangle$. For surfactant-coated nanocrystals, however, the exponent in the $\xi \to \infty$ limit depends on η and δ. The dependence on η is critical, because **negative values of η will yield a power law where σ decreases faster than $1/\langle R\rangle$**. Conversely, positive values of η will inhibit size focusing and limit the degree of size focusing that is permissible in production-controlled growth. Note that the relationship is inverted between monomer transport and size focusing: inhibiting monomer transport ($\eta < 0$) will enhance the size-focusing exponent, while promoting monomer transport ($\eta > 0$) will reduce the effect of size focusing.

This is the essential result of this study: a surfactant which hinders monomer transport, through either a diminished solubility or a lower diffusivity, will enhance the size focusing effect and produce more monodisperse nanocrystals than nanocrystals with no surfactant.

5.5 DISCUSSION OF THE EFFECTS OF SURFACTANTS

The primary result is not intuitive, but it is based on a geometric reasoning. Let us examine bare nanocrystals first and then extend the ideas to the surfactant layer. For two bare nanocrystals with a local monomer concentration c_i at their interface, the concentration gradient is equal and the diffusion rate of monomers leaving the bulk (in volume-per-time) is equal. Once those monomers reach each nanocrystal, however, the larger nanocrystal must distribute the same volume of adsorbing monomers over a larger volume. The result is a smaller difference in the larger nanocrystal's radius for any given concentration gradient, $c_i - c_b$. This surface-to-volume ratio argument explains the D/R factor in the diffusion-limited version of the single-particle growth rate. It also reveals that reaction-limited growth has no size-dependent prefactor because the adsorbing monomers need not come from the bulk, as they are already at the surface.

The same logic applies to surfactant-mediated growth. In this case, however, the monomers leave the bulk, pass through the interface between the surfactant layer and the solution, and diffuse toward the nanocrystal surface. The rate of transport between each diffusion layer is determined solely by their respective concentration gradients, but the effect they have on nanoparticle growth depends on the ratios between their various surface areas. As a result, the surface-to-volume ratio of the nanocrystal remains important, but now the ratio of the nanocrystal's surface area to the surfactant-layer interface's area $4\pi(R + \delta)^2$ is also relevant. If the particle is much

larger than the surfactant layer, then this ratio approaches unity and the surfactant-coated nanocrystal behaves like a bare nanocrystal.

5.6 VALIDATION OF THE MODEL

Unfortunately, no experimental evidence exists to verify our results. The size distribution of Ostwald ripening nanocrystals is so imprecise that comparison to Eq. (5.28) is moot. Examining the slope of $\langle R \rangle^3$ vs. time is more feasible, but the measurement error would mask the variances that even moderately different surfactants could cause. Even if two experiments are accurately fitted to Eq. (5.30), it would be very difficult to distinguish whether the differences are due to the transport effects addressed here, or due to variable miscibility of the surfactant in the solvent.

Comprehensive studies of size focusing have a much better chance of observing differences between nanocrystals growing with different grafted surfactants. However, as noted in Chapter 4, no comprehensive studies of size focusing are currently available, thus any quantitative evidence of the surfactant's effect on growth is not likely to exist. Futher experimentation is therefore necessary. Additionally, numerical analysis with the use of Mantzaris' population balances was attempted to validate the model. However, the new growth rate Eq. (5.10) introduces some numerical instability to the algorithm such that small fluctuations in the function $f(R,t)$ diverge with time. The pursuit of numerical verification is ongoing.

5.7 CONCLUSION

We have modified two existing theories, LSW theory of Ostwald ripening and the theory of size focusing, to quantitatively account for the effect of grafted surfactants and their transport

properties. The results indicate that when the surfactant layer's transport properties are different from those of the bulk solution, the size-dependence of a nanocrystal's growth is dramatically altered. The Ostwald ripening rate and size distribution function are perturbed by surfactants, but not necessarily to any measurable degree in practice. Surfactants' effect on size focusing is much more profound, where the exponent n in the size-focusing power law $\sigma \propto 1/\langle R \rangle^n$ can be tuned through surfactant properties. With an appropriate choice of surfactants, n can be adjusted to values larger than 1, permitting a greater degree of size focusing than is possible for bare nanocrystals in the production-controlled limit.

CHAPTER 6

THERMODYNAMIC ANALYSIS OF DIGESTIVE RIPENING

6.1 THE MYSTERY OF DIGESTIVE RIPENING

While the gold colloid has been studied for hundreds of years, the last three decades have seen a renewed interest in nanometer-sized crystals of noble metals such as gold because of their size-dependent properties.[127] In a gold nanocrystal, the electrons exhibit more quantum mechanical behavior than in bulk gold, which manifests in their optical properties, tunneling behaviors, and surface plasmon properties, all of which are strongly size-dependent. Myriad studies have been conducted to synthesize gold nanocrystals for these applications, always with the goal to gain explicit control over the size and the polydispersity of the product nanocrystals.[26, 32, 45, 46, 72, 74, 128-130] Digestive ripening is one such technique for making monodisperse gold nanocrystals, and it is of particular interest due to its viability for industrial-scale manufacturing.[26, 45-47]

In this fascinating phenomenon gold nanocrystals that are relatively large and very polydisperse can be forced to spontaneously and rapidly shrink into a population of small, monodisperse-sized gold nanocrystals, merely by the addition of excess amounts of a surfactant.[26, 45, 46] Specifically, gold nanocrystals of 2-80nm in toluene are exposed to dodecanethiol, for example, with a 30:1 thiol-to-gold ratio. Instantly, a color change is witnessed, and TEM images taken minutes after the surfactant injection show small, spherical gold nanocrystals with sizes in the range 2-6nm. The mixture is refluxed in toluene (110ºC) for 2 hours, and a subsequent TEM revealed that the distribution had become even more monodisperse, with product nanocrystal

sizes of 4.7±0.4 nm. These highly monodisperse gold-thiolate nanocrystals remain stable for months at room temperature, and are high enough quality for industrial applications. Conducting the digestive ripening experiment with different surfactants (thiols with different alkyl chain lengths, alkyl compounds with different head groups) showed clearly that the choice of head group dramatically changed the product nanocrystals' size and polydispersity, while the alkyl chain length had a weak effect.[45, 46]

Digestive ripening of materials other than gold has also been witnessed. Silver and palladium nanocrystals covered by either thiol or amine surfactants can be produced by digestive ripening.[47] Bulk-sized zinc sulfide crystals can be digestively ripened by dodecanethiol at 100ºC.[131] In a different fashion, iron and cobalt nanocrystals also undergo digestive ripening in the presence of oleic acid, but only if the acid-to-metal ratio is less than 1.[48, 49] When the acid-to-metal ratio is incresed to 2.5:1, no nanocrystals form and instead, a species known as "molecular clusters" are formed in which 2-3 metals ions are bound to 3 oleate ions. Molecular cluster retain no properties of the solid metal. Additionally, a separate study took digestively-ripened gold-thiolate nanocrystals and heated them to 300ºC in dioctyl ether, also resulting in gold-thiolate molecular clusters after a slow reaction.[92] While it is trivial to explain the metal-and-oleic acid results by assuming the crystal-surfactant binding is stronger than crystal-crystal cohesion[48], it remains a mystery why stable gold-thiolate nanocrystals will form under certain conditions and gold-thiolate molecular clusters only slightly different conditions.

The only clear conclusion is that digestive ripening is caused by surfactants, but it is unknown what features of the surfactant cause the spontaneous digestion of nanocrystals. The result

resembles the formation of microemulsions, in which a surfactant stabilizes an immiscible solute-solvent mixture by forming size-stable swollen micelles.[132] Just as in digestive ripening, the formation of the swollen micelles is spontaneous and yields monodisperse aggregates. This would suggest that the process depends strongly on the surfactant tails, while hypotheses in recent literature state that favorable grafting causes digestive ripening.[133]

The big question regarding the gold-thiol digestive ripening phenomenon is this: What permits excess surfactant to digest large crystals but prevents further digestion of small crystals to molecular clusters? In essence, why does digestive ripening stop at the nanoscale? It is the goal of this publication to answer that question using a first-principles theoretical investigation.

A full thermodynamic model will be built which describes a system of nanocrystals that are coated by a monolayer of surfactants. To make the formulation as general as possible, nanocrystals of all sizes will be considered simultaneously, and the model will establish which size nanocrystals are most favorable. The model will include the crystal core free energy, the interaction of the surfactant and the crystal, and the intermolecular interactions between surfactants on the nanocrystal surface. An accurate model must predict five critical experimental results, listed as follows:

(I) Ostwald ripening of bare nanocrystals
(II) Ostwald ripening of certain surfactant-coated nanocrystals
(III) Formation of stable nanocrystals for certain surfactants at low surfactant-to-crystal ratios
(IV) Formation of molecular clusters for certain surfactants at high surfactant-to-crystal ratios and
(V) Stable microemulsions made of swollen micelles of surfactant, surrounding a solute core

If the model reproduces these cases, then it can be used to determine the process that separate stable 4.7-nm gold-thiolate nanocrystals in the presence of excess thiol from the other behaviors listed above.

Several theories have been proposed to describe the phenomenon of stable gold-thiol nanocrystals, including the treatment by Leff et al.[74] and the electrostatic model of Lee et al.[109] Each treatment has significant weaknesses in describing digestive ripening. The Leff model cannot explain why different surfactant head groups will affect the nanocrystal size, and it does not predict the existence of molecular clusters, which is critical experimental result (IV). The Lee model has even greater weakness in that the electrostatic explicitly prohibits molecular clusters and no justification is offered for why Ostwald ripening occurs in the absence of surfactant. As a result, the Lee model reproduces none of the critical experimental behaviors listed above. To address all of these behaviors, our treatment is essentially a generalization of the Leff model, addressing the statistical existence of all nanocrystals simultaneously and explicitly including all energetic and entropy contributions of the global system. This effort is the most comprehensive thermodynamic model of surfactant-coated nanocrystals to date, and will establish the exact circumstances under which finite-size nanocrystals are at equilibrium.

6.2 THERMODYNAMIC MODEL

The model we use for the free energy will start in the global limit, considering the entire population of nanocrystals. The results should be analogous to Israelichvili's model for micellization of an amphiphile.[110] Isrealichvili considers all *N*-mer aggregates of amphiphiles

simultaneously through a function X_N, the mole fraction of amphiphiles that are aggregated into an *N*-mer micelle. The translational entropy of all *N*-mer micelles is $(X_N/N)\ln(X_N/N)$, which is balanced by the standard-state chemical potential of amphiphiles in an *N*-mer micelle, μ_N^o. The free energy is minimized with Lagrange multipliers with conservation of mass as the constraint, and all the mole fractions X_N are explicitly related at equilibrium by thermodynamics. The model predicts an optimum point in the competition between the energy gain and the entropic loss of aggregation, leading to a thermodynamically stable micelle size.

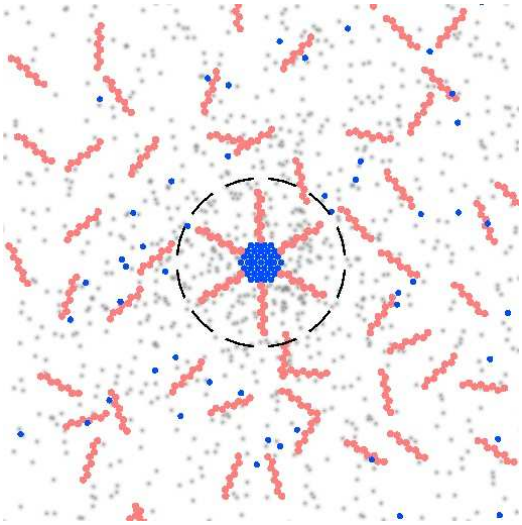

Figure 6.1: Graphical respresentation of the thermodynamic model. Blue dots represent crystal monomers; red chains represent surfactants; gray dots represent solvent; and the dotted circle delineates the volume $V_{n,m}$.

The formation of a surfactant-mediated nanocrystal, however, involves more than the self-assembly of an amphiphile. Our more complete free energy will be a function of two variables, the number of crystal atoms *n* and the number of grafted surfactants *m* in a nanocrystal. The free energy of surfactant interactions will be treated using Single Chain Mean Field theory, a theoretical model of polymer interactions in a finite system.[134] Under this framework, the Gibbs free energy of the system can be fully developed and minimized to establish quantitative expressions for surfactant-grafted nanocrystals at equilibrium.

The model presumes a global solution which comprises the following: N_{solv} solvent molecules, N_C dissolved crystal atoms, N_S dissolved surfactant molecules, and (for every integer

combination of n and m) N_{nm} nanocrystals made of n crystallized atoms and m bound surfactants. Each nanocrystal is presumed spherical, with a crystal core of n atoms, and each of the m surfactants is bound by its head group to the crystal core's surface. Let each n-sized nanocrystal include a volume $V_{n,m}$ around it, which encompasses all m surfactant molecules and all the solvent that interpenetrates the surfactants. $V_{n,m}$ is spherically symmetric, and reflects the volume occupied by surfactants of length L, and its magnitude within the Gibbs free energy varies solely with n. Figure 6.1 illustrates this model graphically for a single nanocrystal in solution.

The Gibbs free energy of such a system is here defined, where the free energy of the solution and the free energy of each nanocrystal is separated into individual terms.

$$G = G_{solution} + \sum_{\{nanocrystals\}} \left(G_{crystal} + G_{surfactant} + G_{solvent} \right) \quad (1)$$

$G_{solution}$ includes the total translational entropy which is calculated using the lattice model with N_{solv} free solvent molecules, N_S free surfactants, N_C free crystal monomers, and (for every n and m) $N_{n,m}$ indistinguishable nanoparticle clusters, occupying a total ($N_C + N_S + N_{solv} + \Sigma_n \Sigma_m N_{n,m}$) lattice sites. Also, each of the N_S dissolved surfactant molecules may exist in a set of possible conformations, $\{\eta\}$. Each conformation η has an internal energy $u_{int}(\eta)$ and a probability $P_f(\eta)$. (The set $\{\eta\}$ and its probabilities $P_f(\eta)$ anticipate the use of SCMF theory.) With this framework, the free energy of the solution is calculated:

$$\frac{G_{solution}}{kT} = N_C \ln N_C + N_S \ln N_S + N_{solv} \ln N_{solv} + N_S \sum_{\{\eta\}} P_S(\eta)[\ln P_S(\eta) + \beta u_{\text{int}}(\eta)] + \sum_{n=1}^{\infty} \sum_{m=\delta_{n1}}^{\infty} N_{n,m} \ln N_{n,m} - \left(N_C + N_S + N_{solv} + \sum_{n=1}^{\infty} \sum_{m=\delta_{n1}}^{\infty} N_{n,m} \right) \ln \left(N_C + N_S + N_{solv} + \sum_{n=1}^{\infty} \sum_{m=\delta_{n1}}^{\infty} N_{n,m} \right) \quad (6.2)$$

Next we examine a single nanocrystal, which comprises a solid crystal core (made of *n* atoms) and a layer of solution (of volume $V_{n,m}$) in which solvent and the alkyl tails of the surfactants mix. The crystal core has bulk crystallization energy g_{crys} per atom and an unfavorable surface energy γ. (Gold nanocrystals as small as 2 nm retain the fcc structure of bulk gold, thus g_{crys} is assumed to be constant for most nanocrystal sizes.) Within the surfactant volume $V_{n,m}$, let the solvent volume fraction be a space-varying function, $\phi_s(\mathbf{r})$. The solvent is presumed athermal, thus its free energy is entirely described by its total translational entropy integrated over the volume, $kT \cdot \int_{Vnm} d\mathbf{r} \cdot 1/v_s \cdot \phi_s(\mathbf{r}) \cdot \ln[\phi_s(\mathbf{r})]$, where v_s is the volume of a solvent molecule.[134, 135]

Next, the grafted surfactants are addressed through the use of Single Chain Mean Field Theory, which is described in great detail elsewhere.[134] Grafted surfactants exist in a series of conformations $\{\alpha\}$ each of which has a probability $P_g(\alpha)$, which are related to the conformations $\{\eta\}$ of dissolved surfactants. The free energy of the surfactants has four contributions: the grafting energy ε_{graft}, the conformational entropy $\Sigma_{\{\alpha\}} P_g(\alpha) \ln P_g(\alpha)$, the internal energy of each conformation $\beta u_{int}(\alpha)$, and the energetic interactions between surfactants throughout $V_{n,m}$. The intermolecular interactions between surfactants are modeled by a double-volume integral, where surfactant tail-monomers in every volume element $d\mathbf{r}$ in $V_{n,m}$ interact with tail-monomers in every other volume element $d\mathbf{r}'$ in $V_{n,m}$ through a prescribed pair potential, $X(|\mathbf{r}-\mathbf{r}'|)$. The tail-

monomer density at each location is $\rho(\mathbf{r})$ and $\rho(\mathbf{r}')$, and total energy of tail-tail interactions is $\rho(\mathbf{r})X(|\mathbf{r}\text{-}\mathbf{r}'|)\rho(\mathbf{r}')$ integrated over all $\mathbf{r}, \mathbf{r}' \in V_{n,,m}$. Combining the free energies of the crystal core, the surfactants, and the solvent gives us the total free energy of a single *n,m*-nanocrystal in solution:

$$\begin{aligned} G_{crystal} + G_{surfactant} + G_{solvent} &= ng_{crys} + 4\pi\left(\frac{3vn}{4\pi}\right)^{2/3}\gamma \\ &+ m\varepsilon_{graft} + mkT\sum_{\alpha} P_g(\alpha:n,m)\left[\ln P_g(\alpha:n,m) + \beta u_{\text{int}}(\alpha)\right] \\ &+ \frac{\omega_{TT}}{2}\int_{V_{n,m}}\int_{V_{n,m}} d\vec{r}\,d\vec{r}\,'\rho(\vec{r}:n,m)X\left(\left|\vec{r}-\vec{r}\,'\right|\right)\rho(\vec{r}\,':n,m) \\ &+ kT\int_{V_{n,m}} d\vec{r}\,\frac{1}{v_s}\phi_s(\vec{r}:n,m)\ln\left(\phi_s(\vec{r}:n,m)\right) \end{aligned} \tag{6.3}$$

The tail-monomer density $\rho(\mathbf{r})$ is calculated through $P_g(\alpha)$ and $n_g(\mathbf{r},\alpha)$, which is defined as the local number-density of tail-monomers at location $\mathbf{r}$ due to conformation α. For *m* grafted surfactants, $\rho(\mathbf{r}) = m\Sigma_{\{\alpha\}}P_g(\alpha)n_g(\mathbf{r},\alpha)$. Furthermore, the interaction $X(|\mathbf{r}-\mathbf{r}'|)$ between tail monomers is chosen such tail monomers are attracted by London forces when the monomer-monomer distance is greater than *l*, thus for $|\mathbf{r}-\mathbf{r}'| > l$, $X(r) \sim (l/r)^6$. *X* is defined as zero for any distance less than *l* to eliminate diverging integrals. The tail-tail interaction is thus re-stated:

$$\int_{V_{n,m}}\int_{V_{n,m}} d\vec{r}\,d\vec{r}\,'\left[m\sum_{\alpha}P(\alpha:n,m)n_g(\vec{r},\alpha)\right]X(\vec{r},\vec{r}\,')\left[m\sum_{\alpha'}P(\alpha':n,m)n_g(\vec{r}\,',\alpha')\right]$$

$$X(\vec{r},\vec{r}\,') = \begin{cases} 0 & \left|\vec{r}-\vec{r}\,'\right| < l \\ \left(\dfrac{l}{\left|\vec{r}-\vec{r}\,'\right|}\right)^6 & \left|\vec{r}-\vec{r}\,'\right| \geq l \end{cases} \tag{6.4}$$

The free energy must be minimized subject to certain constraints which are given by conservation laws. These constraints are placed in the free energy expression through Lagrange multipliers during minimization to ensure a physical result. The three constraints are: the mass balance of crystal atoms, with Lagrange multiplier λ_C; the mass balance of surfactant molecules, with Lagrange multiplier λ_S; and the mass balance of all solvent molecules in solution and contained in every volume $V_{n,m}$ across all nanocrystals, with Lagrange multiplier λ_{solv}:

$$\lambda_C\left(N_C+\sum_{n=1}^{\infty}\sum_{m=\delta_{n1}}^{\infty}nN_{n,m}-N_{crys}^{0}\right)=0 \tag{6.5}$$

$$\lambda_S\left(N_S+\sum_{n=1}^{\infty}\sum_{m=\delta_{n1}}^{\infty}mN_{n,m}-N_{surf}^{0}\right)=0 \tag{6.6}$$

$$\lambda_{solv}\left(N_{solv}+\sum_{n=1}^{\infty}\sum_{m=\delta_{n1}}^{\infty}N_{n,m}\int_{V_{surf}(n)}d\vec{r}\,\frac{1}{v_s}\phi_s(\vec{r}:n,m)-N_{solvent}^{0}\right)=0 \tag{6.7}$$

Finally, a standard assumption of SCMF is employed in which the volume $V_{n,m}$ is declared everywhere incompressible. Since $V_{n,m}$ comprising only solvent and surfactant tail-monomer, this constraint links $\rho(\mathbf{r})$, and thus $P_g(\alpha: n,m)$, with $\phi_s(\mathbf{r})$. The declaration of an incompressible $V_{n,m}$ actually yields an ensemble of constraints, because for each n,m-sized nanocrystal, any volume element $d\mathbf{r}$ in $V_{n,m}$ must be exactly filled by solvent molecules (of volume v_s) plus tail-monomers (of volume v_P) at every point $\mathbf{r}$ in $V_{n,m}$:

$$\forall\vec{r}\in V_{n,m}\qquad\qquad m\sum_{\alpha}P_g(\alpha:n,m)n_g(\vec{r},\alpha)v_P+\phi_s(\vec{r})=1$$

Because this constraint is a function, the Lagrange multipliers for it must also be functions, represented by the set $N_{n,m}\beta\pi_{n,m}(\mathbf{r})$. These functions are different and independent for each *n,m* nanocrystal, and they are convolved with the incompressibility constraint to yield:

$$N_{n,m}\int_{V_{n,m}} d\vec{r}\,\beta\pi_{n,m}(\vec{r})\left(m\sum_{\alpha}P(\alpha:n,m)n(\vec{r},\alpha)v_P+\phi_s(\vec{r})-1\right)=0 \tag{6.8}$$

We combine all Eqs. (6.2-6.8) to obtain the following free energy functional of the system:

$$\begin{aligned}\frac{G}{kT} &= N_C\ln N_C + N_S\ln N_S + N_S\sum_{\{\eta\}}P_f(\eta)\left[\ln P_f(\eta)+\beta u_{\text{int}}(\eta)\right]+N_{solv}\ln N_{solv}+\sum_{n=1}^{\infty}\sum_{m=\delta_{n1}}^{\infty}N_{n,m}\ln N_{n,m}\\
&-\left(N_C+N_S+N_{solv}+\sum_{n=1}^{\infty}\sum_{m=\delta_{n1}}^{\infty}N_{n,m}\right)\ln\left(N_C+N_S+N_{solv}+\sum_{n=1}^{\infty}\sum_{m=\delta_{n1}}^{\infty}N_{n,m}\right)\\
&+\sum_{n=1}^{\infty}\sum_{m=\delta_{n1}}^{\infty}N_{n,m}\left\{\begin{array}{l} n\beta g_{crys}+4\pi\left(\frac{3vn}{4\pi}\right)^{2/3}\beta\gamma+m\beta\varepsilon_{graft}\\ +m\sum_{\{\alpha\}}P_g(\alpha:n,m)\left[\ln P_g(\alpha:n,m)+\beta u_{\text{int}}(\alpha)\right]+\int_{V_{n,m}}d\vec{r}\,\frac{1}{v_s}\phi_s(\vec{r}:n,m)\ln(\phi_s(\vec{r}:n,m))\\ +\frac{\beta\omega_{TT}}{2}\iint_{V_{n,m}}d\vec{r}\,d\vec{r}'\left[m\sum_{\{\alpha\}}P_g(\alpha:n,m)n_g(\vec{r},\alpha)\right]X(\vec{r},\vec{r}')\left[m\sum_{\{\alpha'\}}P_g(\alpha':n,m)n_g(\vec{r}',\alpha')\right]\end{array}\right\}\\
&+\lambda_C\left(N_C+\sum_{n=1}^{\infty}\sum_{m=\delta_{n1}}^{\infty}nN_{n,m}-N^0_{crys}\right)\\
&+\lambda_S\left(N_S+\sum_{n=1}^{\infty}\sum_{m=\delta_{n1}}^{\infty}mN_{n,m}-N^0_{surf}\right)\\
&+\lambda_{solv}\left(N_{solv}+\sum_{n=1}^{\infty}\sum_{m=\delta_{n1}}^{\infty}N_{n,m}\int_{V_{n,m}}d\vec{r}\,\frac{1}{v_s}\phi_s(\vec{r}:n,m)-N^0_{solvent}\right)\\
&+N_{n,m}\int_{V_{n,m}}d\vec{r}\,\beta\pi_{n,m}(\vec{r})\left(m\sum_{\{\alpha\}}P_g(\alpha:n,m)n_g(\vec{r},\alpha)v_P+\phi_s(\vec{r}:n,m)-1\right)\end{aligned} \tag{6.9}$$

This expression for the free energy can now be minimized with respect to all state variables – N_C, N_S, N_{solv}, all values $\{N_{n,m}\}$, all distributions $P(\alpha:n,m)$ and $P_S(\gamma)$, and all functions $\phi_s(\mathbf{r}:n,m)$ –

by differentiating Eq. (6.9) by each state variable and setting the resultant expression to zero. By this algorithm, we find that the mass balance Lagrange multipliers, λ_C, λ_S, and λ_{solv} are simply the species' translational entropies $-\ln N_C$, $-\ln N_S$, and $-\ln N_{solv}$. Then the probability distribution of dissolved surfactants is defined:

$$P_f(\eta) = \frac{1}{q_f} e^{-\beta u_{\text{int}}(\eta)} = \frac{e^{-\beta u_{\text{int}}(\eta)}}{\sum_{\{\eta\}} e^{-\beta u_{\text{int}}(\eta)}} \tag{6.10}$$

where q_f is the partition function of dissolved surfactants.[134] The closely related probability distribution of grafted chains $\{\alpha\}$ in any *n,m*-nanocrystal is:

$$P_g(\alpha : n,m) = \frac{1}{q_g} \exp\left\{ \begin{array}{l} -\beta u_{\text{int}}(\alpha) + \int_{V_{n,m}} d\vec{r} \ln\left(\frac{\phi_s(\vec{r} : n,m)}{N_{solv}/N_{total}} \right) n_g(\vec{r},\alpha) \frac{v_P}{v_s} \\ -\frac{\beta\omega_{TT}}{2} \iint_{V_{n,m}} d\vec{r} d\vec{r}\,' X(\vec{r},\vec{r}\,') \left[\rho_g(\vec{r}\,') n_g(\vec{r},\alpha) + \rho_g(\vec{r}) n_g(\vec{r}\,',\alpha) \right] \end{array} \right\} \tag{6.11}$$

where $q_g(n,m)$ is the partition function of grafted surfactants on an *n,m*-nanocrystal. Using these definitions, the population distribution of all *n,m*-nanocrystals in our system is calculated:

$$\frac{N_{n,m}}{N_{total}} = \left(\frac{N_C}{N_{total}} \right)^n \left(\frac{N_S}{N_{total}} \right)^m \times \exp\left(-\left\{ \begin{array}{l} n\beta g_{crys} + 4\pi \left(\frac{3vn}{4\pi} \right)^{2/3} \beta\gamma + m\beta\varepsilon_{graft} \\ + m \sum_{\{\alpha\}} P_g(\alpha : n,m) \left[\ln P_g(\alpha : n,m) + \beta u_{\text{int}}(\alpha) \right] \\ + \frac{\beta\omega_{TT}}{2} \iint_{V_{n,m}} d\vec{r} d\vec{r}\,' \left[m \sum_{\{\alpha\}} P_g(\alpha : n,m) n_g(\vec{r},\alpha) \right] X(\vec{r},\vec{r}\,') \left[m \sum_{\{\alpha'\}} P_g(\alpha' : n,m) n_g(\vec{r}\,',\alpha') \right] \\ + \int_{V_{n,m}} d\vec{r} \frac{1}{v_s} \phi_s(\vec{r} : n,m) \ln(\phi_s(\vec{r} : n,m)) \end{array} \right\} \right) \tag{6.12}$$

Note that many of the terms in the exponential are due exclusively to SCMF calculations. These quantities will be addressed later individually, but for convenience let us lump them into a single term $F_{n,m}$. We also note that while N_{total} may not be constant, we can reduce the variables N_C, N_S, N_{solv}, and $N_{n,m}$ into mole fractions X_C, X_S, X_{solv}, and $X_{n,m}$. Then Eq. (6.12) is combined with the three material balances to yield the following four governing equations of our model:

$$X_{n,m} = X_C^{\,n} X_S^{\,m} X_{solv}^{\frac{V_{n,m}}{v_s} - m\frac{lv_P}{v_s}} \exp\left(-\left\{ n\beta g_{crys} + 4\pi\left(\frac{3vn}{4\pi}\right)^{2/3}\beta\gamma + m\beta\varepsilon_{graft} + \beta F_{n,m} \right\}\right) \quad (6.13a)$$

$$\sum_{n=1}^{\infty}\sum_{m=0}^{\infty} nX_{n,m} + X_C = X_{crys} \quad (6.13b)$$

$$\sum_{n=1}^{\infty}\sum_{m=0}^{\infty} mX_{n,m} + X_S = X_{surf} \quad (6.13c)$$

$$\sum_{n=1}^{\infty}\sum_{m=0}^{\infty}\left(\frac{V_{nm} - mlv_P}{v_s}\right)X_{n,m} + X_{solv} = X_{solvent} \quad (6.13d)$$

The variables X_C, X_S, and X_{solv} enter Eq. (13a) to determine the equilibrium population $\{X_{n,m}\}$, which must self-consistently obey the mass balances given by equations (13b-d). The equilibrium nanocrystal given by (n_{eq},m_{eq}) occurs at a local maximum in $X_{n,m}$. Naturally n_{eq} and m_{eq} depend on parameters given to system, such as γ, ε_{graft}, etc. Discovering these dependencies will grant crucial insight into what mechanisms are responsible for digestive ripening.

6.3 ANALYSIS OF THE MODEL THROUGH SIMPLIFICATIONS

The system of equations (13a-d) must be solved self-consistently to determine the exact behavior of $X_{n,m}$. Such a solution is intractable in general, but we can make some useful approximations and manipulate the equations mathematically to determine the relevant physics behind digestive ripening. We begin with the principle that equilibrium-sized nanocrystals will have n_{eq} crystal atoms and m_{eq} surfactants, which indicates that $X_{n,m}$ will have a local maximum at n_{eq},m_{eq}. Therefore, $-\ln X_{n,m}$ must be a minimum with respect to both n and m at the point n_{eq},m_{eq}.

At this point, we employ a change of variables from the statistical quantities n and m to the geometric quantities R (nanocrystal radius in nm) and σ (grafting density of surfactant in chains/nm^2), such that $n = 4\pi R^3/3v_C$ and $m = 4\pi R^2\sigma$ with v_C volume of a crystal monomer. Further to the change in variables, we make two new assumptions: (1) the nanocrystals are very dilute (μM) and thus X_{solv} and all its powers are nearly unity, and (2) the interfacial energy γ and the grafting energy between surfactant and crystal ε are invariant with radius or grafting density. Finally, we take the negative logarithm of Eq. (13a) and restate it as $-\ln X_{nm}$:

$$-\ln X_{n,m} = \frac{4\pi R^3}{3v_C}\left(\beta g_{crys} - \ln X_C\right) + 4\pi R^2\left(\beta\gamma + \sigma\beta\varepsilon_{graft} - \sigma \ln X_S + \beta f_{nm}\right) \tag{6.14}$$

The free energy (per unit area) calculated by SCMF theory, βf_{nm}, includes all the interactions among the surfactants' tail groups and the solvent, including tail-tail attractions, excluded volume interactions, and the configurational entropy of the solvent-surfactant mixture. There always exists a finite $\sigma_{\max}$ which represents complete coverage of the core. This surfactant-filling state

excludes all solvent molecules and dramatically limits the possible conformations of the surfactant tails, thus the entropic loss is divergently unfavorable ($\beta f_{nm} \to \infty$ as $\sigma \to \sigma_{\max}$).

The σ-derivative of Eq. (6.14) is equal to zero for the equilibrium nanocrystal to develop a relation for the equilibrium value of σ_{eq}:

$$\left(\frac{\partial - \ln X_{n,m}}{\partial \sigma} \right)_{eq} = 4\pi R_{eq}^2 \left(\beta \varepsilon_{graft} - \ln X_S + \frac{\partial \beta f_{n,m}}{\partial \sigma} \right) = 0 \qquad (6.15)$$

The results of Eq. (6.15) are different depending on the availability of surfactant. If there is enough surfactant in solution to coat the nanocrystal as needed, then any favorable grafting energy $\varepsilon < 0$ will bring surfactants out of solution and tether them to the nanocrystal surface. The conformational entropy decreases as σ increases, thus there exists an equilibrium grafting density for every radius, $\sigma_{eq}(R)$, which optimizes the grafting energy against the loss of conformational entropy. On the other hand, if the surfactant concentration is limited, then the translational entropy loss $-\ln X_S$ becomes significant at smaller σ than optimal. In that surfactant-lean condition, $\sigma_{eq}(R)$ is such that the ratio of crystal monomers ($4\pi R^3/3v_C$) to surfactants ($4\pi R^2 \sigma$) in a single nanocrystal is equivalent to the global molar ratio, such that $X_{crys}/X_{surf} = R_{eq}/3v_C\sigma_{eq}$.

We may insert the function $\sigma_{eq}(R)$ back into Eq. (6.14) and take the R-derivative. By setting it to zero, we define the equilibrium radius R_{eq}, the primary goal of this study:

$$\left.\frac{\partial - \ln X_{n,m}}{\partial R}\right|_{eq} = \frac{4\pi R_{eq}^2}{v_C}\left(\beta g_{crys} - \ln X_C\right) + 8\pi R_{eq}\left(\beta\gamma + \sigma_{eq}\beta\varepsilon_{graft} - \sigma_{eq}\ln X_S + \beta f_{nm}\right)$$
$$+4\pi R_{eq}^2\left[\frac{d\sigma_{eq}}{dR}\left(\beta\varepsilon_{graft} - \ln X_S\right) + \frac{\partial\beta f_{n,m}}{\partial R}\right] = 0 \qquad (6.16)$$

When there are enough surfactant molecules to graft to all the R_{eq}-sized nanocrystals optimally, then $d\sigma_{eq}/dR$ is negligible and does not control the equilibrium size. If, however, surfactant is present in insufficient quantities for a given value of R_{eq}, then $d\sigma_{eq}/dR$ at R_{eq} becomes strongly positive and has an influence on the equilibrium size.

Meanwhile, βf_{nm} depends on the core radius R in an unknown and difficult to interrogate manner. To obtain quantitative relations for R_{eq}, we therefore examine two limiting cases: either the free energy of the crystal core dominates and βf_{nm} and its R-derivative are neglected, or the free energy of the surfactant tails dominates and ($g_{crys} - \ln X_C$) is neglected.

6.4 THE CRYSTAL-DOMINANT MODEL

In the special case where the R-dependence of βf_{nm} is considered negligible, we can reduce Eq. (6.16) to obtain the following definition of the equilibrium radius R_{eq}. In this derivative, we employ a new quantity γ_{eff}:

$$\gamma_{eff} = \beta\gamma + \sigma_{eq}\left(\beta\varepsilon_{graft} - \ln X_S\right) \qquad (6.17)$$

and the result for the equilibrium radius is therefore:

$$R_{eq} = \frac{2\gamma_{eff} v_C}{kT \ln X_C - g_{crys} + v_C \frac{d\sigma_{eq}}{dR}\left(\varepsilon_{graft} - kT \ln X_S\right)} \tag{6.18}$$

It is necessary to note the following: if no surfactant is present and $\sigma_{eq} = 0$ identically, then Eq. (6.18) becomes essentially the definition given by LSW theory of the "critical" radius R_c for Ostwald ripening.[54-56] This will be discussed further below. The second derivative of $-\ln X_{nm}$ establishes whether R_{eq} in Eq. (6.18) is a minimum of $-\ln X_{nm}$ or a maximum, stable or unstable. The second derivative of Eq. (6.14) is combined with Eq. (6.18) to obtain the following:

$$\left.\frac{\partial^2 - \ln X_{n,m}}{\partial R^2}\right|_{eq} = -8\pi\left[\gamma_{eff} + R_{eq} \frac{d\sigma_{eq}}{dR}\left(\beta\varepsilon_{graft} - \ln X_S\right)\right] \tag{6.19}$$

In the surfactant-excess case where $d\sigma_{eq}/dR$ is negligible, the effective surface energy γ_{eff} exclusively determines whether R_{eq} is a thermodynamically stable radius or not. Namely, R_{eq} is unstable for any $\gamma_{eff} > 0$, i.e. when surface is net unfavorable. In this condition Eq. (6.18) becomes *exactly* the definition of the critical radius R_c in the LSW theory of Ostwald ripening, in which R_c represents the *least* thermodynamically favored radius.[54-56] This is why small nanocrystals will shrink away from R_c, while larger nanocrystals grow away from R_c. Thus, Ostwald ripening will occur for any $\gamma_{eff} > 0$, even when surfactant is present in excess. LSW theory further states that the Ostwald ripening rate depends on γ_{eff}, therefore *weakly grafted surfactants will slow Ostwald ripening, but cannot prevent it*. In this manner, equation (6.18) and (6.19) represent Ostwald ripening of bare nanocrystals and of weakly-bound surfactants. The

crystal-dominant version of our model thus successfully reproduces the critical experimental results (I) and (II).

According to Eq. (6.19), a stable nanocrystal radius can only exist under the condition $\gamma_{eff} < 0$, i.e. when surfactant mediation makes the nanocrystal surface *net favorable*. Another physical interpretation of $\gamma_{eff} < 0$ is that the crystal-surfactant bond is more favorable than the crystal-crystal bond. Meanwhile, $d\sigma_{eq}/dR$ is either negligible in the excess surfactant case or positive in the surfactant lean case, thus $\gamma_{eff} < 0$ is a universal condition for stability of R_{eq} in this crystal-dominant thermodynamic model. Combining Eq. (6.18) and Eq. (6.14) reveals the value of X_{nm} at R_{eq}, σ_{eq}, with a surprising result:

$$-\ln X_{n,m}\Big|_{eq} = \frac{4\pi R_{eq}^2}{3}\left[\beta\gamma_{eff} + v_C \frac{d\sigma_{eq}}{dR}\left(\beta\varepsilon_{graft} - \ln X_S\right)\right] \tag{6.20}$$

If $d\sigma_{eq}/dR$ is negligible (the excess-surfactant condition), then Eq. (6.19) and Eq. (6.20) imply that $X_{nm}|_{eq} > 1$ for any $R_{eq} > 0$ whenever $\gamma_{eff} < 0$. Therefore, when surfactant is present in excess, any finite value of a stable R_{eq} will violate the mass balance given in Eq. (6.13b) and be thermodynamically inaccessible. The physical interpretation is more intuitive: a finite-size nanocrystal with $\gamma_{eff} < 0$ will shrink to maximize the amount of thermodynamically favorable surface. The nanocrystal will therefore shrink until the mass balance is obeyed, which is to say its radius will decrease until either (a) $d\sigma_{eq}/dR$ becomes positive and significant or (b) until all crystal-crystal bonds have been replaced by crystal-surfactant bonds. $d\sigma_{eq}/dR$ only becomes positive when insufficient surfactant remains to maintain σ_{eq}, leading to stable nanocrystals in

the surfactant-lean condition. This represents the critical experimental result (III). Meanwhile, the case where all crystal-crystal bonds are replaced by crystal-surfactant bonds represents the molecular cluster, which is the critical experimental result (IV).

By assuming the free energy is dominated by the crystal core, our thermodynamic model is capable of reproducing four critical behaviors of nanocrystal synthesis: (I), (II) Ostwald ripening of nanocrystals with no surfactant or weakly bound surfactant, (III) the formation of stable nanocrystals under surfactant-lean conditions, and (IV) the formation of molecular clusters.

Most importantly, the crystal-dominant thermodynamic model explicitly disproved the hypothesis that grafting energy and crystal core free energy can complete to yield a thermodynamically stable nanocrystal in the presence of excess surfactant.[133] In the case where crystal core dominates the free energy, excess surfactant always either leads to Ostwald ripening for $\gamma_{eff} > 0$ or to molecular clusters for $\gamma_{eff} < 0$. No middle-ground exists. Either crystal-crystal bonds or the crystal-surfactant bonds are more energetically favorable, and without other constraints the system will evolve to maximize the more favorable bond.

6.5 THE SURFACTANT-DOMINANT MODEL

We now explore the case where the surfactant free energy dominates the thermodynamics of the nanocrystal. This is inspired by the existence of stable microemulsions: mixtures of water, oil, and a surfactant form "swollen micelles" where a spherical core of the solvent is surrounded by a monolayer of surfactant, which mediates the core-solvent interaction.[132] The swollen micelle size is stable and monodisperse, and microemulsion formation is spontaneous upon surfactant

addition. Such systems represent the critical experimental result (V) given above. To be considered complete, the thermodynamic model given in Eq. (6.13) must theoretically reproduce these stable swollen micelles. Once such a stable state has been determined, the limits of stability can be assessed to determine whether microemulsions and gold-thiolate nanocrystals are formed by the same mechanism.

To study a swollen micelle, let the surfactant free energy βf_{nm} be dominant, yielding the following simplified thermodynamic model:

$$-\ln X_{n,m} = 4\pi R^2 \left(\beta\gamma + \sigma\beta\varepsilon_{graft} - \sigma \ln X_S + \beta f_{nm}\right) \tag{6.21}$$

with its first derivatives set to zero at the equilibrium size R_{eq}, σ_{eq}:

$$\frac{\partial - \ln X_{n,m}}{\partial R} = 8\pi R_{eq}\left(\beta\gamma + \sigma\beta\varepsilon_{graft} - \sigma \ln X_S + \beta f_{nm}\Big|_{eq}\right) + 4\pi R_{eq}^2 \frac{\partial \beta f_{nm}}{\partial R}\Bigg|_{eq} = 0 \tag{6.22}$$

Figure 6.2: The left-hand side of Eq. (6.24) and the plane where the function is zero. The intersection of the blue surface and the white plane yeilds the viable equilibrium pairs (R_{eq}, σ_{eq}).

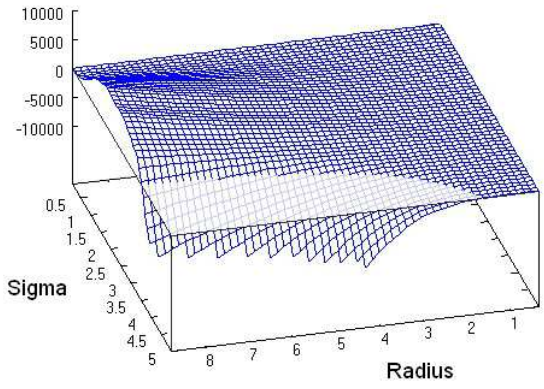

$$\frac{\partial - \ln X_{n,m}}{\partial \sigma} = 4\pi R_{eq}^2 \left(\beta\varepsilon_{graft} - \ln X_S + \frac{\partial \beta f_{nm}}{\partial \sigma}\Bigg|_{eq}\right) = 0 \tag{6.23}$$

Combining equations (6.22) and (6.23) eliminates the grafting energy ε_{graft} and the dissolved surfactant entropy $\ln X_S$, expressing the

equilibrium condition only in terms of the surfactants' intermolecular interactions and the core-solvent interfacial energy γ:

$$\beta f_{nm}\Big|_{eq} + \frac{R_{eq}}{2}\frac{\partial \beta f_{nm}}{\partial R}\Big|_{eq} - \sigma \frac{\partial \beta f_{nm}}{\partial \sigma}\Big|_{eq} + \beta\gamma = 0 \qquad (6.24)$$

Eq. (6.24) defines a curve of points (R_{eq},σ_{eq}) which represent all the possible equilibrium sizes and grafting densities of swollen micelles. Depending on the total amount of surfactant available, the equilibrium values R_{eq} and σ_{eq} will vary along this curve. This is equivalent to the definition of $\sigma_{eq}(R)$ in the crystal-dominant model, but due to self-assembly instead of surface grafting.

As was the case for the crystal-dominant model, one further constraint on the system is that the mole fraction $X_{nm}|_{eq} < 1$. Using Eq. (6.21) and (6.22), we may restate $-\ln X_{nm}$ such that it depends only on the surfactant free energy βf_{nm} through the following equality:

$$-\ln X_{n,m}\Big|_{eq} = -2\pi R_{eq}^3 \frac{\partial \beta f_{nm}}{\partial R}\Big|_{eq} > 0 \qquad (6.25)$$

The surfactants' intermolecular interactions are defined by SCMF theory, as expressed in fully in Eq. (6.12). To investigate the trends of βf_{nm} and its derivatives, the system of equations defined by SCMF theory is solved numerically.[135] From the results, $\beta f_{nm}(R,\sigma)$ and its derivatives were calculated for various parameters, and analyzed through equations (6.21-6.25) above.

The two-dimensional surface in Eq. (6.24) was calculated, as shown graphically in Figure 6.2, and set to zero to obtain a series of pairs (R_{eq},σ_{eq}), which are plotted in Figure 6.3 for multiple values of different parameters. If swollen micelles exist at equilibrium, then their structure R,σ must lie on this curve. The curve (R_{eq},σ_{eq}) exhibits three clear trends: the equilibrium coverage σ_{eq} decreases as the equilibrium size R_{eq} increases, stronger tail-tail attractions promote larger swollen micelles, and higher values of $\beta\gamma$will slightly promote larger micelles as well. The three trends all point to the same mechanism: the surfactants can better maximize the monomer-to-monomer contacts when the core is larger. In fact, it is this mechanism which generates an equilibrium size at all, since the surfactants' intermolecular attraction will promote a larger core radius while entropy prefers smaller aggregates.

Finally, $-\ln X_{nm}|_{eq}$ is calculated with Eq. (6.25) to determine which swollen micelles obey the mass balance (where $X_{nm}|_{eq} < 1$) and to confirm that the total amount of surfactant determines the exact size (R_{eq},σ_{eq}) of the swollen micelle at equilibrium. The value of $-\ln X_{nm}|_{eq}$ is plotted versus R_{eq} and σ_{eq} for several values of $\beta\gamma$for $\omega_{TT} = -6kT$ in Figure 6.4. (The "hump" is a side effect of discretization in the SCMF framework, as discussed in Appendix E.) The largest microemulsions always yield $-\ln X_{nm}|_{eq} < 0$ (thus $X_{nm}|_{eq} > 1$), but for small $\beta\gamma$there is always a range of (R_{eq},σ_{eq}) that are physically viable for equilibrium swollen micelles. The value of $-\ln X_{nm}|_{eq}$ will be the one that obeys the mass balance, and more positive values of $-\ln X_{nm}|_{eq}$ imply that lower surfactant concentrations X_{surf} are able to self-assemble into a finite number of swollen micelles.

The breadth of this range of viable sizes, however, tends to shrink as $\beta\gamma$increases: the unfavorable core-solvent interface competes with the tail-tail attractions of the surfactant, and

tail-tail attractions of a particular magnitude ω_{TT} are only able to overcome certain values of $\beta\gamma$ to yield $-\ln X_{nm}|_{eq} > 0$, as shown in Figure 6.4. The maximum surface energy that permits any thermodynamically stable micelle is defined as the "critical surface energy" $\beta\gamma_{crit}$: for any $\beta\gamma > \beta\gamma_{crit,}$ the core-solvent interface is so unfavorable that no self-assembled structure of the surfactants can yield an equilibrium micelle. Furthermore, as $\beta\gamma$ approached $\beta\gamma_{crit}$, the possible values of $X_{nm}|_{eq}$ are larger, meaning that the solution must contain a larger concentration of surfactants before they will self-assemble. If no equilibrium micelle is formed, the result is Ostwald ripening of the cores. The threshold energy $\beta\gamma_{crit}$ can be estimated from the numerical results of the SCMF data, as plotted in Figure 6.5. It appears that $\beta\gamma_{crit}$ increases with ω_{TT} approximately linearly, though there is a high degree of error.

To support the numerical results and confirm the overall trend of $\beta\gamma_{crit}$ increasing with ω_{TT}, an order-of-magnitude simplification of Eq. (26) is employed using the governing equations of SCMF theory. While the details are in Appendix E, we say that the surfactant attractions are incredibly strong and they form a pure layer around the solute core. Thus, $\phi_s \approx 0$ near the core, $\phi_s \approx 1$ everywhere else, and Eq. (26) simplifies to the following approximation which includes the chain length L:

$$\beta\gamma_{crit} \propto -\sigma_{\max}\left(L\beta\omega_{TT}\right) \tag{6.26}$$

Because σ cannot be arbitrarily high, the number of surfactant tail monomer-monomer contacts cannot be increased beyond that of a particular optimal structure. Therefore, the optimal structure

maximizes the effect of ω_{TT} such that it overcomes the greatest possible range of surface energies, $\beta\gamma$. The largest such surface energy is thus $\beta\gamma_{crit}$.

Figure 6.3: Pairs of (R_{eq},σ_{eq}) as calculated from Eq. (6.24), shown for (a) various values of ω_{TT}, (b) various chain lengths L, and (c) various surface energies $\beta\gamma$. The broader lines in (c) show the physically viable range of (R_{eq},σ_{eq}) values as per Eq. (6.25). See Figure 6.4.

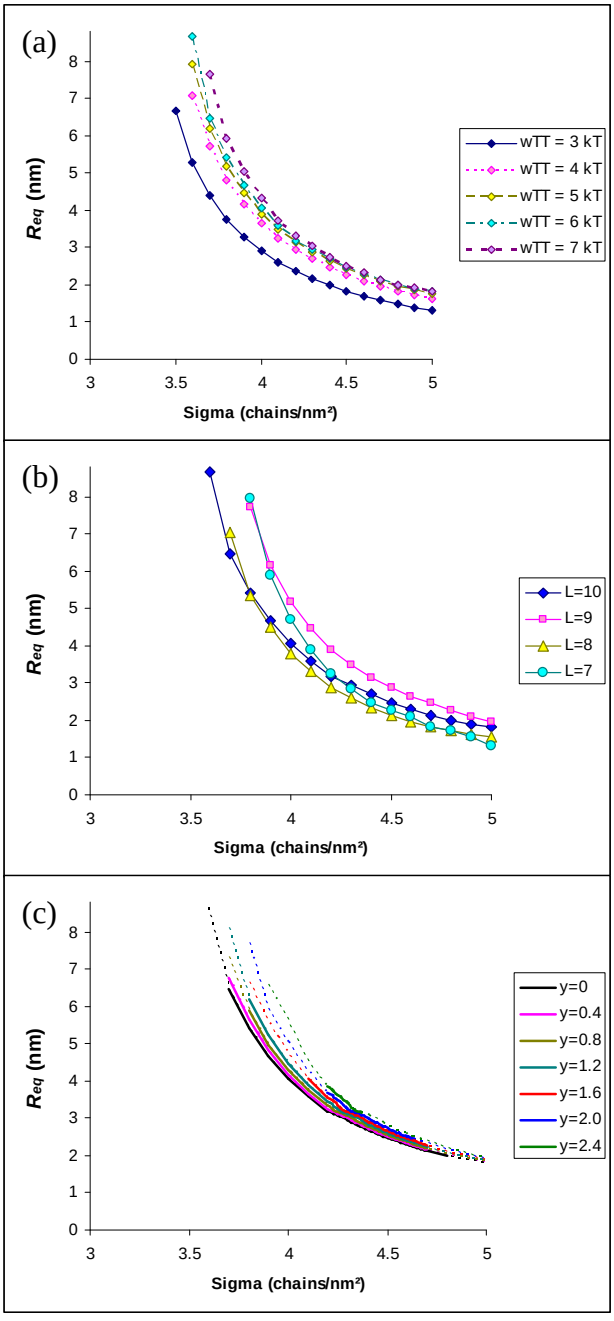

Furthermore, that optimal structure represents a particular pair $(R_{eq},\sigma_{eq})^*$ around which the swollen micelles are likely to be distributed. As is the case for ordinary micelles, the size distribution of swollen micelles will only be a perturbation away from $(R_{eq},\sigma_{eq})^*$ for various other physical parameters of the system. As shown in Figure 6.4, the viable range of swollen micelle sizes varies about $(R_{eq},\sigma_{eq})^*$, with more freedom as $\beta\gamma$ decreases.

Figure 6.4: $-\ln X_{nm|eq}$ as calculated in Eq. (6.25). As $\beta\gamma$ increases, the range of viable values of $X_{nm|eq}$ shrinks. For some $\beta\gamma_{crit}$, no viable values of $X_{nm|eq}$ can be obtained.

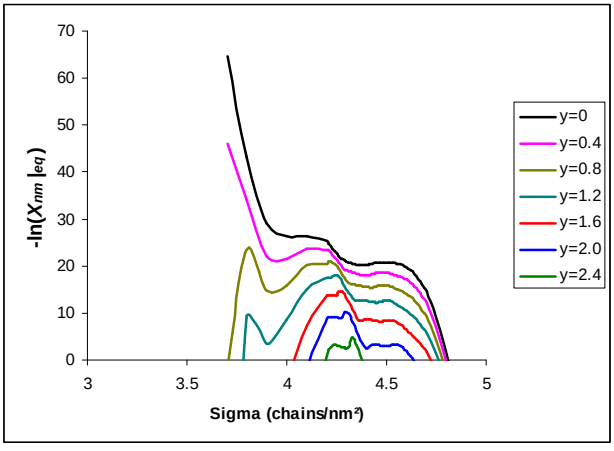

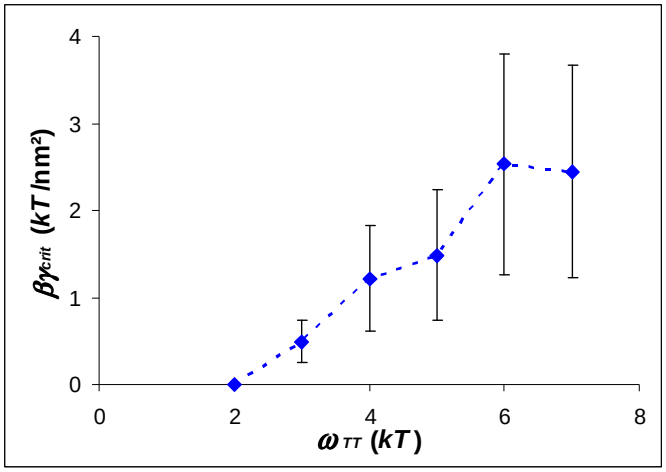

Figure 6.5: Plot of estimated values of $\beta\gamma_{crit}$ vs. ω_{TT}. The error bars represent uncertainty in the calculation due to the discretization of the SCMF model.

The literature estimate for the surface energy of gold nanocrystals in vacuum is about 1 J/m^2 = 100-200 kT/nm^2 at typical experimental temperatures.[136] Although the data in Figure 6.5 is highly imprecise, it suffices to say that the ω_{TT} value must be large, of order 10-100 kT to stabilize a nanocrystal with $\beta\gamma \sim 100\ kT/\text{nm}^2 < \beta\gamma_{crit}$.

6.6 DISCUSSION AND COMPARISON WITH EXPERIMENTS

Between equations (6.18-6.20) and (6.24-6.26), we have shown that our thermodynamic model, expressed in its most general form in Eq. (6.13), can properly predict the five critical types of behavior witness in surfactant-mediated systems, namely (I) Ostwald ripening of nanocrystals with no surfactant, (II) Ostwald ripening of nanocrystals with a weakly-bound surfactant, (III) formation of stable nanocrystals with a strongly-binding surfactant, but present in limited amounts, (IV) formation of molecular clusters with a strongly-binding surfactant, present in excess, and (V) stable microemulsions. The division between stable and unstable nanostructures can be described in the following way:

(A) A dominant, unfavorable surface energy $\beta\gamma > 0$ always causes Ostwald ripening.

(B) If surfactant grafting outweighs $\beta\gamma$, the final size maximizes surfactant-core contacts.

(C) If surfactant cohesion outweighs $\beta\gamma$, the surfactants self-assemble into a microemulsion.

These are the three possible scenarios offered by our thermodynamic model. This suggests that gold-thiol nanocrystals as produced by digestive ripening can only be thermodynamically stable if (a) the surfactant-to-crystal ratio is too small to permit further digestion or (b) if the thiols are forming a microemulsion around the (relatively) weak gold core. Let us examine the second condition through the details of our model.

In a microemulsion, the spontaneous formation of swollen micelles is caused only by the mixing of the three components, solute, solvent, and surfactant. This matches qualitatively with the process of digestive ripening of gold-thiolate nanocrystals in excess surfactant, where the simple addition of thiol causes large, polydisperse nanocrystals to spontaneously shrink to small, monodisperse nanocrystals. We must compare the quantitative conclusions of our model against known experimental trends of digestive ripening. Already, Figure 6.5 illustrates that ω_{TT} would have to be very high to overcome the large surface energy of a nanocrystal, but between the error in $\beta\gamma_{crit}$ and the experimental difficulty in determining $\beta\gamma$ for a solid, this comparison alone is insufficient to evaluate whether digestive ripening behaves like a microemulsion. We therefore compare our conclusions in Eq. (6.24) with experimental trends of digestive ripened nanocrystals and we require that the model must reproduce three primary trends:

(Trend 1) The final size and polydispersity do not vary significantly with the chain length. Digestive ripening of gold nanocrystals with octanethiol, decanethiol, and dodecanethiol thiol yielded almost identical nanocrystals (within measurement error) that were 4.7 ± 0.4 nm. The same protocol with hexadecanethiol produced 5.5 ± 0.4 nm nanocrystals.[45]

(Trend 2) Size and polydispersity vary strongly with the choice of head group. Digestive ripening using dodecyl amine yielded much larger, much more polydisperse nanocrystals at 8.6 ± 1.3 nm; using octadecyl silane produced 7.2 ± 1.0 nm nanocrystals; and using trioctyl phosphine produced 7.2 ± 1.1 nm nanocrystals.[46]

(Trend 3) Gold, silver, and palladium nanocrystals were synthesized by digestive ripening with both dodecanethiol and dodecyl amine as surfactant. The final sizes for the silver, gold, and palladium nanocrystals were 4.4 ± 0.6 nm, 5.2 ± 0.5 nm, and 6.2 ± 0.5 nm respectively with thiol surfactant, and were 10.2 ± 1.2 nm, 8.0 ± 0.6 nm, and 7.1 ± 0.6 nm for amine surfactant. We note especially that the trend of sizes $R_{\mathrm{AgSR}} < R_{\mathrm{AuSR}} < R_{\mathrm{PdSR}}$ for dodecanethiol is *opposite* the size trend for dodecyl amine surfactant, $R_{\mathrm{AgNR}} > R_{\mathrm{AuNR}} > R_{\mathrm{PdNR}}$.[47]

In the surfactant-dominant case, the possible pairs (R_{eq}, σ_{eq}) are determined by Eq. (6.24) and Eq. (6.25) reveals which pairs are physically viable. Eq. (6.24) clearly indicates that R_{eq} and σ_{eq} only depend on the surfactants' intermolecular interactions βf_{nm} and the core-solvent surface energy $\beta\gamma$. They do not depend explicitly on grafting energy ε_{graft}. The polydispersity, too, is controlled exclusively by βf_{nm} and $\beta\gamma$. This fails to explain Trend 2, the observation that the head group strongly affects the nanocrystal size. While it is possible that the different surfactants could alter the solvent enough to change $\beta\gamma$, it is not likely since the solution is only about 7% surfactant by volume. Even Trend 3 does not strictly obey Eq. (6.24). Dodecyl amine and dodecyl thiol have identical tail groups and should have very similar profiles for βf_{nm}, and the choice of amine vs. thiol shoud have no effect on $\beta\gamma$. As a result, there is no immediately explanation for the reversed trend in sizes, $R_{\mathrm{AgSR}} < R_{\mathrm{AuSR}} < R_{\mathrm{PdSR}}$ for thiols versus $R_{\mathrm{AgNR}} > R_{\mathrm{AuNR}} > R_{\mathrm{PdNR}}$ for amines.

In addition to the three trends listed above, stable gold nanocrystals can also be digested further to yield gold-thiolate molecular clusters under certain conditions. This does not occur in the classic digestive ripening procedure. However, mixing 6-nm gold-thiolate nanocrystals with excess dodecanethiol in octyl ether and heating the solution to 300°C will produce Au_3SR_3 molecular clusters after 50 minutes.[92] 10-nm gold nanocrystals passivated with oleylamine (C_9=C_9NH_2) were dissolved to molecular clusters at *room temperature* by adding an aromatic thiol instead of an alkyl thiol.[94] Our SCMF calculations do not show molecular clusters to be thermodynamically stable for any choice of parameters under the surfactant-dominant model. The crystal-dominant model addresses molecular clusters, but declares that the existence of stable molecular clusters requires that the gold-thiol bond be stronger than the gold-gold bond ($\gamma_{eff} < 0$). Any assertion that digestive ripening is similar to microemulsions is thus at odds with $\gamma_{eff} < 0$ in these other conditions. It is conceivable that the grafting energy ε_{graft} is vastly different between alkanethiols and aromatic thiols, and it is possible that $\gamma_{eff} > 0$ for gold-thiolate in toluene at 100°C and simultaneously $\gamma_{eff} < 0$ for gold-thiolate in octyl ether at 300°C. However, these requirements are very stringent and unintuitive, especially in the context of Figure 6.5 which requires an incredibly strong ω_{TT} value to overcome the nanocrystal surface energy. Comparing the surfactant-dominant model with experimental data therefore reveals many weaknesses in treating digestive ripening as a process akin to microemulsion formation.

However, if the thermodynamic drive for microemulsions is not applicable to digestive ripening, then our model suggests that there is only one alternative explanation remains: that $\gamma_{eff} < 0$ and the thiolate-to-gold ratio is less than 1. This is counterintuitive given that the thiol-to-gold ratio is

30:1 in digestive ripening, but the critical difference is that while dodecane*thiol* is the species added in the procedure, dodecane*thiolate* is the species that passivates the gold nanocrystals.

Experimental data and DFT calculations have both indicated that only thiolate is bonded to the gold nanocrystal surface.[86, 89, 137] A recent study has also determined that when gold-thiolate nanocrystals are formed in acetone or butanone, hydrogen gas is evolved.[85] It is unknown if hydrogen gas is evolved in any other gold-thiolate synthesis. Furthermore, there is experimental evidence that dodecanethiol alone cannot digest gold at room temperature. Mixing dodecanethiol and bulk gold in organic solvents yields no measurable reaction at room temperature or at 250°C,[138] and even the 10-nm gold-amine nanocrystals (which spontaneously formed molecular clusters when an aromtic thiol was added) were completely inert in the presence of alkanethiols.[94] In fact, dodecanethiol is only shown to digest gold in two cases: in octyl ether at 300°C and in the original digestive ripening studies.[26, 92]

The combination of the available information — hydrogen evolution, the difference between alkanethiol and aromatic thiol, the high-temperature vs. low-temperature behavior of alkanethiol — inspires a hypothetical explanation. It is possible that, thermodynamically, the gold-thiolate bond is always stronger than the gold-gold bond, but there is a chemical kinetic energy barrier of hydrogen loss which governs whether or not a surfactant will digest gold crystal. The authors of the aromatic-thiol molecular cluster synthesis state that aromatic thiols can more easily donate the hydrogen because the unfavorable formation of any net charge can be stabilized by resonance in the aromatic rings.[94] It is also natural to believe that alkanethiol molecules could more

easily lose hydrogen at high temperatures in a polar solvent (octyl ether) than at moderate temperatures when dissolved in toluene or another hydrocarbon.

Unfortunately, though this hypothesis is pleasingly simple, there is no experimental evidence for it or against it in the digestive ripening process. Among thousands of publications regarding the synthesis of gold nanocrystals, very few published works interrogate any exact chemical processes, and no global trends across publications can be established because the protocols are so heterogeneous among different experiments. It is therefore necessary to perform more experiments in order to properly assess which theory, the microemulsions treatment or the hindered thiolate formation, correctly describes why digestive ripening occurs.

We propose three simple series of experiments that will provide definitive proof that one of these treatments is correct. The first series should reproduce the original digestive ripening synthesis, which dissolved 34 mg of $AuCl_3$ in 10 mL toluene, with different reagent concentrations by dissolving the same 34 mg of $AuCl_3$ and the same masses of other reagents in 20 mL, 40 mL, 80 mL, and 160 mL of toluene. (This will reduce the total mole fraction of surfactant, X_{surf}, but the thiol-to-gold ratio, X_{surf}/X_{crys}, will be maintained.) According to Eq. (6.25) and Figure 6.4, the equilibrium size will shift until X_{nm} is the right magnitude that X_{surf} total surfactant is at equilibrium: for small-to-moderate values of $\beta\gamma$(like the black, pink, and gold curves in Figure 6.4) reducing X_{surf} will cause the equilibrium size to shrink until X_{nm} is sufficiently small; if $\beta\gamma$is large (like the blue and green curves), then the range of possible X_{nm} values becomes so limited that small changes in thiol concentration will prevent self-assembly. Therefore, diluting the reagent concentration will either give rise to measurable changes in size or, if the size is

independent of concentration, a moderately low concentration will prevent any self-assembly of stable nanocrystals.

The second and third series of experiments will extend other studies that have been conducted to investigate the effect of the thiol-to-gold ratio. These experiments should maintain the 30:1 thiol-to-gold ratio, but the DDAB-to-gold ratio and $NaBH_4$-to-gold ratio should be altered. If the final nanocrystal size in digestive ripening depends only on the interactions between metal and surfactant, then these two concentrations should have no effect on the product nanocrystals (provided DDAB still forms micelles and provided $NaBH_4$ can remove all the chlorides from $AuCl_3$). On the other hand, if the hypothesis that the thiolate formation depends on one or more of the side products and excess reagents of gold salt reduction, then the final nanocrystal size should show nearly stoichiometric dependence on one of the reagents *independently* of thiol-to-gold ratio.

6.7 CONCLUSION

We have built a general thermodynamic model and calculated the free energy of surfactant-mediated nanocrystals in solution. Examination of two limiting cases, the crystal-dominant model and the surfactant-dominant model, the theory correctly reproduces the thermodynamic driving forces (I) for Ostwald ripening of nanocrystals that are bare, (II) for Ostwald ripening of nanocrystals coated with weakly-grafted surfactants, (III) for the formation of stable nanocrystals when a strongly-binding surfactant is present in limited quantities, (IV) for the formation of molecular clusters when a strong-binding surfactant is present in excess, and (V) for the spontaneous formation of swollen micelles as in a microemulsion. The conclusions of theory

indicate that a favorable crystal volume and favorable surfactant grafting to its surface is insufficient to explain digestive ripening: when surfactant is present in excess, the result is either Ostwald ripening or molecular clusters and finite-size nanocrystals are impossible in that scheme. The only two possible thermodynamic explanations are that it is either like a microemulsion or that the production of thiolate from thiol is critically limiting the progress of digestive ripening. The microemulsion comparison requires a very high surfactant interaction ω_{IT} and predicts trends that are contracted by experimental data. Evidence, meanwhile, for the thiolate conversion hypothesis is very limited. We therefore recommend a series of experiments that, combined with our theoretical results, should determine explicitly which model is more appropriate to describing the digestive ripening process.

CHAPTER 7

CONCLUSIONS AND FUTURE DIRECTIONS

7.1 NEW THEORIES OF NANOCRYSTAL GROWTH

The goal of this thesis is to fill a void in our understanding of nanocrystal growth, a void that was inaccessible by experimental methods and impractical for numerical exploration. The insights have practical applications in an immediate sense, in that they have advanced the timeline for mass-production of nanocrystals at factory scales. The theory of size focusing explicitly relates an intensive but controllable quantity to the size and quality of product nanocrystals.[111] The supplementary theory of surfactant-coated nanocrystals allows an extra degree of further control. Finally, the theories for digestive ripening have separated two possible explanations for the process, which have elucidated what new experimental investigations of gold nanocrystals are needed to advance the technology. The theoretical conclusions derived here reveal what mysteries remain in these individual processes and what kinds of investigations are necessary in the future to approach the controlled, engineerable mass production of nanocrystals.

Combined with LSW theory, the formulations presented in this work provide a comprehensive description of spherical nanocrystal growth processes. Bare nanocrystals, surfactant-coated nanocrystals, Ostwald ripening, size focusing, digestive ripening, and the formation of molecular clusters have each been addressed. The paths for future study are still infinite, but the developments made so far suggest two very important avenues in which novel theoretical

research should be conducted in the quantitative analysis of nanocrystal growth. These two avenues are anisotropic nanocrystal growth and nanocrystal nucleation.

7.2 FUTURE DIRECTIONS: ANISOTROPIC NANOCRYSTAL GROWTH

Starting roughly in 2002, experimental studies of non-spherical nanocrystals have exploded in number because of the diverse applications of shape-controlled nanocrystals.[102] Nanorods, nanowires, nanosheets, nanocubes, nanoprisms, nano-polyhedra, and even nano-tetrapods and nano-hexapods have been synthesized reproducibly using a long list of crystal materials. Anisotropic structures are observed to possess orientation-dependent quantum properties. For example, while a spherical quantum dot has a single photoluminescent frequency, a nanorod of the same material will show two separate frequencies of photoluminescence, one from the rod's diameter and the other from its length.[139] Multipods (tetrapods, hexapods, etc.) have been explored for their electronic transport properties in technologies such as quantum computing and solar power.[140, 141] Myriad other examples exist of the technological utility of anisotropic nanocrystals.

The different techniques for synthesizing anisotropic nanocrystals are as diverse as their morphologies. A general motif is that use of more than one surfactant in a synthesis, where the different surfactants enhance or inhibit a particular facet's growth rate.[67] CdSe nanorods, for example, employ the same solvent and surfactant surfactant as spherical CdSe nanocrystals, but the inclusion of a phosphonic acid alters the CdSe surface such that growth along the *c*-axis is preferred. Gold octahedra, meanwhile, are synthesized using a diol solvent and a polar polymer, like polyvinyl pyridine or a polyol, effectively making any facet that is not the 111 face

sufficiently unfavorable as to never appear.[67] While some insights have been gained from observing experimental results, a general theory has not been developed.

A theoretical description of anisotropic nanocrystal growth is problematic when viewed through the lens of LSW theory. It is possible to develop a model for a polyhedron with a face-dependent reaction rate constant. Such a model would assist in determining what properties of the face-dependent rate constant will lead to spheres vs. prisms, etc. However, such a model would neglect the case of diffusion-limited growth. Diffusion of monomers to, from, and especially around the anisotropic nanocrystal's surface must be described quantitatively to accurately describe its growth. Herein lies the grand challenge to a theoretical description of anisotropic nanocrystals.

In the volume around any nanocrystal, the concentration profile can vary with distance r and the angles θ and ϕ. Gradients in the concentration profile in the θ and ϕ directions could be critical to determining what shape the nanocrystal grows into. Solving for the complete concentration profile, however, is greatly challenging. An elementary analytical answer is almost unobtainable. It is hypothetically possible to solve for the concentration profile around an oblate or a prolate ellipsoid, using either a complicated construct in spherical coordinates or using a dynamic-size spheroidal coordinate system. However, even in the event that such treatments would be successful, they would only address the difference in growth between spheres, rods, and discs. The framework would be unable to assess polyhedra, prisms, or multipods.

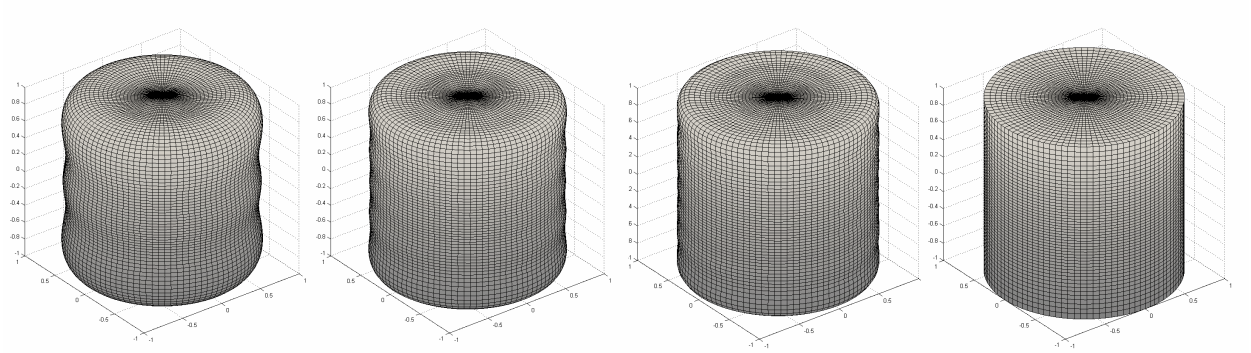

Figure 7.1: A cylinder, expressed in spherical coordinates using a Fourier spectral method as defined by Eq. (7.1), with using 3, 5, and 7 sinusoidal modes, with the exact cylinder expressed parametrically on the right.

The only framework that is general enough to incorporate the greatest number of anisotropic nanocrystal types is the use of spectral methods. Because the surface is cyclic, it is trivial to define it through sine and cosine functions, providing a general expression that models literally any surface with a one-to-one mapping. (That is, any surface with only one value of R for every direction θ,ϕ.) The boundary $R(\theta,\phi)$ of an anisotropic nanocrystal is therefore defined:

$$R(\theta,\phi)=\sum_{n=0}^{\infty}\sum_{m=0}^{\infty}R_{nm}\left[\cos(n\theta)+a_{nm}\sin(n\theta)\right]\left[\cos(n\phi)+b_{nm}\sin(n\phi)\right] \tag{7.1}$$

Because the Fourier series are orthogonal sets, one may convolve $R(\theta,\phi)$ with one of the modes, i.e. $\cos(N\theta)$, to reduce the entire sum over n to a single value at $n = N$. This method can be used, for example, to describe the surface of a cylinder as shown in Figure 7.1, where the number of modes increases the accuracy of the surface, and the convolution

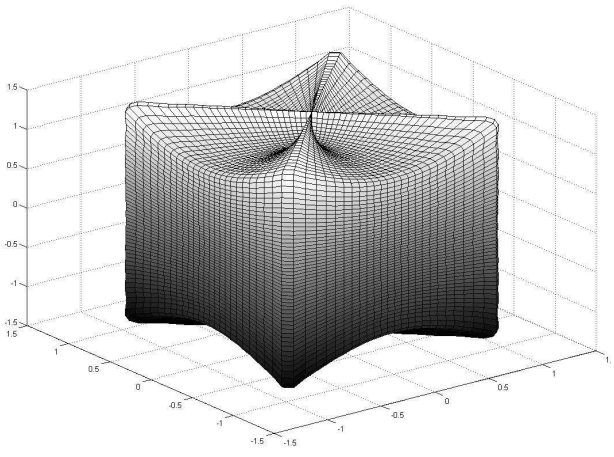

Figure 7.2: Pseudo-cube expressed in spherical coordinates via Eq. (7.1) by convolving the formula for a cylinder in θ with the same formula in ϕ.

of a cylinder in θ and a cylinder in ϕ yields a pseudo-cubic shape with minimal effort. The method can be refined analytically as well as numerically to yield exact expansions of the coefficients R_{nm}, a_{nm}, and b_{nm} that form specific geometries in Eq. (7.1).

A similar form can be used to define the surface reaction rate constant, $k_s(\theta,\phi)$ which might even depend on the surface normal of $R(\theta,\phi)$. The real utility of such a framework, however, is that the spectral method can also be used to describe the concentration profile of monomers in solution, thus we may solve for the concentration from the diffusion equation. The best-case result would be several analytical expressions for the various coefficients, such that the resultant concentration profile could be calculated to arbitrary accuracy by summing a sufficient number of terms. If no such analytical form is found, then other orthogonal function spaces will be explored.

Specific metrics can be developed that would indicate quantitatively how rod-like, how tetrapod-like, or how polyhedral a nanocrystal is from its spectral coefficients. These metrics can inform the k_s functions that yield a particular shape while disfavoring others. All of this analysis is possible without the use of computers, though the model will depend heavily on infinite series and orthogonality. The framework readily allows exploration of shapes with cylindrical symmetry by neglecting the θ dependence. Then, by examining particular ϕ-modes such as n = 1, 2, 3 and 4, it is possible to examine nanocrystals shaped like teardrops, rods or rice, triangles or tripods, and dog-bones. Other specific combinations of low-order modes can yield insight into the proto-dynamics of certain shapes.

Once the differential equations are generally converted to a series of linear-algebraic formulas, numerical solutions would be necessary to validate any analytical results, to explore simple shapes in more detail, and to address shapes whose expansions are not trivial (such octahedra). However, the important feature of the mathematical analysis is, as always, that physical parameters are retained in the linear-algebraic expressions, instead of explored one combination at a time by a computer. Explicit dependencies are easily interrogated with the analytical form, and a pencil-and-paper analysis will inform the most fruitful numerical simulations.

7.3 FUTURE DIRECTIONS: A PRACTICAL THEORY OF NUCLEATION

The phenomenon of nucleation is the thread that ties all nanocrystal syntheses together, and as our analyses imply, it is also the mystery which most frustrates efforts to control nanocrystal growth. The problem is that multiple models have been used for nucleation, but no one model truly elucidates the process.[71, 123, 142, 143] The classical Gibbs formulation of nucleation disregards the statistical nature of the formation of nuclei and is incompatible with LSW theory. The more recent Cahn-Hilliard treatment of nucleation is more insightful and more telling of why nucleation occurs as it does for nanocrystals, but it again fails to produce quantitatively applicable principles for the control of nucleation.[142] There are other models such as the LaMer model of supersaturation[143] and the Sugimoto scaling law for number of nuclei versus monomer production rate,[71] and there have been numerical studies of the phenomenon through molecular simulations or the presumption of the size distribution function of recently-generated nuclei.[40] Unfortunately, all of these investigations have only surrounded the process of nucleation without ever penetrating it in a meaningful way for nanocrystals.

Which elements of the nucleation process are most critical to nanocrystal formation has yet to be ascertained. In the vein of the theoretical treatments outlined in this thesis, a novel but straightforward model can be employed. The instantaneous material balance, Eq. (3.9) in Chapter 3 and Eq. (4.2) in Chapter 4, can be combined with the LaMer model of nucleation to examine the timeframe near where *c* is a maximum. At that maximum, the molar generation rate *c* is exactly balanced with the rate of new nucleation and the net growth of existing nanocrystals. On either side of the maximum, *c(t)* can be approximated as a parabola, $c = c_0 - \frac{1}{2}b(t - t_0)^2$:

$$\frac{dc}{dt} = -b(t - t_0) = \dot{c} - n_{nuc}\frac{dZ}{dt} - \int_0^\infty \frac{4\pi R^2}{v}\frac{dR}{dt} f(R,t)dR$$

The unknowns are the details of *f(R,t)* and the nucleation rate *dZ/dt*. The nucleation rate is a function of concentration as per both the Gibbs formula and per Cahn-Hilliard nucleation theory.[142] If between the two theories a form can be found for *dZ/dt*, then it will be possible to interrogate the unsteady evolution of *f(R,t)* during and immediately after nucleation.

Aside from the novelty of a practical theory of nucleation, a theoretical model for the number concentration of nanocrystals, *Z(t)*, would be greatly beneficial to nanocrystal analysis. The current calculation of *Z* in a nanocrystal experiment can be erroneous by up to 30% due to propagations of measurement error.[53] With a theoretical model in place, a curve-fit to *Z* can be established simultaneously with the evaluation of other measured parameters in the system. This multiple-fit procedure would improve the overall accuracy of the characterization of nanocrystals, particularly at early times when the nanocrystals are smallest and the error of all

measurements is highest. Additional theories would also help to determine what the weakest features are of current *in situ* measurement techniques.

7.4 CONCLUDING REMARKS

Though this thesis serves to expand our knowledge, we must note that these same insights developed here are transient. Given advances in experimental technology and computer simulations, other studies will eventually surpass the accuracy and understanding granted by the theories published here, obviating the assumptions and approximations and replacing them with quantitatively accurate trends, tabulations, and observed laws. The greatest utility, however, of using analytical mathematics to assess a physical-chemical problem is not always in quantitatively predicting experimental results, but occasionally in isolating what correlations the experimenters should be looking for. Before the development of our theory of size focusing, the monomer generation rate and the polydispersity of a nanocrystal population had never been linked in the literature. Before our thermodynamic investigation gold-thiolate nanocrystals, it had never before been suggested that the thiolate concentration might be the critical variable of control. In the spirit of Dr. Brus' original crystallite study, we have mapped out new insights and directed future studies toward their most useful end.

This idea is the exact motive for the theories derived in this thesis. These quantitative relations and predictions will inspire future nanocrystal experiments and will guide future engineers and manufacturers on the path to making modern nanocrystal technology accessible, useful, and economical. While the future of nanocrystal technology is unknown, these theories represent a

large step in the right direction toward understanding, controlling, and applying nanocrystals for the constant advancement of our industry and our society.

REFERENCES

1. Smith, A.M., et al., *Engineering luminescent quantum dots for In vivo molecular and cellular imaging.* Annals of Biomedical Engineering, 2006. **34**(1): p. 3-14.
2. Park, J., et al., *Synthesis of Cadmium Selenide Quantum Dots from a Non-Coordinating Solvent: Growth Kinetics and Particle Size Distribution.* The Journal of Physical Chemistry C, 2008. **112**(46): p. 17849-17854.
3. Brus, L.E., *Electron Electron and Electron-Hole Interactions in Small Semiconductor Crystallites - the Size Dependence of the Lowest Excited Electronic State.* Journal of Chemical Physics, 1984. **80**(9): p. 4403-4409.
4. Alvarez, M.M., et al., *Optical absorption spectra of nanocrystal gold molecules.* Journal of Physical Chemistry B, 1997. **101**(19): p. 3706-3712.
5. Sanders, P.G., J.A. Eastman, and J.R. Weertman, *Elastic and tensile behavior of nanocrystalline copper and palladium.* Acta Materialia, 1997. **45**(10): p. 4019-4025.
6. Puntes, V.F., K. Krishnan, and A.P. Alivisatos, *Synthesis of colloidal cobalt nanoparticles with controlled size and shapes.* Topics in Catalysis, 2002. **19**(2): p. 145-148.
7. Murray, C.B., D.J. Norris, and M.G. Bawendi, *Synthesis and Characterization of Nearly Monodisperse Cde (E = S, Se, Te) Semiconductor Nanocrystallites.* Journal of the American Chemical Society, 1993. **115**(19): p. 8706-8715.
8. Reed, M.A., et al., *Spatial Quantization in Gaas-Algaas Multiple Quantum Dots.* Journal of Vacuum Science & Technology B, 1986. **4**(1): p. 358-360.
9. Search conducted for "nanocrystal*" on ISI Web of Knowledge on July 7, 2012, then refined with the terms "quantum dot* OR semicond*".
10. Alivisatos, A.P., *Semiconductor clusters, nanocrystals, and quantum dots.* Science, 1996. **271**(5251): p. 933-937.
11. Colvin, V.L., M.C. Schlamp, and A.P. Alivisatos, *Light-Emitting-Diodes Made from Cadmium Selenide Nanocrystals and a Semiconducting Polymer.* Nature, 1994. **370**(6488): p. 354-357.
12. Huynh, W.U., J.J. Dittmer, and A.P. Alivisatos, *Hybrid nanorod-polymer solar cells.* Science, 2002. **295**(5564): p. 2425-2427.
13. Peng, K.Y., S.A. Chen, and W.S. Fann, *Efficient light harvesting by sequential energy transfer across aggregates in polymers of finite conjugational segments with short aliphatic linkages.* Journal of the American Chemical Society, 2001. **123**(46): p. 11388-11397.
14. Michalet, X., et al., *Quantum dots for live cells, in vivo imaging, and diagnostics.* Science, 2005. **307**(5709): p. 538-544.
15. Chan, W.C.W. and S.M. Nie, *Quantum dot bioconjugates for ultrasensitive nonisotopic detection.* Science, 1998. **281**(5385): p. 2016-2018.
16. Gao, X.H., et al., *In vivo molecular and cellular imaging with quantum dots.* Current Opinion in Biotechnology, 2005. **16**(1): p. 63-72.
17. Alivisatos, P., *The use of nanocrystals in biological detection.* Nature Biotechnology, 2004. **22**(1): p. 47-52.
18. Somers, R.C., M.G. Bawendi, and D.G. Nocera, *CdSe nanocrystal based chem-/bio-sensors.* Chemical Society Reviews, 2007. **36**(4): p. 579-591.

19. DiVincenzo, D.P., *Quantum computing and single-qubit measurements using the spin-filter effect (invited).* Journal of Applied Physics, 1999. **85**(8): p. 4785-4787.
20. Choi, K.S., et al., *Mapping photonic entanglement into and out of a quantum memory.* Nature, 2008. **452**(7183): p. 67-U4.
21. Clarke, J. and F.K. Wilhelm, *Superconducting quantum bits.* Nature, 2008. **453**(7198): p. 1031-1042.
22. DiCarlo, L., et al., *Demonstration of two-qubit algorithms with a superconducting quantum processor.* Nature, 2009. **460**(7252): p. 240-244.
23. Ladd, T.D., et al., *Quantum computers.* Nature, 2010. **464**(7285): p. 45-53.
24. Ostwald, W., *Lehrbuch der allgemeinen chemie*. 1902: W. Engelmann.
25. Ostwald, W., *On the assumed isomerism of red and yellow mercury oxide and the surface-tension of solid bodies.* Zeitschrift Fur Physikalische Chemie--Stochiometrie Und Verwandtschaftslehre, 1900. **34**(4): p. 495-503.
26. Lin, X.M., C.M. Sorensen, and K.J. Klabunde, *Digestive ripening, nanophase segregation and superlattice formation in gold nanocrystal colloids.* Journal of Nanoparticle Research, 2000. **2**: p. 157-164.
27. Buscall, R., S.S. Davis, and D.C. Potts, *EFFECT OF LONG-CHAIN ALKANES ON THE STABILITY OF OIL-IN-WATER EMULSIONS - SIGNIFICANCE OF OSTWALD RIPENING.* Colloid and Polymer Science, 1979. **257**(6): p. 636-644.
28. Peng, X.G., J. Wickham, and A.P. Alivisatos, *Kinetics of II-VI and III-V colloidal semiconductor nanocrystal growth: "Focusing" of size distributions.* Journal of the American Chemical Society, 1998. **120**(21): p. 5343-5344.
29. Vladimirova, N., A. Malagoli, and R. Mauri, *Diffusion-driven phase separation of deeply quenched mixtures.* Physical Review E, 1998. **58**(6): p. 7691-7699.
30. Voorhees, P.W., *OSTWALD RIPENING OF 2-PHASE MIXTURES.* Annual Review of Materials Science, 1992. **22**: p. 197-215.
31. Marre, S., et al., *Supercritical Continuous-Microflow Synthesis of Narrow Size Distribution Quantum Dots.* Advanced Materials, 2008. **20**(24): p. 4830-+.
32. Stoeva, S., et al., *Gram-scale synthesis of monodisperse gold colloids by the solvated metal atom dispersion method and digestive ripening and their organization into two- and three-dimensional structures.* Journal of the American Chemical Society, 2002. **124**(10): p. 2305-2311.
33. Dickerson, B.D., et al., *Synthesis kinetics of CdSe quantum dots in trioctylphosphine oxide and in stearic acid.* Applied Physics Letters, 2005. **86**(17).
34. Harada, M., N. Tamura, and M. Takenaka, *Nucleation and Growth of Metal Nanoparticles during Photoreduction Using In Situ Time-Resolved SAXS Analysis.* Journal of Physical Chemistry C, 2011. **115**(29): p. 14081-14092.
35. Su, H., et al., *Study on Growth Kinetics of CdSe Nanocrystals with a New Model.* Nanoscale Research Letters, 2010. **5**(5): p. 823-828.
36. Varghese, N., K. Biswas, and C.N.R. Rao, *Investigations of the growth kinetics of capped CdSe and CdS nanocrystals by a combined use of small angle X-ray scattering and other techniques.* Chemistry-an Asian Journal, 2008. **3**(8-9): p. 1435-1442.
37. Chen, Y.F., E. Johnson, and X.G. Peng, *Formation of monodisperse and shape-controlled MnO nanocrystals in non-injection synthesis: Self-focusing via.* Journal of the American Chemical Society, 2007. **129**(35): p. 10937-10947.

38. Dushkin, C.D., et al., *The kinetics of growth of semiconductor nanocrystals in a hot amphiphile matrix.* Advances in Colloid and Interface Science, 2000. **88**(1-2): p. 37-78.
39. Talapin, D.V., et al., *Evolution of an ensemble of nanoparticles in a colloidal solution: Theoretical study.* Journal of Physical Chemistry B, 2001. **105**(49): p. 12278-12285.
40. van Embden, J., et al., *Evolution of Colloidal Nanocrystals: Theory and Modeling of their Nucleation and Growth.* Journal of Physical Chemistry C, 2009. **113**(37): p. 16342-16355.
41. Mantzaris, N.V., *Liquid-phase synthesis of nanoparticles: Particle size distribution dynamics and control.* Chemical Engineering Science, 2005. **60**(17): p. 4749-4770.
42. Ould-Ely, T., et al., *Large-scale engineered synthesis of BaTiO3 nanoparticles using low-temperature bioinspired principles.* Nature Protocols, 2011. **6**(1): p. 97-104.
43. Chan, E.M., et al., *Reproducible, High-Throughput Synthesis of Colloidal Nanocrystals for Optimization in Multidimensional Parameter Space.* Nano Letters, 2010. **10**(5): p. 1874-1885.
44. In the publication by Chan et al., CdSe size does not depend on Cd-precursor amounts, and it depends only slightly on the Se-precursor. A factor of 10 difference in Se effects a 20% change in size, while doubling the Se yields no change in size within measurement error.
45. Prasad, B.L.V., et al., *Digestive ripening of thiolated gold nanoparticles: The effect of alkyl chain length.* Langmuir, 2002. **18**(20): p. 7515-7520.
46. Prasad, B.L.V., et al., *Digestive-ripening agents for gold nanoparticles: Alternatives to thiols.* Chemistry of Materials, 2003. **15**(4): p. 935-942.
47. Sahu, P. and B.L.V. Prasad, *Effect of digestive ripening agent on nanoparticle size in the digestive ripening process.* Chemical Physics Letters, 2012. **525-26**: p. 101-104.
48. Samia, A.C.S., et al., *Ligand effect on the growth and the digestion of co nanocrystals.* Journal of the American Chemical Society, 2005. **127**(12): p. 4126-4127.
49. Samia, A.C.S., et al., *Effect of ligand-metal interactions on the growth of transition-metal and alloy nanoparticles.* Chemistry of Materials, 2006. **18**(22): p. 5203-5212.
50. Kwon, S.G., et al., *Kinetics of monodisperse iron oxide nanocrystal formation by "heating-up" process.* Journal of the American Chemical Society, 2007. **129**(41): p. 12571-12584.
51. Smetana, A.B., et al., *Low-temperature metallic alloying of copper and silver nanoparticles with gold nanoparticles through digestive ripening.* Journal of Physical Chemistry B, 2006. **110**(5): p. 2155-2158.
52. Cingarapu, S., et al., *Transformation of Indium Nanoparticles to β-Indium Sulfide: Digestive Ripening and Visible Light-Induced Photocatalytic Properties.* Langmuir, 2012. **28**(7): p. 3569-3575.
53. Owen, J.S., et al., *Precursor Conversion Kinetics and the Nucleation of Cadmium Selenide Nanocrystals.* Journal of the American Chemical Society, 2010. **132**(51): p. 18206-18213.
54. Lifshitz, I.M. and V.V. Slyozov, *The Kinetics of Precipitation from Supersaturated Solid Solutions.* Journal of Physics and Chemistry of Solids, 1961. **19**(1-2): p. 35-50.
55. Wagner, C., *Theorie Der Alterung Von Niederschlagen Durch Umlosen (Ostwald-Reifung).* Zeitschrift Fur Elektrochemie, 1961. **65**(7-8): p. 581-591.
56. Kahlweit, M., *Ostwald Ripening of Precipitates.* Advances in Colloid and Interface Science, 1975. **5**(1): p. 1-35.

57. Viswanatha, R., et al., *Growth Mechanism of Cadmium Sulfide Nanocrystals.* (unpublished).
58. Schlamp, M.C., X.G. Peng, and A.P. Alivisatos, *Improved efficiencies in light emitting diodes made with CdSe(CdS) core/shell type nanocrystals and a semiconducting polymer.* Journal of Applied Physics, 1997. **82**(11): p. 5837-5842.
59. Lin, X.M., et al., *Formation of long-range-ordered nanocrystal superlattices on silicon nitride substrates.* Journal of Physical Chemistry B, 2001. **105**(17): p. 3353-3357.
60. Lin, X.M., C.M. Sorensen, and K.J. Klabunde, *Ligand-induced gold nanocrystal superlattice formation in colloidal solution.* Chemistry of Materials, 1999. **11**(2): p. 198-202.
61. Murray, C.B., C.R. Kagan, and M.G. Bawendi, *SELF-ORGANIZATION OF CDSE NANOCRYSTALLITES INTO 3-DIMENSIONAL QUANTUM-DOT SUPERLATTICES.* Science, 1995. **270**(5240): p. 1335-1338.
62. Mews, A., et al., *PREPARATION, CHARACTERIZATION, AND PHOTOPHYSICS OF THE QUANTUM-DOT QUANTUM-WELL SYSTEM CDS/HGS/CDS.* Journal of Physical Chemistry, 1994. **98**(3): p. 934-941.
63. Dabbousi, B.O., et al., *(CdSe)ZnS core-shell quantum dots: Synthesis and characterization of a size series of highly luminescent nanocrystallites.* Journal of Physical Chemistry B, 1997. **101**(46): p. 9463-9475.
64. Kalyuzhny, G. and R.W. Murray, *Ligand effects on optical properties of CdSe nanocrystals.* Journal of Physical Chemistry B, 2005. **109**(15): p. 7012-7021.
65. Puzder, A., et al., *The effect of organic ligand binding on the growth of CdSe nanoparticles probed by Ab initio calculations.* Nano Letters, 2004. **4**(12): p. 2361-2365.
66. Yu, W.W., Y.A. Wang, and X.G. Peng, *Formation and stability of size-, shape-, and structure-controlled CdTe nanocrystals: Ligand effects on monomers and nanocrystals.* Chemistry of Materials, 2003. **15**(22): p. 4300-4308.
67. Peng, X.G., et al., *Shape control of CdSe nanocrystals.* Nature, 2000. **404**(6773): p. 59-61.
68. El-Sayed, M.A., *Small Is Different: Shape-, Size-, and Composition-Dependent Properties of Some Colloidal Semiconductor Nanocrystals.* Accounts of Chemical Research, 2004. **37**(5): p. 326-333.
69. Sugimoto, T., *Preparation of Monodispersed Colloidal Particles.* Advances in Colloid and Interface Science, 1987. **28**(1): p. 65-108.
70. Sugimoto, T. and F. Shiba, *Spontaneous nucleation of monodisperse silver halide particles from homogeneous gelatin solution II: silver bromide.* Colloids and Surfaces A: Physicochemical and Engineering Aspects, 2000. **164**(2-3): p. 205-215.
71. Sugimoto, T., et al., *Spontaneous nucleation of monodisperse silver halide particles from homogeneous gelatin solution I: silver chloride.* Colloids and Surfaces A: Physicochemical and Engineering Aspects, 2000. **164**(2-3): p. 183-203.
72. Brust, M., et al., *Synthesis of Thiol-Derivatized Gold Nanoparticles in a 2-Phase Liquid-Liquid System.* Journal of the Chemical Society-Chemical Communications, 1994(7): p. 801-802.
73. Brust, M., et al., *Novel Gold-Dithiol Nano-Networks with Nonmetallic Electronic-Properties.* Advanced Materials, 1995. **7**(9): p. 795-&.
74. Leff, D.V., et al., *Thermodynamic Control of Gold Nanocrystal Size - Experiment and Theory.* Journal of Physical Chemistry, 1995. **99**(18): p. 7036-7041.

75. Badia, A., et al., *Gold-sulfur interactions in alkylthiol self-assembled monolayers formed on gold nanoparticles studied by solid-state NMR.* Journal of the American Chemical Society, 1997. **119**(45): p. 11104-11105.
76. Badia, A., et al., *Self-assembled monolayers on gold nanoparticles.* Chemistry-a European Journal, 1996. **2**(3): p. 359-363.
77. Bandyopadhyay, K., et al., *Spontaneously organized molecular assembly of an aromatic organic disulfide on silver/platinum alloy surfaces: an angle dependent X-ray photoemission investigation.* Journal of Electron Spectroscopy and Related Phenomena, 1997. **87**(2): p. 101-107.
78. Buining, P.A., et al., *Preparation of functional silane-stabilized gold colloids in the (sub)nanometer size range.* Langmuir, 1997. **13**(15): p. 3921-3926.
79. Cleveland, C.L., et al., *Structural evolution of larger gold clusters.* Zeitschrift Fur Physik D-Atoms Molecules and Clusters, 1997. **40**(1-4): p. 503-508.
80. Leff, D.V., L. Brandt, and J.R. Heath, *Synthesis and characterization of hydrophobic, organically-soluble gold nanocrystals functionalized with primary amines.* Langmuir, 1996. **12**(20): p. 4723-4730.
81. Schaaff, T.G., et al., *Isolation of smaller nanocrystal au molecules: Robust quantum effects in optical spectra.* Journal of Physical Chemistry B, 1997. **101**(40): p. 7885-7891.
82. Terrill, R.H., et al., *Monolayers in three dimensions: NMR, SAXS, thermal, and electron hopping studies of alkanethiol stabilized gold clusters.* Journal of the American Chemical Society, 1995. **117**(50): p. 12537-12548.
83. Sarathy, K.V., et al., *Thiol-Derivatized Nanocrystalline Arrays of Gold, Silver, and Platinum.* The Journal of Physical Chemistry B, 1997. **101**(48): p. 9876-9880.
84. Elghanian, R., et al., *Selective colorimetric detection of polynucleotides based on the distance-dependent optical properties of gold nanoparticles.* Science, 1997. **277**(5329): p. 1078-1081.
85. Matthiesen, J.E., et al., *Loss of Hydrogen upon Exposure of Thiol to Gold Clusters at Low Temperature.* Journal of the American Chemical Society, 2012. **134**(22): p. 9376-9379.
86. Jadzinsky, P.D., et al., *Structure of a thiol monolayer-protected gold nanoparticle at 1.1 angstrom resolution.* Science, 2007. **318**(5849): p. 430-433.
87. Owens, T.M., et al., *Formation of alkylsilane-based monolayers on gold.* Journal of the American Chemical Society, 2002. **124**(24): p. 6800-6801.
88. Jiang, D.-e., *Au adatom-linked CH3S-Au-SCH3 complexes on Au(111).* Chemical Physics Letters, 2009. **477**(1-3): p. 90-94.
89. Jiang, D.-e., et al., *The "Staple" motif: A key to stability of thiolate-protected gold nanoclusters.* Journal of the American Chemical Society, 2008. **130**(9): p. 2777-+.
90. Jiang, D.-E., *Understanding and Predicting Thiolated Gold Nanoclusters from First Principles.* Acta Physico-Chimica Sinica, 2010. **26**(4): p. 999-1016.
91. Yang, Z. and K.J. Klabunde, *Synthesis of nearly monodisperse palladium (Pd) nanoparticles by using oleylamine and trioctylphosphine mixed ligands.* Journal of Organometallic Chemistry, 2009. **694**(7-8): p. 1016-1021.
92. Jin, R.C., S. Egusa, and N.F. Scherer, *Thermally-induced formation of atomic Au clusters and conversion into nanocubes.* Journal of the American Chemical Society, 2004. **126**(32): p. 9900-9901.

93. Yang, Z., K.J. Klabunde, and C.M. Sorensen, *From monodisperse sulfurized palladium nanoparticles to tiara Pd(II) thiolate clusters: Influence of thiol ligand on thermal treatment of a palladium(II)-amine system.* Journal of Physical Chemistry C, 2007. **111**(49): p. 18143-18147.
94. Wang, F., et al., *Chemical controlled reversible gold nanoparticles dissolution and reconstruction at room-temperature.* Chemical Communications, 2012. **48**(49): p. 6136-6138.
95. Cha, S.-H., et al., *Preparation and photoluminescent properties of gold(I)-alkanethiolate complexes having highly ordered supramolecular structures.* Chemistry of Materials, 2007. **19**(25): p. 6297-6303.
96. Cha, S.-H., et al., *Nanoparticles under heat treatment process.* Journal of Physical Chemistry C, 2008. **112**(36): p. 13862-13868.
97. Kim, J.U., et al., *Synthesis of gold nanoparticles from gold(I)-alkanethiolate complexes with supramolecular structures through electron beam irradiation in TEM.* Journal of the American Chemical Society, 2005. **127**(28): p. 9962-9963.
98. Cha, S.-H., et al., *Thermal Behavior of Gold(I)−Thiolate Complexes and Their Transformation into Gold Nanoparticles under Heat Treatment Process.* The Journal of Physical Chemistry C, 2008. **112**(36): p. 13862-13868.
99. Zheng, N., J. Fan, and G.D. Stucky, *One-step one-phase synthesis of monodisperse noble-metallic nanoparticles and their colloidal crystals.* Journal of the American Chemical Society, 2006. **128**(20): p. 6550-6551.
100. Koerner, H., et al., *In Situ UV/Vis, SAXS, and TEM Study of Single-Phase Gold Nanoparticle Growth.* Chemistry of Materials, 2012. **24**(6): p. 981-995.
101. Xia, Y., et al., *Shape-Controlled Synthesis of Metal Nanocrystals: Simple Chemistry Meets Complex Physics?* Angewandte Chemie-International Edition, 2009. **48**(1): p. 60-103.
102. Yin, Y. and A.P. Alivisatos, *Colloidal nanocrystal synthesis and the organic-inorganic interface.* Nature, 2005. **437**(7059): p. 664-670.
103. Bauer, L.A., N.S. Birenbaum, and G.J. Meyer, *Biological applications of high aspect ratio nanoparticles.* Journal of Materials Chemistry, 2004. **14**(4): p. 517-526.
104. Chen, J., et al., *Shape-controlled synthesis of platinum nanocrystals for catalytic and electrocatalytic applications.* Nano Today, 2009. **4**(1): p. 81-95.
105. Jose, R., et al., *Structure-property correlation of CdSe clusters using experimental results and first-principles DFT calculations.* Journal of the American Chemical Society, 2006. **128**(2): p. 629-636.
106. Joswig, J.O., M. Springborg, and G. Seifert, *Structural and electronic properties of cadmium sulfide clusters.* Journal of Physical Chemistry B, 2000. **104**(12): p. 2617-2622.
107. Rempel, J.Y., et al., *Properties of the CdSe(0001), (0001), and (1120) single crystal surfaces: Relaxation, reconstruction, and adatom and admolecule adsorption.* Journal of Physical Chemistry B, 2005. **109**(41): p. 19320-19328.
108. Jiang, D.-e., et al., *What Protects the Core When the Thiolated Au Cluster is Extremely Small?* Journal of Physical Chemistry C, 2009. **113**(39): p. 16983-16987.
109. Lee, D.K., et al., *A theoretical model for digestive ripening.* Acta Materialia, 2007. **55**(15): p. 5281-5288.

110. Israelachvili, J.N., D.J. Mitchell, and B.W. Ninham, *THEORY OF SELF-ASSEMBLY OF HYDROCARBON AMPHIPHILES INTO MICELLES AND BILAYERS.* Journal of the Chemical Society-Faraday Transactions Ii, 1976. **72**: p. 1525-1568.
111. Clark, M.D., et al., *Focusing Nanocrystal Size Distributions via Production Control.* Nano Letters, 2011. **11**(5): p. 1976-1980.
112. Allen, P.M., B.J. Walker, and M.G. Bawendi, *Mechanistic Insights into the Formation of InP Quantum Dots.* Angewandte Chemie-International Edition, 2010. **49**(4): p. 760-762.
113. Joo, J., et al., *A Reduction Pathway in the Synthesis of PbSe Nanocrystal Quantum Dots.* Journal of the American Chemical Society, 2009. **131**(30): p. 10620-10628.
114. Liu, H.T., J.S. Owen, and A.P. Alivisatos, *Mechanistic study of precursor evolution in colloidal group II-VI semiconductor nanocrystal synthesis.* Journal of the American Chemical Society, 2007. **129**(2): p. 305-312.
115. Steckel, J.S., et al., *On the mechanism of lead chalcogenide nanocrystal formation.* Journal of the American Chemical Society, 2006. **128**(40): p. 13032-13033.
116. Baek, J., et al., *Investigation of Indium Phosphide Nanocrystal Synthesis Using a High-Temperature and High-Pressure Continuous Flow Microreactor.* Angewandte Chemie International Edition, 2011. **50**(3): p. 627-630.
117. Reiss, H., *The Growth of Uniform Colloidal Dispersions.* Journal of Chemical Physics, 1951. **19**(4): p. 482-487.
118. Kanie, K. and T. Sugimoto, *Organic-inorganic hybrid liquid crystals: Hybridization of calamitic liquid-crystalline amines with monodispersed anisotropic TiO2 nanoparticles.* Journal of the American Chemical Society, 2003. **125**(35): p. 10518-10519.
119. The bulk concentration in solution never reaches a large enough value to cause additional nucleation.
120. Peng et al. noted that the number of particles in their synthesis stayed constant during "focusing" events and decreased during "defocusing", presumably due to the Ostwald ripening process in which nanocrystal concentration decreases with time.
121. The deviation of our fit from the observed polydispersity during the Ostwald ripening period may be caused by a background acid catalyzed TOPSe cleavage, which maintains a non-zero monomer production.
122. We fit the generation of CdSe to a general rate law, in which the reaction rate constant the exponents of the two precursors were permitted to float. All reaction data were used in the fit of the three parameters.
123. Sugimoto, T., *The Theory of the Nucleation of Monodisperse Particles in Open Systems and Its Application to AgBr Systems.* Journal of Colloid and Interface Science, 1992. **150**(1): p. 208-225.
124. The pseudo-steady state supersaturation in so-called “heating-up” methods will depend on the relative response of the nucleation and precursor conversion rate to increasing temperature. Furthermore, the relationship between concentration and the critical radius Rc depends strongly on temperature. For examples of the heating-up method see: Park, J., et al. Angew. Chem., Int. Ed. 46, 4630 – 4660 (2007); Yang, Y. A., et al. Angew. Chem., Int. Ed. 44, 6712-6715 (2005); Chen, Y; Johnson, E.; Peng, X. J. Am. Chem. Soc. 129, 10937-10947 (2007).
125. Bullen, C.R. and P. Mulvaney, *Nucleation and growth kinetics of CdSe nanocrystals in octadecene.* Nano Letters, 2004. **4**(12): p. 2303-2307.

126. Viswanatha, R. and D.D. Sarma, *Study of the growth of capped ZnO nanocrystals: A route to rational synthesis.* Chemistry-a European Journal, 2006. **12**(1): p. 180-186.
127. Link, S. and M.A. El-Sayed, *Shape and size dependence of radiative, non-radiative and photothermal properties of gold nanocrystals.* International Reviews in Physical Chemistry, 2000. **19**(3): p. 409-453.
128. Frenkel, A.I., et al., *Size-controlled synthesis and characterization of thiol-stabilized gold nanoparticles.* Journal of Chemical Physics, 2005. **123**(18): p. -.
129. Hostetler, M.J., et al., *Alkanethiolate gold cluster molecules with core diameters from 1.5 to 5.2 nm: Core and monolayer properties as a function of core size.* Langmuir, 1998. **14**(1): p. 17-30.
130. Martin, J.E., et al., *Control of the interparticle spacing in gold nanoparticle superlattices.* Journal of Physical Chemistry B, 2000. **104**(40): p. 9475-9486.
131. Sarma, DD. Unpublished results.
132. Prince, L.M., *Microemulsions: theory and practice*. 1977: Academic Press.
133. Sidhaye, D.S. and B.L.V. Prasad, *Many manifestations of digestive ripening: monodispersity, superlattices and nanomachining.* New Journal of Chemistry, 2011. **35**(4): p. 755-763.
134. Szleifer, I. and M.A. Carignano, *Tethered polymer layers.* Advances in Chemical Physics, Vol Xciv, 1996. **94**: p. 165-260.
135. Carignano, M.A. and I. Szleifer, *Statistical Thermodynamic Theory of Grafted Polymeric Layers.* Journal of Chemical Physics, 1993. **98**(6): p. 5006-5018.
136. Nanda, K.K., *Bulk cohesive energy and surface tension from the size-dependent evaporation study of nanoparticles.* Applied Physics Letters, 2005. **87**(2).
137. Jose, D., et al., *Size Focusing of Nanoparticles by Thermodynamic Control through Ligand Interactions. Molecular Clusters Compared with Nanoparticles of Metals.* Journal of Physical Chemistry Letters, 2012. **3**(7): p. 885-890.
138. Norman ZM, Owen JS. Unpublished results.
139. Liao, H.W., et al., *Solvothermal Elemental Direct Reaction to CdE (E = S, Se, Te) Semiconductor Nanorod.* Inorganic chemistry, 1999. **38**(7): p. 1382-1387.
140. Milliron, D.J., et al., *Colloidal nanocrystal heterostructures with linear and branched topology.* Nature, 2004. **430**(6996): p. 190-195.
141. Dittmer, J.J. and A.P. Alivisatos, *Hybrid nanorod-polymer solar cells.* Science (New York, N.Y.), 2002. **295**(5564): p. 2425-2427.
142. Cahn, J.W. and J.E. Hilliard, *Free Energy of a Nonuniform System .3. Nucleation in a 2-Component Incompressible Fluid.* Journal of Chemical Physics, 1959. **31**(3): p. 688-699.
143. Lamer, V.K. and R.H. Dinegar, *Theory, Production and Mechanism of Formation of Monodispersed Hydrosols.* Journal of the American Chemical Society, 1950. **72**(11): p. 4847-4854.

APPENDIX A: DERIVINGTHE ASYMPTOTION DISTRIBUTION IN LSW THEORY

The function *g(t)* is determined by declaring a new parameter φ, the total volume fraction of solute contained in particles. It is defined as the total volume of all particles divided by the total system volume, or the particle volume times the particle concentration. Thus it is defined as follows:

$$\varphi = \int_0^\infty \frac{4\pi R^3}{3} f(R,t)dR = g(t)\int_0^\infty \frac{4\pi R_c^3\rho^3}{3}\rho^2 h(\rho)R_c d\rho \tag{A1}$$

The volume fraction φ is nearly constant because of the assumption $dc/dt \sim 0$ and the consequence that all monomers that desorb from shrinking particles will adsorb onto growing particles. Therefore, *g(t)* can be expressed in terms of R_c and otherwise constant quantities:

$$g(t) = \frac{3\varphi}{4\pi R_c^4 \int_0^\infty \rho^5 h(\rho)d\rho} \tag{A2}$$

Wagner places the asymptotic form of $f(R,t) = g(t)\rho^2 h(\rho)$ into two different evaluations of *dZ/dt*:

$$\begin{aligned} \frac{dZ}{dt} &= \frac{d}{dt}\int_0^\infty f(R,t)dR = \frac{d(gR_c)}{dt}\int_0^\infty \rho^2 h(\rho)d\rho \\ \frac{dZ}{dt} &= \lim_{R\to 0} f(R,t)\frac{dR}{dt} = -g(t)\frac{K_D}{R_c^2}h(0) \end{aligned} \tag{A3a,b}$$

Let us declare that $h(0) = 1$, which loses no generality because *g(t)* contains $h(\rho)$ in its denominator. The integral $\int_0^{\inf}\rho^2 h(\rho)d\rho$ is a constant with time and Wagner defines it as a new parameter $\gamma_D = \int_0^{\inf}\rho^2 h(\rho)d\rho$. Therefore, the result of using *dZ/dt* is:

$$\frac{d(gR_c)}{dt} = -g\frac{K_D}{\gamma_D R_c^2} \tag{A4}$$

Inserting the definition for *g(t)*, we find that the φ term, the integral of $\rho^5 h(\rho)$, and the $4\pi/3$ each cancel with the following result:

$$\frac{d}{dt}\left[R_c^3\right]^{-1} = -\left[R_c^3\right]^{-2}\frac{K_D}{\gamma_D} \tag{A5}$$

From this, we obtain the time-derivative of the cube of the critical radius:

$$\frac{dR_c^3}{dt} = \frac{K_D}{\gamma_D} \tag{A6}$$

APPENDIX B: DETAILED PERTURBATION ANALYSIS FOR THE THEORY OF SIZE FOCUSING

The distribution function *f(R,t)* evolves according to the equation $\frac{\partial f}{\partial t} = -\frac{\partial}{\partial R}\left(f\,\frac{dR}{dt}\right)$[41, 54, 55], which has no general solution for $\dot{c} > 0$. To determine the temporal behavior of the polydispersity, we use a time-dependent Gaussian,

$$f(R,t) = \frac{1}{\sqrt{2\pi\sigma^2(t)}}\exp\left(-\frac{\left(R-\langle R\rangle_t\right)^2}{2\sigma^2(t)}\right) \tag{B1}$$

with the polydispersity $\sigma(t)$ and the average radius $\langle R\rangle$ both functions of time. Inserting this distribution into the evolution equation, and presuming that all changes in the distribution are reflected in the time-wise behavior of $\sigma(t)$ and $\langle R\rangle$, provides the following:

$$\left(\frac{\left(R-\langle R\rangle\right)^2}{\sigma^3}-\frac{1}{\sigma}\right)\frac{d\sigma}{dt}+\frac{R-\langle R\rangle}{\sigma^2}\frac{d\langle R\rangle}{dt} = -\frac{K_D}{R^3}\left[\left(-\frac{R^2}{\sigma^2}+\frac{\langle R\rangle R}{\sigma^2}-1\right)\left(\frac{R}{R_c}-1\right)+1\right] \tag{B2}$$

We may now analyze this equation using regular perturbation analysis about the average $R = \langle R\rangle$, therefore we make the replacement $R = \langle R\rangle(1+\varepsilon)$ in Equation (B2):

$$\begin{aligned}&\left[\left(\frac{\langle R\rangle^2\varepsilon^2}{\sigma^2}-1\right)\frac{1}{\sigma}\frac{d\sigma}{dt}+\frac{\langle R\rangle\varepsilon}{\sigma^2}\frac{d\langle R\rangle}{dt}\right]\\ &= -\frac{K_D}{\langle R\rangle^3(1+\varepsilon)^3}\left[\left(-\frac{\langle R\rangle^2(1+\varepsilon)^2}{\sigma^2}+\frac{\langle R\rangle^2(1+\varepsilon)}{\sigma^2}-1\right)\left(\frac{\langle R\rangle(1+\varepsilon)}{R_c}-1\right)+1\right]\end{aligned} \tag{B3}$$

Next we only examine the region near $R = \langle R\rangle$ such that $\varepsilon << 1$. We only retain the terms proportional to ε^0, ε^1 and ε^2. (Note: the right-hand side has no terms proportional to ε^3 or higher, thus all higher-order perturbations are mathematically trivial and physically invalid.) Additionally, the terms independent of ε must be equal and the terms proportional to ε must vary together, as must the terms proportional to ε^2. Therefore, perturbation analysis yields three differential equations:

$$-\frac{1}{\sigma}\frac{d\sigma}{dt} = \frac{K_D}{\langle R\rangle^3}\left[\frac{\langle R\rangle}{R_c}-2\right] \tag{B4a}$$

$$\frac{\langle R\rangle}{\sigma^2}\frac{d\langle R\rangle}{dt} = \frac{K_D}{\langle R\rangle^3}\left[\frac{\langle R\rangle^2}{\sigma^2}\left(\frac{\langle R\rangle}{R_c}-1\right)-2\frac{\langle R\rangle}{R_c}\right] \tag{B4b}$$

$$-\frac{\langle R\rangle^2}{\sigma^2}\frac{1}{\sigma}\frac{d\sigma}{dt} = \frac{K_D}{\langle R\rangle^3}\left[\frac{\langle R\rangle^2}{\sigma^2}\left(\frac{\langle R\rangle}{R_c}-2\right)-\frac{\langle R\rangle}{R_c}\right] \tag{B4c}$$

Using Eq. (4.4) from Chapter 4, we are able make the replacement $\langle R\rangle/R_c = \xi + 1$ in the above equations. Additionally, for any system in which $\langle R\rangle/R_c > 2$ (i.e. the systems of interest here), equation B4a clearly indicates that narrowing will occur. This agrees explicitly with Sugimoto's conclusion.[69] After some time, the ratio $\langle R\rangle^2/\sigma^2$ increases substantially, and we may make the long-time approximation $\langle R\rangle^2/\sigma^2 >> 1$ in equations (B4a-c) and drop all other terms,

$$\frac{1}{\sigma}\frac{d\sigma}{dt} = -\frac{K_D}{\langle R\rangle^3}(\xi - 1) \tag{B5a}$$

$$\frac{1}{\langle R\rangle}\frac{d\langle R\rangle}{dt} = \frac{K_D\xi}{\langle R\rangle^3} \tag{B5b}$$

$$\frac{1}{\sigma}\frac{d\sigma}{dt} = -\frac{K_D}{\langle R\rangle^3}(\xi - 1) \tag{B5c}$$

Clearly, for a monodisperse distribution, equations (B5a) and (B5c) are *equal* up to a 2nd-order perturbation. Meanwhile, by ξ's definition $K_D\xi = v\dot{c}/4\pi Z$, and we see Eq. (B5b) therefore simplifies to

$$\frac{d\langle R\rangle^3}{dt} = \frac{3v\dot{c}}{4\pi Z} = 3K_D\xi \tag{B6}$$

which is equivalent to Eq. (4.3) in the main text for monodisperse distributions. If we include this monodisperse growth law in Eq. (B5a) or (B5c), we find the following:

$$-\frac{1}{\sigma}\frac{d\sigma}{dt} = \frac{K_D}{\langle R\rangle^3}(\xi - 1) = \frac{K_D\xi}{\langle R\rangle^3}\left(1 - \frac{1}{\xi}\right) = \frac{1}{\langle R\rangle^3}\frac{1}{3}\frac{d\langle R\rangle^3}{dt}\left(1 - \frac{1}{\xi}\right)$$

$$\frac{1}{\sigma}\frac{d\sigma}{dt} = \frac{1}{\langle R\rangle}\frac{d\langle R\rangle}{dt}\left(\frac{1}{\xi} - 1\right) \tag{B7}$$

For ξ constant or nearly so, we integrate Eq. (B7) from initial conditions $\langle R\rangle_0$ and σ_0:

$$\ln\frac{\sigma}{\sigma_0} = \left(\frac{1}{\xi} - 1\right)\ln\frac{\langle R\rangle}{\langle R\rangle_0} \tag{B8}$$

Equation (B8) clearly yields the parametric diagram Fig. 4.1 in Chapter 4. Taking the exponential of (B8) yields Eq. (4.7), completing the derivation:

$$\frac{\sigma}{\sigma_0} = \left(\frac{\langle R\rangle}{\langle R\rangle_0}\right)^{\frac{1}{\xi}-1} \quad \blacksquare \tag{B9}$$

As noted at the end of Section 4.2, we have performed the analogous derivation of equations (B1-B9) under surface-reaction control (i.e. $k_s R << D$). The only difference is that the R-derivative yields fewer terms in Eqs. (B4) and (B5), and the term in brackets in Eq. (B4a) becomes $[\langle R\rangle/R_c - 1] = \xi$, instead of $[\langle R\rangle/R_c - 2] = (\xi - 1)$ for diffusion-limited systems. Naturally, this causes the exponent in Eq. (B9) to change from $^1/_\xi - 1$, which has the capacity to be negative, to simply $^1/_\xi$ which is always positive. It clearly becomes impossible for σ to explicitly decrease with time regardless of $\dot{c}$ for nanocrystals growing under surface-reaction control.

APPENDIX C: DERIVATION OF $f_b(R,t)$, THE BROADENING-ZONE DISTRIBUTION, DURING PRODUCTION-CONTROLLED GROWTH

We begin with the form of *dR/dt* that employs ρ:

$$\frac{dR}{dt} = \frac{K_D}{R^2}\left(\frac{R}{R_c} - 1\right) = \frac{K_D}{R_c{}^2\rho^2}(\rho - 1)\text{a} \tag{C1}$$

and with the differential equation for $g_b(t)$ and $h_b(\rho)$:

$$\frac{\partial g(t)\rho^2 h(\rho)}{\partial t} = -g(t)\frac{1}{R_c}\frac{d}{d\rho}\left[\rho^2 h(\rho)\frac{K_D}{R_c{}^2\rho^2}(\rho - 1)\right] = -g(t)\frac{K_D}{R_c{}^3}\frac{d}{d\rho}[h(\rho)(\rho - 1)] \tag{C2}$$

The definition of ρ involves the time-dependent R_c, therefore ρ has a partial time-derivative:

$$\frac{\partial\rho}{\partial t} = \frac{\partial}{\partial t}\frac{R}{R_c} = -R\frac{1}{R_c^2}\frac{dR_c}{dt} = -\rho\frac{1}{3R_c{}^3}\frac{dR_c{}^3}{dt} \tag{C3}$$

Inserting the derivative $\partial\rho/\partial t$ into (C2) and simplifying yields the following:

$$\rho^2 h(\rho)\frac{R_c{}^3}{K_D}\frac{1}{g(t)}\frac{dg}{dt} = -\left[\frac{dh}{d\rho}(\rho - 1) + h - \left(\rho^3\frac{dh}{d\rho} + 2\rho^2 h(\rho)\right)\frac{1}{3K_D}\frac{dR_c{}^3}{dt}\right] \tag{C4}$$

To determine *g(t)* and eliminate it from the equation, we use the volume fraction of broadening crystals, which is a function of time as explained in Section 4.6.

$$\phi_b = \int_0^{2R_c}\frac{4\pi R^3}{3} f_b(R,t)dR = g_b(t)\frac{4\pi R_c^4}{3}\int_0^2 \rho^5 h_b(\rho)d\rho \tag{C5}$$

From it, we obtain a definition for the time-dependent portion of the distribution, *g(t)*:

$$g_b(t) = \frac{3\phi_b}{4\pi R_c^4\int_0^2 \rho^5 h_b(\rho)d\rho} \tag{C6}$$

This definition of *g(t)* is inserted explicitly into $R_c{}^3/K_D$ 1/*g dg/dt* in Eq. (C4).

$$\frac{R_c^3}{K_D}\frac{1}{g_b(t)}\frac{\partial g_b(t)}{\partial t} = \frac{R_c^3}{K_D}\frac{4\pi R_c^4\int_0^2\rho^5 h_b(\rho)d\rho}{3\phi_b}\left[\frac{3\phi_b}{4\pi\int_0^2\rho^5 h_b(\rho)d\rho}\frac{d}{dt}\frac{1}{R_c^4} + \frac{3}{4\pi R_c^4\int_0^2\rho^5 h_b(\rho)d\rho}\frac{d\phi_b}{dt}\right]$$

therefore

$$\frac{R_c^3}{K_D}\frac{1}{g_b(t)}\frac{\partial g_b(t)}{\partial t} = -\frac{4}{3K_D}\frac{dR_c^{\,3}}{dt} + \frac{R_c^3}{\phi_b K_D}\frac{d\phi_b}{dt} \tag{C7}$$

Now we define Z_b, the number concentration of nanocrystals in the broadening zone:

$$Z_b = \int_0^{2R_c} f_b(R,t)dR = R_c g(t)\int_0^2 \rho^2 h_b(\rho)d\rho \tag{C8}$$

The time-derivative of Z_b has two separate formulations: one where the time-derivative of the whole integral is taken and one where the fundamental theorem of calculus is applied to simplify out the integral.

$$\frac{d}{dt}\int_0^{2R_c} f_b(R,t)dR = \frac{d}{dt}\int_0^2 g_b(t)\rho^2 h_b(\rho)R_c d\rho = \frac{dg_b(t)R_c}{dt}\int_0^2 \rho^2 h_b(\rho)d\rho \tag{C9}$$

and

$$\begin{aligned}\frac{d}{dt}\int_0^{2R_c} f_b(R,t)dR &= f_b(2R_c,t)\frac{d(2R_c)}{dt} - f_b(0,t)\frac{d(0)}{dt} + \int_0^{2R_c}\frac{\partial f_b(R,t)}{\partial t}dR \\ &= 8g(t)h(2)\frac{dR_c}{dt} - g(t)\frac{K_D}{R_c^2}[h(2)+h(0)]\end{aligned} \tag{C10}$$

The two results are set equal to each other and Eq. (C7) is applied:

$$\left(\frac{dR_c^{\,3}}{dt} - \frac{R_c^{\,3}}{\phi_b}\frac{d\phi_b}{dt}\right) = -\frac{8h(2)}{\int_0^2 \rho^2 h(\rho)d\rho}\frac{1}{3}\frac{dR_c^{\,3}}{dt} + K_D\frac{h(2)+h(0)}{\int_0^2 \rho^2 h(\rho)d\rho} \tag{C11}$$

It is here that we define the dimensionless quantity $\Gamma(\xi)$, through the right-hand side of (C11):

$$\Gamma(\xi) = -\frac{8h(2)}{\int_0^2 \rho^2 h(\rho)d\rho}\frac{1}{3K_D}\frac{dR_c^{\,3}}{dt} + \frac{h(2)+h(0)}{\int_0^2 \rho^2 h(\rho)d\rho} \tag{C12}$$

Eq. (C11) resembles Wagner's derivation, except that the volume fraction and limits of integration are time-dependent and $h(2) \neq 0$. Combining (C7) with (C11) and (C12) yields:

$$\frac{R_c^3}{K_D}\frac{1}{g(t)}\frac{\partial g(t)}{\partial t} = -\frac{1}{3K_D}\frac{dR_c^{\,3}}{dt} - \Gamma(\xi) \tag{C13}$$

This result is now used in (C4) and consolidated:

$$\left[-\frac{1}{3K_D}\frac{dR_c^{\,3}}{dt}3\rho^2-\Gamma(\xi)\rho^2+1\right]h(\rho)+\left(\rho-1-\rho^3\frac{1}{3K_D}\frac{dR_c^{\,3}}{dt}\right)\frac{dh}{d\rho}=0 \tag{C14}$$

We have an expression for $dR_c^{\,3}/dt$ which we insert now:

$$\left[-\frac{3\xi}{(\xi+1)^3}\rho^2-\Gamma(\xi)\rho^2+1\right]h(\rho)+\left(\rho-1-\rho^3\frac{\xi}{(\xi+1)^3}\right)\frac{dh}{d\rho}=0 \tag{C15}$$

The second term has a zero near $\rho = 1$ for large ξ. That means that the first term must be zero at that point, or that $dh/d\rho$ is a delta function at that zero. Since $h(\rho)$ can't be zero anywhere (because we've presumed a monotonic function), we must find the value of $\Gamma(\xi)$ that makes the first term equal to zero as well for $\rho = \rho_{pole}$:

$$\begin{aligned}&-\frac{3\xi}{(\xi+1)^3}\rho_{pole}^{\,2}-\Gamma(\xi)\rho_{pole}^{\,2}+1=0\\&\Gamma(\xi)=-\frac{3\xi}{(\xi+1)^3}+\frac{1}{\rho_{pole}^2}\end{aligned} \tag{C16}$$

The solution of ρ_{pole} is cubic and too complicated to list here, though it is always just above 1 for large ξ and maxes out at $\rho_{pole} = 3/2$ when $\xi = ½$. Restating the differential equation yields:

$$\frac{\frac{\rho^2}{\rho_{pole}^2}-1}{\rho-1-\rho^3\frac{\rho_{pole}-1}{\rho_{pole}^3}}=\frac{d\ln h}{d\rho} \tag{C17}$$

Analysis by L'Hospital's rule shows the function is continuous and non-divergent at $\rho = \rho_{pole}$:

$$\lim_{\rho\to\rho_{pole}}\frac{\frac{\rho^2}{\rho_{pole}^2}-1}{\rho-1-\rho^3\frac{\rho_{pole}-1}{\rho_{pole}^3}}=\lim_{\rho\to\rho_{pole}}\frac{\frac{2\rho}{\rho_{pole}^2}-1}{1-3\rho^2\frac{\rho_{pole}-1}{\rho_{pole}^3}}=\frac{2-\rho_{pole}}{1-2\rho_{pole}} \tag{C18}$$

We may now split (C17) using partial fractions and integrate the result:

$$\frac{\frac{\rho^2}{\rho_z^{\,2}}-1}{\rho-1-\rho^3\frac{\rho_z-1}{\rho_z^{\,3}}}=-\frac{\frac{1}{2}+\frac{\rho}{\rho_z}}{-1+\left(\frac{\rho}{\rho_z}+\frac{\rho^2}{\rho_z^{\,2}}\right)(\rho_z-1)}-\frac{\frac{1}{2}}{-1+\left(\frac{\rho}{\rho_z}+\frac{\rho^2}{\rho_z^{\,2}}\right)(\rho_z-1)} \tag{C19}$$

The first term can be integrated with *u*-substitution:

$$-\int \frac{\frac{1}{2}+\frac{\rho}{\rho_z}}{-1+\left(\frac{\rho}{\rho_z}+\frac{\rho^2}{\rho_z^{\,2}}\right)(\rho_z-1)}\,d\rho = \frac{\rho_z}{2(\rho_z-1)}\int\frac{du}{u} \qquad (C20)$$

$$= -\frac{\rho_z}{2(\rho_z-1)}\ln\left(\left|-1+\left(\frac{\rho}{\rho_z}+\frac{\rho^2}{\rho_z^{\,2}}\right)(\rho_z-1)\right|\right)$$

and the second term

$$\begin{bmatrix} u=\sqrt{\left(1+2\frac{\rho}{\rho_z}\right)^2\frac{(\rho_z-1)}{(\rho_z+3)}}=\left(1+2\frac{\rho}{\rho_z}\right)\sqrt{\frac{(\rho_z-1)}{(\rho_z+3)}} \\ du=\frac{2}{\rho_z}\sqrt{\frac{(\rho_z-1)}{(\rho_z+3)}}d\rho \end{bmatrix}$$

$$-\int \frac{\frac{1}{2}}{-1+\left(\frac{\rho}{\rho_z}+\frac{\rho^2}{\rho_z^{\,2}}\right)(\rho_z-1)} = \frac{\rho_z}{\sqrt{(\rho_z+3)(\rho_z-1)}}\int \frac{\frac{2}{\rho_z}\sqrt{\frac{\rho_z-1}{\rho_z+3}}}{\left[1-\left(1+2\frac{\rho}{\rho_z}\right)^2\frac{(\rho_z-1)}{(\rho_z+3)}\right]}d\rho \qquad (C21)$$

$$= \frac{\rho_z}{\sqrt{(\rho_z+3)(\rho_z-1)}}\int\frac{du}{[1-u^2]} = \frac{\rho_z}{\sqrt{(\rho_z+3)(\rho_z-1)}}\tanh^{-1}(u)$$

$$= \frac{\rho_z}{\sqrt{(\rho_z+3)(\rho_z-1)}}\tanh^{-1}\left(\left(1+2\frac{\rho}{\rho_z}\right)\sqrt{\frac{(\rho_z-1)}{(\rho_z+3)}}\right)$$

therefore:

$$\ln h = \begin{bmatrix} -\frac{\rho_z}{2(\rho_z-1)}\ln\left(1-\left(\frac{\rho}{\rho_z}+\frac{\rho^2}{\rho_z^{\,2}}\right)(\rho_z-1)\right) \\ \frac{\rho_z}{\sqrt{(\rho_z+3)(\rho_z-1)}}\tanh^{-1}\left(\left(1+2\frac{\rho}{\rho_z}\right)\sqrt{\frac{\rho_z-1}{\rho_z+3}}\right) \end{bmatrix} \qquad (C22)$$

When the exponential is taken, the logarithmic term is easily addressed. To simplify the $\tanh^{-1}$ we make use of the identity $\exp(\tanh^{-1}(x)) = [(1+x)/(1-x)]^{½}$ to obtain:

$$h = C_h\left(1-\left(\frac{\rho}{\rho_z}+\frac{\rho^2}{\rho_z{}^2}\right)(\rho_z-1)\right)^{-\frac{\rho_z}{2(\rho_z-1)}}\left(\frac{1+\left(1+2\frac{\rho}{\rho_z}\right)\sqrt{\frac{\rho_z-1}{\rho_z+3}}}{1-\left(1+2\frac{\rho}{\rho_z}\right)\sqrt{\frac{\rho_z-1}{\rho_z+3}}}\right)^{\frac{1}{2}\frac{\rho_z}{\sqrt{(\rho_z+3)(\rho_z-1)}}} \tag{C23}$$

For extremely small $1-\rho_{pole}$, we can expand this expression:

1st term:

$$\begin{aligned}\left(1-\left(\frac{\rho}{\rho_z}+\frac{\rho^2}{\rho_z{}^2}\right)(\rho_z-1)\right)^{-\frac{\rho_z}{2(\rho_z-1)}} &= \exp\left(\left(-\frac{\rho_z}{2(\rho_z-1)}\right)\ln\left[1-\left(\frac{\rho}{\rho_z}+\frac{\rho^2}{\rho_z{}^2}\right)(\rho_z-1)\right]\right)\\ &\approx \exp\left(\left(-\frac{\rho_z}{2(\rho_z-1)}\right)\left[-\left(\frac{\rho}{\rho_z}+\frac{\rho^2}{\rho_z{}^2}\right)(\rho_z-1)\right]\right) = \exp\left(\frac{\rho}{2}\left(1+\frac{\rho}{\rho_z}\right)\right)\end{aligned} \tag{C24}$$

2nd term:

$$\begin{aligned}\left(\frac{1+\left(1+2\frac{\rho}{\rho_z}\right)\sqrt{\frac{\rho_z-1}{\rho_z+3}}}{1-\left(1+2\frac{\rho}{\rho_z}\right)\sqrt{\frac{\rho_z-1}{\rho_z+3}}}\right)^{\frac{1}{2}\frac{\rho_z}{\sqrt{(\rho_z+3)(\rho_z-1)}}} &= \exp\left(\ln\left[\frac{1+\left(1+2\frac{\rho}{\rho_z}\right)\sqrt{\frac{\rho_z-1}{\rho_z+3}}}{1-\left(1+2\frac{\rho}{\rho_z}\right)\sqrt{\frac{\rho_z-1}{\rho_z+3}}}\right]\left(\frac{1}{2}\frac{\rho_z}{\sqrt{(\rho_z+3)(\rho_z-1)}}\right)\right)\\ &\approx \exp\left(\left[\left(1+\frac{2\rho}{\rho_z}\right)\sqrt{\frac{\rho_z-1}{\rho_z+3}}\right]\left(\frac{\rho_z}{\sqrt{(\rho_z+3)(\rho_z-1)}}\right)\right) = \exp\left(\left(1+2\frac{\rho}{\rho_z}\right)\frac{\rho_z}{(\rho_z+3)}\right)\end{aligned} \tag{C25}$$

Therefore a large-ξ approximation to the distribution is:

$$h(\rho) \approx C_h \exp\left(\frac{\rho}{2}\left(1+\frac{\rho}{\rho_z}\right)+\left(1+2\frac{\rho}{\rho_z}\right)\frac{1}{\rho_z+3}\right) \tag{C26}$$

This is a much more tractable form of the equation for $h(\rho)$, but the %error of this expansion versus the full expression grows as $\sim 13(1-\rho_z)$, and for any $\xi < 20$ is too inaccurate to use. Since experimental values of ξ are likely to be less than 20, which is perfectly able to cause size focusing, the approximation is good only for qualitative analysis.

APPENDIX D: SUPPLEMENTAL DERIVATIONS OF SURFACTANT-MEDIATED GROWTH

The Single-Particle Growth Rate

The two concentration profiles $c_0(r)$ and $c_1(r)$ are defined by the Laplace differential equation, which has a known solution. Therefore, the two profiles are

$$\begin{aligned} c_1 &= a_1 + \frac{b_1}{r} \\ c_0 &= a_0 + \frac{b_0}{r} \end{aligned} \tag{D1}$$

The four boundary conditions are given in Chapter 5, Section 1.

$$\begin{aligned} &c_1(r \to \infty) = c_b \\ &D_0\left[\frac{\partial c_0}{\partial r}\right]_R = k_s\left(c_0(R) - c_\infty e^{2\gamma/RkT}\right) \\ &c_1(R+\delta) = K_P c_0(R+\delta) \\ &D_1\left[\frac{\partial c_1}{\partial r}\right]_{R+\delta} = D_0\left[\frac{\partial c_0}{\partial r}\right]_{R+\delta} \end{aligned} \tag{D2}$$

Inserting the preliminary solutions for c_1 and c_0, including integration constants, in the boundary conditions yields:

$$\begin{aligned} &c_b = a_1 \\ &-D_0\frac{b_0}{R^2} = k_s\left(a_0 + \frac{b_0}{R} - c_\infty e^{2\gamma/RkT}\right) \\ &c_b + \frac{b_1}{R+\delta} = K_P a_0 + \frac{K_P b_0}{R+\delta} \\ &-D_1\frac{b_1}{(R+\delta)^2} = -D_0\frac{b_0}{(R+\delta)^2} \end{aligned} \tag{D3}$$

Using algebraic replacements, it is easy to determine the constants a_0 and b_0, which are needed for the single-particle growth rate:

$$a_0 = \frac{c_b}{K_P} + \left(\frac{D_0}{K_P D_1} - 1\right)\frac{b_0}{R+\delta}$$
$$b_0 = -\frac{\left(\frac{c_b}{K_P} - c_\infty e^{2\gamma/RkT}\right)}{\left(\frac{D_0}{k_s R}+1\right)\frac{1}{R} + \left(\frac{D_0}{K_P D_1} - 1\right)\frac{1}{R+\delta}} \quad \text{(D4)}$$

These constants are used to calculate $[c_0(R) - e^{2\gamma/RkT}]$ in the single-particle growth rate:

$$\left(c_0(R) - c_\infty e^{2\gamma/RkT}\right) = \left(\frac{c_b}{K_P} - e^{2\gamma/RkT}\right)\left[1 - \frac{\frac{1}{R} + \left(\frac{D_0}{K_P D_1} - 1\right)\frac{1}{R+\delta}}{\left(\frac{D_0}{k_s R}+1\right)\frac{1}{R} + \left(\frac{D_0}{K_P D_1} - 1\right)\frac{1}{R+\delta}}\right]$$
$$\left(c_0(R) - c_\infty e^{2\gamma/RkT}\right) = \frac{D_0}{k_s R}\left[\frac{\left(\frac{c_b}{K_P} - e^{2\gamma/RkT}\right)}{\left(\frac{D_0}{k_s R}+1\right) + \left(\frac{D_0}{K_P D_1} - 1\right)\frac{R}{R+\delta}}\right] \quad \text{(D5)}$$

Therefore, the fully accurate single-particle growth rate for a sphere, suspended in a solution with bulk concentration c_b, surrounded by a layer of thickness δ bearing different transport properties than the bulk, is as follows:

$$\frac{dR}{dt} = \nu\frac{D_0}{R}\frac{\left(\frac{c_b}{K_P} - e^{2\gamma/RkT}\right)}{\left(\frac{D_0}{k_s R}+1\right) + \left(\frac{D_0}{K_P D_1} - 1\right)\frac{R}{R+\delta}} \quad \text{(D6)}$$

This model presumed that the diffusivity and permeability of the surfactant layer are constant throughout the layer, neglecting the fact that the density profile of surfactant monomers is likely varies with *r*.

Detailed derivation of h(ρ)

Eq. (5.23) in Chapter 4 gives the ordinary differential equation for $h(\rho)$:

$$\left(\frac{\rho^3}{3\gamma_D} - \frac{\rho-1}{1+\eta\frac{\rho}{\rho+\delta'}}\right)\frac{dh}{d\rho} = h(\rho)\left[-\frac{6}{3\gamma_D}\rho^2 + \frac{1}{1+\eta\frac{\rho}{\rho+\delta'}} - \frac{\rho-1}{1+\eta\frac{\rho}{\rho+\delta'}}\frac{\eta\delta'}{(\rho+\delta')^2\left(1+\eta\frac{\rho}{\rho+\delta'}\right)}\right] \quad \text{(D7)}$$

In solving this differential equation, it is necessary to note the behavior of the prefactor to $dh/d\rho$ on the left-hand side.

$$\frac{\rho-1}{1+\eta\dfrac{\rho}{\rho+\delta'}}-\frac{\rho^3}{3\gamma_D} \tag{D8}$$

Using the insight of Kahlweit, we find that this expression is within a constant of the dimensionless single-particle growth rate $d\rho^3/dt$, which incorporates both dR/dt and dR_c/dt. This function $d\rho^3/dt = 0$ at some finite point(s) $\rho = \rho_{pole}$, such that any particle at $\rho = \rho_{pole}$ remains at $\rho = \rho_{pole}$ for some time. In an open (infinite) system where $f(R,t)$ is truly continuous, this persists indefinitely. In a closed system, the final state of the whole system is one large macroscopic phase of size $\rho = 1$. Therefore, all particles will eventually decrease in size and a particle at $\rho = \rho_{pole}$ has reached its maximum ρ-value. Separately, if $d\rho^3/dt$ equals zero at $\rho = \rho_{pole}$, then the left-hand side of the differential equation for h is also zero $\rho = \rho_{pole}$, which in turn implies that $h(\rho_{pole})$ must also be zero. The form of h thus confirms the physical argument that ρ_{pole} represents the maximum possible ρ-value.

We again employ an argument by Kahlweit and take the ρ-derivative of $d\rho^3/dt$, i.e. $d/d\rho\,(d\rho^3/dt)$. Setting this relation to zero will solve for the fastest-growing particle in the system. Because $d\rho^3/dt$ monotonically increases with ρ for all $\rho < \rho_{pole}$ regardless of γ_D, the fastest-growing particle is also the largest particle in the system. As a result, $d/d\rho\,(d\rho^3/dt) = 0$ at $\rho = \rho_{pole}$. Combining this with the definition of ρ_{pole} given by $d\rho^3/dt = 0$ yields the two equations needed to solve for ρ_{pole} and γ_D, as follows:

$$\begin{aligned}
&\frac{\rho_{pole}^3}{3\gamma_D}-\frac{\rho_{pole}-1}{1+\eta\frac{\rho_{pole}}{\rho_{pole}+\delta'}}=0\\
&\frac{\rho_{pole}^2}{\gamma_D}-\frac{1}{1+\eta\frac{\rho_{pole}}{\rho_{pole}+\delta'}}+\frac{\left(\rho_{pole}-1\right)}{\left(1+\eta\frac{\rho_{pole}}{\rho_{pole}+\delta'}\right)^2}\frac{\eta\delta'}{\left(\rho_{pole}+\delta'\right)^2}=0
\end{aligned} \tag{D9}$$

It is trivial to eliminate γ_D and construct an equation for ρ_{pole} only:

$$3\left(\frac{\rho_{pole}-1}{\rho_{pole}}\right)-1+\left(\frac{\rho_{pole}-1}{\rho_{pole}}\right)\frac{\eta\delta'}{\left(1+\eta\frac{\rho_{pole}}{\rho_{pole}+\delta'}\right)\left(\rho_{pole}+\delta'\right)^2}=0 \tag{D10}$$

The exact solution for ρ_{pole} comes from the cubic equation, which involves imaginary computations and dozens of terms. Such a form is not useful in establishing the relevant physics of the Ostwald ripening system, so we make an approximation. For $\eta\delta = 0$, the solution is exactly $\rho_{pole} = 3/2$ and $\gamma_D = 9/4$, just as in LSW theory. Therefore, let ρ_{pole} be replaced by 3/2 in certain key places in the above equation to facilitate a first-order accurate solution to ρ_{pole}:

$$3\left(\frac{\rho_{pole}-1}{\rho_{pole}}\right)-1+\left(\frac{\rho_{pole}-1}{\rho_{pole}}\right)\frac{\eta\delta'^{\frac{3}{2}}}{\left(1+\eta^{\frac{\frac{3}{2}}{\frac{3}{2}+\delta'}}\right)\left(\frac{3}{2}+\delta'\right)^2}=0 \tag{D11}$$

therefore

$$\rho_{pole}\approx\frac{3+\frac{\eta\delta'^{\frac{3}{2}}}{\left(1+\eta^{\frac{\frac{3}{2}}{\frac{3}{2}+\delta'}}\right)\left(\frac{3}{2}+\delta'\right)^2}}{2+\frac{\eta\delta'^{\frac{3}{2}}}{\left(1+\eta^{\frac{\frac{3}{2}}{\frac{3}{2}+\delta'}}\right)\left(\frac{3}{2}+\delta'\right)^2}} \tag{D12}$$

This approximation is accurate to within order $\eta^2\delta^2$. Values obtained by this formula are within 5×10^{-5} of numerical solutions for $-¼ < \eta < ¼$ and within 5×10^{-4} for $-½ < \eta < 1$. The approximate formula for γ_D that employs this version of ρ_{pole} is:

$$\gamma_D=\left(1+\eta^{\frac{\frac{3}{2}}{\frac{3}{2}+\delta'}}\right)\frac{1}{3}\frac{\left(3+\frac{\eta\delta'^{\frac{3}{2}}}{\left(1+\eta^{\frac{\frac{3}{2}}{\frac{3}{2}+\delta'}}\right)\left(\frac{3}{2}+\delta'\right)^2}\right)^3}{\left(2+\frac{\eta\delta'^{\frac{3}{2}}}{\left(1+\eta^{\frac{\frac{3}{2}}{\frac{3}{2}+\delta'}}\right)\left(\frac{3}{2}+\delta'\right)^2}\right)^2} \tag{D13}$$

Note the generic Taylor expansion $(3+x)^3/(2+x)^2 \approx 27/4 + 9/16x^2 + O(x^3)$, and here x is the $\eta\delta$ term in the numerator and denominator of γ_D. The maximum possible value for this term is $\eta/4$, thus for any $|\eta| < 1$, γ_D should obey the following approximation.

$$\gamma_D=\frac{9}{4}\left(1+\eta^{\frac{\frac{3}{2}}{\frac{3}{2}+\delta'}}\right) \tag{D14}$$

Comparison with numerical solutions to γ_D and ρ_{pole} shows that this simple expression for γ_D is within 1% error of the numerical answer. This accuracy is marginally increased if the 3/2 terms are *post facto* replaced by ρ_{pole}. Therefore, we have the following closed-form expression for the differential equation of h:

$$\frac{d\ln h}{d\rho}=\frac{-\frac{24}{27\left(1+\eta^{\frac{\rho_{pole}}{\rho_{pole}+\delta'}}\right)}\rho^2+\frac{1}{1+\eta^{\frac{\rho}{\rho+\delta'}}}-\frac{\rho-1}{1+\eta^{\frac{\rho}{\rho+\delta'}}}\frac{\eta\delta'}{(\rho+\delta')^2\left(1+\eta^{\frac{\rho}{\rho+\delta'}}\right)}}{\frac{4\rho^3}{27\left(1+\eta^{\frac{\rho_{pole}}{\rho_{pole}+\delta'}}\right)}-\frac{\rho-1}{1+\eta^{\frac{\rho}{\rho+\delta'}}}} \tag{D15}$$

This is Eq. (5.26) in Chapter 5. The numerator of this expression can be separated into two pieces to yield the following:

$$\frac{d\ln h}{d\rho}=-\frac{\frac{d}{d\rho}\left[\frac{4\rho^3}{27\left(1+\eta\frac{\rho_{pole}}{\rho_{pole}+\delta'}\right)}-\frac{\rho-1}{1+\eta\frac{\rho}{\rho+\delta'}}\right]}{\frac{4\rho^3}{27\left(1+\eta\frac{\rho_{pole}}{\rho_{pole}+\delta'}\right)}-\frac{\rho-1}{1+\eta\frac{\rho}{\rho+\delta'}}}+\frac{-\frac{12}{27}\rho^2}{\frac{4\rho^3}{27}-(\rho-1)\frac{1+\eta\frac{\rho_{pole}}{\rho_{pole}+\delta'}}{1+\eta\frac{\rho}{\rho+\delta'}}} \tag{D16}$$

The first term is easily integrable, but the second term is intractable without an approximation. Let us simplify the second term on the right by declaring that the denominator does not depend on η and simply removing that term. This is the least robust approximation made so far, introducing error on the order of $|\eta(\rho_{pole}-\rho)|$. To capture the nature of the error introduced through this approximation, we calculate the first-order η-perturbation of the second term in Eq. (5.26) and then integrate to obtain the following:

$$\begin{aligned}\ln h = C-\frac{4}{3}\ln(\rho+3)-\frac{\frac{3}{2}}{\frac{3}{2}-\rho}-\frac{5}{3}\ln\left(\frac{3}{2}-\rho\right)-\ln\left(\frac{4\rho^3}{27\left(1+\eta\frac{\rho_{pole}}{\rho_{pole}+\delta'}\right)}-\frac{\rho-1}{1+\eta\frac{\rho}{\rho+\delta'}}\right)\\ -\frac{12}{27}\left(\frac{\eta\delta'}{1+\eta\frac{\rho_{pole}}{\rho_{pole}+\delta'}}\right)\left[\frac{3(\delta'+1)}{(\delta'-3)^2}\ln(\rho+3)-\frac{243}{8}\frac{\delta'^3(\delta'+1)}{(\delta'-3)^2\left(\delta'+\frac{3}{2}\right)^3}\ln(\rho+\delta')-\frac{3}{8}\frac{(\delta'+1)(8\delta'+3)}{\left(\delta'+\frac{3}{2}\right)^3}\ln\left(\frac{3}{2}-\rho\right)\right.\\ \left.+\frac{\left(\frac{3}{2}\right)^3\left[\rho^2\left(5\delta'^2+8\delta'+3\right)-\frac{1}{4}\left(\frac{3}{2}\right)\rho\left(22\delta'^2+97\delta'+87\right)+\frac{1}{2}\left(\frac{3}{2}\right)^2\left(2\delta'^2+31\delta'+33\right)\right]}{(3-\delta')\left(\frac{3}{2}+\delta'\right)^2(3+\rho)\left(\frac{3}{2}-\rho\right)^2}\right]\end{aligned} \tag{D17}$$

Note that the first three terms are found in the classical LSW derivation. In fact, by adding and subtracting a term $\ln(4\rho^3/27-\rho+1)=\ln(^4/_{27})+\ln(\rho+3)+2\ln(^3/_2-\rho)$, the exact LSW distribution is recovered and this is the reason for its appearance in Eq. (5.27) in Chaper 5. The $\eta\delta$-term is reduced by declaring $\delta'=1$ to the following:

$$\begin{aligned}\ln h = \ln\left(\frac{\frac{4\rho^3}{27}-(\rho-1)}{\frac{4\rho^3}{27\left(1+\eta\frac{\rho_{pole}}{\rho_{pole}+\delta'}\right)}-\frac{\rho-1}{1+\eta\frac{\rho}{\rho+\delta'}}}\right)+\left(\frac{6}{5}\right)^3\left(\frac{\eta\delta'}{1+\eta\frac{\rho_{pole}}{\rho_{pole}+\delta'}}\right)\ln\left(\frac{\rho+\delta'}{\delta'}\right)\\ +\left(\frac{7}{3}+\frac{2}{3}\frac{\eta\delta'}{1+\eta\frac{\rho_{pole}}{\rho_{pole}+\delta'}}\right)\ln\left(\frac{3}{3+\rho}\right)+\left(\frac{11}{3}-\frac{\eta\delta'}{1+\eta\frac{\rho_{pole}}{\rho_{pole}+\delta'}}\right)\ln\left(\frac{\frac{3}{2}}{\frac{3}{2}-\rho}\right)\\ -\frac{\rho}{\frac{3}{2}-\rho}+\left(\frac{6}{5}\right)^2\left(\frac{\eta\delta'}{1+\eta\frac{\rho_{pole}}{\rho_{pole}+\delta'}}\right)\frac{\rho}{\rho+3}+O\left\{\left(\frac{\eta\frac{\rho_{pole}}{\rho_{pole}+\delta'}-\eta\frac{\rho}{\rho+\delta'}}{1+\eta\frac{\rho_{pole}}{\rho_{pole}+\delta'}}\right)^2\right\}\end{aligned} \tag{D18}$$

The perturbations to the ln(3/(3+ρ)) and ln(3/(3+ρ)) terms both diminish the value of *h*, while the new ln(ρ/δ + 1) term and ρ/(3+ρ) term raise *h*. Numerical analysis for various values of η and δ reveal that in general, completely neglecting the $\eta\delta$ term in the integration yields a second-order accurate approximation to the full solution. Thus, we are justified in keeping Eq. (5.27) in its current form.

APPENDIX E: DETAILED EQUATIONS & IMPLEMENTATION OF SCMF THEORY

As noted in the main text, the surfactant chains on the surface of a nanocrystal with *n* crystal monomers and *m* grafted surfactant chains can exhibit a set of conformations $\{\alpha\}$. These conformations are assumed to be globally applicable to all surfactants, i.e. every surface has the same set $\{\alpha\}$ representing the possible conformations of a single chain. The different conformations all interact with each other, with the solvent, and with the nanocrystal core. From these interactions, a probability distribution function $P_g(\alpha : n,m)$ can be defined as follows:

$$P_g(\alpha : n,m) = \frac{1}{q_g}\exp\left\{\begin{array}{l} -\beta u_{\text{int}}(\alpha) + \int_{V_{n,m}} d\vec{r}\,\ln\left(\frac{\phi_s(\vec{r} : n,m)}{N_{solv}/N_{total}}\right) n_g(\vec{r},\alpha)\frac{v_P}{v_s} \\ -\frac{\beta\omega_{TT}}{2}\iint_{V_{n,m}} d\vec{r}\,d\vec{r}\,'\left|\frac{\Theta(|\vec{r}-\vec{r}\,'|-l)l}{\vec{r}-\vec{r}\,'}\right|^6 \left[\rho_g(\vec{r}\,')n_g(\vec{r},\alpha)+\rho_g(\vec{r})n_g(\vec{r}\,',\alpha)\right] \end{array}\right\}$$

with the following definitions:

$u_{int}(\alpha)$	the internal energy of chain conformation α, including gauche bonds, etc.
$\phi_s(\mathbf{r})$	the space-varying function for the solvent volume fraction
$n_g(\mathbf{r},\alpha)$	for conformation α, the number of monomers located at **r** (delta functions)
$\Theta(x)$	a step function in x, where $\Theta = 1$ for $x > 0$ and $\Theta = 0$ for $x < 0$
$\rho_g(\mathbf{r})$	the local density of chain monomers at location **r**, averaged over α
v_P, v_s	the volume of a chain monomer and a solvent molecule, respectively
l	the length of a bond within the chain Also, for $r < l$, the interaction between monomers is zero
ω_{TT}	the interaction strength between chain monomers ("Tail-Tail" interaction)
q_g	the grafted chain partition function, defined such that $\Sigma P_g(\alpha) = 1$

The definition of $P_g(\alpha : n,m)$ resulted from the minimization of the free energy functional given in the main text as Eq. (6.9). The portion of the free energy that depends only on the chains and their Boltzmann-weighted probabilities is defined as follows:

$$\begin{aligned} \beta F_{nm} &= m\sum_{\{\alpha\}} P_g(\alpha : n,m)\left[\ln P_g(\alpha : n,m) + \beta u_{\text{int}}(\alpha)\right] \\ &+ \frac{\beta\omega_{TT}}{2}\iint_{V_{n,m}} d\vec{r}\,d\vec{r}\,'\left[m\sum_{\{\alpha\}} P_g(\alpha : n,m)n_g(\vec{r},\alpha)\right]\left|\frac{\Theta(|\vec{r}-\vec{r}\,'|-l)l}{\vec{r}-\vec{r}\,'}\right|^6\left[m\sum_{\{\alpha'\}} P_g(\alpha' : n,m)n_g(\vec{r}\,',\alpha')\right] \\ &+ \int_{V_{n,m}} d\vec{r}\,\frac{1}{v_s}\phi_s(\vec{r} : n,m)\ln(\phi_s(\vec{r} : n,m)) \end{aligned}$$

Using the definition of $P_g(\alpha : n,m)$, the expression for βF_{nm} can be reduced. We also employ a change of variables (as in the main text) from *n* and *m* to the nanocrystal radius *R* and the surface grafting density σ, to obtain:

$$\beta F_{nm} = -4\pi R^2 \sigma \ln\frac{q_g}{q_f} + \int_{V_{n,m}} d\vec{r}\,\frac{1}{v_s}\ln\left(\phi_s(\vec{r}:n,m)\right) - \frac{\beta\omega_{TT}}{2}\iint_{V_{n,m}} d\vec{r}\,d\vec{r}\,'\left[\frac{1-\phi_s(\vec{r})}{v_P}\right]X(\vec{r},\vec{r}\,')\left[\frac{1-\phi_s(\vec{r}\,')}{v_P}\right]$$

where q_f is the partition function of a free chain, which has a larger set of conformations but much weaker monomer-monomer interactions. Note the monomer-monomer attraction potential has been reduced to $X(\mathbf{r},\mathbf{r}')$ for convenience. The derivative of this function with respect to σ is simple to evaluate because the limits of integration do not vary with σ (they depend only on R) and the interaction function $X(\mathbf{r},\mathbf{r}')$ does not vary with σ.

$$\left(\frac{\partial\beta F_{nm}}{\partial\sigma}\right)_R = -4\pi R^2 \ln\frac{q_g}{q_f} - 4\pi R^2\sigma\frac{1}{q_g}\frac{\partial q_g}{\partial\sigma} + \int_{V_{n,m}} d\vec{r}\,\frac{1}{v_s}\frac{1}{\phi_s(\vec{r})}\frac{\partial\phi_s(\vec{r})}{\partial\sigma} + \frac{\beta\omega_{TT}}{2v_P}\iint_{V_{n,m}} d\vec{r}\,d\vec{r}\,'\left[\frac{1-\phi_s(\vec{r})}{v_P}\right]\left[X(\vec{r},\vec{r}\,') + X(\vec{r}\,',\vec{r})\right]\frac{\partial\phi_s(\vec{r}\,')}{\partial\sigma}$$

where the σ-derivative of ϕ_s is given by the incompressibility constraint, and the derivative of q_g is given through the definition of $P_g(\alpha:n,m)$:

$$\frac{\partial\phi_s(\vec{r})}{\partial\sigma} = -4\pi R^2\sum_{\{\alpha\}} P_g(\alpha:n,m)n_g(\vec{r},\alpha)v_P - 4\pi R^2\sigma\sum_{\{\alpha\}} P_g(\alpha)\frac{\partial\ln\left[q_g P_g(\alpha)\right]}{\partial\sigma}n_g(\vec{r},\alpha)v_P$$

$$4\pi R^2\sigma\frac{1}{q_g}\frac{\partial q_g}{\partial\sigma} = 4\pi R^2\sigma\sum_{\{\alpha\}} P(\alpha)\frac{\partial\ln\left[q_g P_g(\alpha)\right]}{\partial\sigma}$$

More $d\phi_s/d\sigma$ terms appears in the derivative of $\ln[q_g P_g(\alpha)]$, but almost all of those terms cancel in the total calculation, to finally yield this expression:

$$\left(\frac{\partial\beta F_{nm}}{\partial\sigma}\right)_R = -4\pi R^2\ln\frac{q_g}{q_f} - \int_{V_{n,m}} d\vec{r}\,\frac{1}{v_s}\frac{\partial\phi_s(\vec{r})}{\partial\sigma} + \frac{1}{\sigma}\int_{V_{n,m}} d\vec{r}\,\frac{1}{v_s}\ln\phi_s(\vec{r}) - \frac{1}{\sigma}\frac{\beta\omega_{TT}}{2v_P{}^2}\iint_{V_{n,m}} d\vec{r}\,d\vec{r}\,'(1-\phi_s(\vec{r}))X(\vec{r},\vec{r}\,')(1-\phi_s(\vec{r}\,'))$$

The final simplification involves the incompressibility constraint and the product rule of differentiation, including a new parameter, the change length $L = \int n_g(\mathbf{r},\alpha)d\mathbf{r}$.

$$\int_{V_{n,m}} d\vec{r}\,\frac{1}{v_s}\frac{\partial\phi_s(\vec{r})}{\partial\sigma} = \frac{1}{v_s}\frac{\partial}{\partial\sigma}\underbrace{\int_{V_{n,m}} d\vec{r}\,\phi_s(\vec{r})}_{V_{nm}-4\pi R^2\sigma L v_P} - \left[\phi_s(\vec{r})\right]_{\partial V_{nm}}\underbrace{\frac{\partial V_{nm}}{\partial\sigma}}_{0} = 4\pi R^2\frac{L v_P}{v_s}$$

Therefore, the σ-derivative of βF_{nm} is entirely evaluable using quantities already defined through SCMF theory:

$$\frac{\partial \beta F_{nm}}{\partial \sigma} = -4\pi R^2 \left[\frac{L v_P}{v_s} + \ln q_g \right]$$

Using similar methods, the R-derivative of βF_{nm} can also be determined.

$$\left(\frac{\partial F}{\partial R} \right)_\sigma = -8\pi R \sigma \ln \frac{q_g}{q_f} - 4\pi R^2 \sigma \frac{1}{q_g} \frac{\partial q_g}{\partial R} + \frac{1}{v_s} \frac{\partial}{\partial R} \int_{V_{nm}} d\vec{r} \ln \phi_s(\vec{r}) - \frac{\beta \omega_{TT}}{2 v_P^2} \frac{\partial}{\partial R} \int_{V_{nm}} d\vec{r} \int_{V_{nm}} d\vec{r}' [1 - \phi_s(\vec{r})] X(\vec{r}, \vec{r}') [1 - \phi_s(\vec{r}')]$$

The R-derivative of q_g also contains the R-derivatives of the same volume integrals, many of which cancel out. The result for the derivative is:

$$\left(\frac{\partial F}{\partial R} \right)_\sigma = -8\pi R \sigma \ln \frac{q_{g,nm}}{q_f} + \frac{1}{v_s} \int_{\partial V_{nm}} d\vec{s}\, \phi_s(\vec{s}) [\ln \phi_s(\vec{s}) - 1] + \frac{\beta \omega_{TT}}{2 v_P^2} \int_{V_{nm}} d\vec{r} \int_{V_{nm}} d\vec{r}' [1 - \phi_s(\vec{r})] \frac{\partial X(\vec{r}, \vec{r}')}{\partial R} [1 - \phi_s(\vec{r}')]$$

The final formulation of Eq. (6.26) is therefore defined as follows:

$$\frac{R_{eq}}{2} \left[\frac{1}{v_s} \int_{\partial V_{nm}} d\vec{s}\, \phi_s(\vec{s}) [\ln \phi_s(\vec{s}) - 1] + \frac{\beta \omega_{TT}}{2 v_P^2} \int_{V_{nm}} d\vec{r} \int_{V_{nm}} d\vec{r}' [1 - \phi_s(\vec{r})] \frac{dX(\vec{r}, \vec{r}')}{dR} [1 - \phi_s(\vec{r}')] \right] + 4\pi R_{eq}^2 \beta \gamma = 0$$

In the "collapsed surfactant" limit, we presume that the surfactants' monomer-monomer attractions are sufficiently strong to completely collapse all the conformations to form a nearly solid-like layer of monomers around the core. Thus, $\phi_s(\mathbf{r})$ is presumed very small near the nanocrystal core and experiences a step-change rise to $\phi_s(\mathbf{r}) = 1$ outside the solid-like layer. In both cases, $\phi_s \ln \phi_s = 0$ and the monomer-monomer attractions are zero outside the solid-like layer. The volume of the solid-like layer is equal to the total volume of monomers, mLv_P. Therefore, the reformulation of Eq. (6.26) reduces to the following:

$$\frac{\beta \omega_{TT}}{2 v_P^2} mL v_P \frac{R_{eq}}{2} \int_{V_{nm}} d\vec{r}' \frac{dX\left(\langle \vec{r} \rangle_{mLv_P}, \vec{r}' \right)}{dR} = -4\pi R_{eq}^2 \beta \gamma$$

Numerical analysis indicates that the product of $R/2v_P$ and the volume-integral of dX/dR is constant with R, therefore

$$\beta\omega_{TT}\left(4\pi R_{eq}^2\right)\sigma L\frac{K}{2}=-4\pi R_{eq}{}^2\beta\gamma$$

The value of σ cannot be higher than $\sigma_{\max}$ and the largest value that $\beta\gamma$ can possess is $\beta\gamma_{crit}$, therefore we have our scaling law:

$$\beta\omega_{TT}\sigma_{\max}L\propto-\beta\gamma_{crit}$$

NUMERICAL FRAMEWORK

Although SCMF theory is stated in terms of integrals and continuous functions, it is intractable to solve for the function $\phi_s(\mathbf{r})$ analytically and impossible to do it numerically without some kind of discretization. For this system of surfactant chains grafted to a spherical surface, the system is treated as spherically symmetric and is divided into *M* concentric spherical shells of thickness δ, starting at the core radius *R* and radiating outward. It is then declared that the solvent volume fraction $\phi_s(\mathbf{r})$, which theoretically varies throughout space, is appropriately represented within the *i*-th spherical shell by the volume-average of $\phi_s(\mathbf{r})$ throughout the *i*-th shell. Thus, instead of the function $\phi_s(\mathbf{r})$, we obtain the vector $\phi_s(i)$:

$$\forall i\in[1,2,...M]\ \ \phi_s(i)=\frac{1}{V(i)}\int_{V(i)}\phi_s(\vec{r})d\vec{r}$$

As a result, every volume integral in the governing equations becomes now a sum over *i* layers:

$$\int_{V_{n,m}}d\vec{r}\ln[\phi_s(\vec{r}:n,m)]n_g(\vec{r},\alpha)\frac{v_P}{v_s}=\frac{v_P}{v_s}\sum_{i=1}^{M}\ln\phi_s(i)\int_{V(i)}d\vec{r}n_g(\vec{r},\alpha)=\frac{v_P}{v_s}\sum_{i=1}^{M}\overline{n}_g(i,\alpha)\ln\phi_s(i)$$

$$\iint_{V_{n,m}}d\vec{r}d\vec{r}'[1-\phi_s(\vec{r})]X(\vec{r},\vec{r}')[1-\phi_s(\vec{r})]=\sum_{i=1}^{M}\sum_{j=1}^{M}\phi_s(i)\phi_s(j)\int_{V(i)V(j)}\int d\vec{r}d\vec{r}'X(\vec{r},\vec{r}')=\sum_{i=1}^{M}\sum_{j=1}^{M}\phi_s(i)\phi_s(j)\overline{X}(i,j)$$

As a direct result, it is no longer necessary to do calculations on any function of **r** in the system because they have all been replaced by a representative average value with in each of the *M* layers. This makes the theory much more amenable to computer solution.

The final step is to note that the solvent volume fractions $\phi_s(i)$ depend on the probability distribution $P_g(\alpha)$ through the incompressibility constraint, but the probability distribution $P_g(\alpha)$ depends on $\phi_s(i)$ through thermodynamics. Therefore, the two quantities must be solved self-consistently, i.e. a set of values $\{\phi_s(i)\}$ must be found such that the $P_g(\alpha)$ calculated from thermodynamics, will return the same set $\{\phi_s(i)\}$ again, calculated by incompressibility. There are many numerical solver packages for this task; we use KINSOL for this set of data.

With that final statement, the name of Single Chain Mean Field theory becomes clear: it is a theory based on the interaction between the conformations $\{\alpha\}$ of a single chain with a series of mean field parameters $\phi_s(i)$.

INHERENT ERROR:
The discretization of the volume around the nanocrystal leads to errors that are relevant to our calculations. The averaging of a function over an entire element presents a particular problem with respect to which conformations are preferred for any given R and σ. The i-th layer is defined as the region between $r = R + (i - 1)\delta$ and $r = R + i\delta$, and within that range a monomer which is $R + (i - {}^{999}/_{1000})\delta$ away from the nanocrystal center is completely indistinguishable from a monomer at $R + (i - {}^{1}/_{1000})\delta$ from the center.

As ω_{TT} increases in magnitude, probability distribution $P_g(\alpha: n,m)$ will adjust to promote smaller values of $\phi_s(i)$. For an arbitrary $\sigma = 10A$, the value of $\phi_s(2)$ is small; when σ increases by A again, $\phi_s(2)$ will decrease, to promote the intermolecular attractions between surfactants, and $\phi_s(3)$ will hardly change at all. However, if σ increases by A again, suddenly the 2nd layer is too full and the entropic losses are too great for $\phi_s(2)$ to decrease again. The result is that $P_g(\alpha)$ shifts to decrease $\phi_s(3)$. For $\omega_{TT} = 0$, the $\phi_s(2)$ would remain untouched as $\phi_s(3)$ increases, but recall that significant values of ω_{TT} will promote smaller values of $\phi_s(3)$, and the shift in the probabilities will cannibalize $\phi_s(2)$ to optimize $\phi_s(3)$. Because monomers at the outermost edge of layer 3 are indistinguishable from monomers at the innermost edge of layer 3, the shift in $P(\alpha: n,m)$ and in $\phi_s(2)$ both become self-consistently non-monotonic. $\phi_s(2)$ increases for $\sigma = 10A$ and $11A$, but decreases at $\sigma = 12A$, all while $\phi_s(3)$ is increasing monotonically. $P_g(\alpha)$ experiences a similar non-uniform redistribution as σ increases, due its dependence on $\{\phi_s\}$, and the result is that q_g oscillates with σ for significant values of ω_{TT}. This is shown graphically in Figure X.1.

This oscillating behavior would not occur given a continuous function $\phi_s(\mathbf{r})$ because a monomer's effect on the SCMF calculation is a continuous function of its location. The averaging technique discretizes a given monomer's effect on the calculation, introducing discontinuities that manifest as oscillations in the otherwise continuous data. Such oscillations are a practical concern when trying to find the zeros of Eq. (6.26), since these oscillations can cause degenerate zeros when a unique solution should exist, and even when a unique zero is found, the oscillations serve to shift the location of that zero. Therefore, the assessment of (R_{eq},σ_{eq}), of $-\ln X_{nm}|_{eq}$, and of $\beta\gamma_{crit}$ are all highly sensitive to the effects of discretization that are implicit in current SCMF framework. That is why the error bars on $\beta\gamma_{crit}$ are so large.

Figure E.1: Oscillations in the grafted chain partition function, $-\ln q_g$, due to discretization of the SCMF equations.